Summer 2014

Multi-objective optimization and meta-modeling of tape-wound transformers

Ahmed Taher
Purdue University

Graduate School ETD Form 9
(Revised 01/14)

PURDUE UNIVERSITY
GRADUATE SCHOOL
Thesis/Dissertation Acceptance

This is to certify that the thesis/dissertation prepared

By Ahmed Taher

Entitled
Multi-objective Optimization and Meta-modeling of Tape-wound Transformers

For the degree of Doctor of Philosophy

Is approved by the final examining committee:

SCOTT D. SUDHOFF, Co-Chair

STEVEN D. PEKAREK, Co-Chair

OLEG WASYNCZUK

DAN JIAO

To the best of my knowledge and as understood by the student in the *Thesis/Dissertation Agreement. Publication Delay, and Certification/Disclaimer (Graduate School Form 32)*, this thesis/dissertation adheres to the provisions of Purdue University's "Policy on Integrity in Research" and the use of copyrighted material.

Approved by Major Professor(s): SCOTT D. SUDHOFF, Co-Chair

Approved by: M. R. Melloch 07/22/2014

Head of the Department Graduate Program Date

MULTI-OBJECTIVE OPTIMIZATION AND META-MODELING OF TAPE-WOUND TRANSFORMERS

A Dissertation

Submitted to the Faculty

of

Purdue University

by

Ahmed Taher

In Partial Fulfillment of the

Requirements for the Degree

of

Doctor of Philosophy

December 2014

Purdue University

West Lafayette, Indiana

إهداء

إلى روح أبي (جدي) الطاهرة,

أهدي بحثي هذا,

وأسأل الله أن يسكنه فسيح جناته,

وأن أكون له إبناً صالحاً يدعو له.

ACKNOWLEDGMENTS

I would like to express my gratitude to GE for funding part of this thesis. Also, I would like to thank my advisors professor Sudhoff and professor Pekarek for their support and encouragement throughout my research as well as my academic program. I would like to extend my gratitude to my advisory committee professor Wasynczuk and professor Jiao.

Finally, I would like to thank my fellow students and the members of the graduate office specially Michelle Wagner and Matt Golden.

TABLE OF CONTENTS

Page

Page

LIST OF TABLES

LIST OF FIGURES

Figure Page

Figure Page

ABSTRACT

Taher, Ahmed A. Ph.D., Purdue University, December 2014. Multi-Objective Optimization and Meta-Modeling of Tape-Wound Transformers. Major Professors: Scott Sudhoff and Steven Pekarek.

In the research presented herein, design models of tape-wound transformers to support component and system-level optimization are considered. As a basis for component optimization, a magnetic equivalent circuit (MEC) model is derived. The key components of the MEC model are the leakage permeances, which have been established using analytical techniques and validated using both 2D and 3D finite element analysis. To enable high frequency design, expressions that predict the winding AC resistance and the proximity effect loss are derived. In addition, a thermal equivalent circuit (TEC) model is established to predict the temperature throughout the transformer and to account for temperature impact on winding resistances. To predict transformer performance, the T-equivalent, MEC, and thermal models are coupled to determine the magnetic operating point and establish core loss, winding loss, voltage regulation, and inrush current given the core and winding geometries, material properties, input voltage, and rated load. The coupled MEC/T-equivalent and the TEC circuit-based performance evaluation is demonstrated within an optimization in which the goals are to minimize mass and minimize loss.

To support system-level optimization, a scaling technique is derived in which transformer size/mass is predicted based upon rated power, specified current density, and frequency. Curve-fitting techniques are used to derive a meta-model for scaled mass and power loss. The meta-model is compared to designs obtained using detailed design code. A strong agreement between the results from the detailed design code and that predicted by the meta-model is achieved.

1. INTRODUCTION

In this research, an objective is to establish tools that enable multi-objective design of tape-wound transformers. Tape-wound transformers are used in numerous applications, including power distribution, galvanic isolation, amplifiers, and dc-dc converters [1]-[12]. An advantage of tape-wound transformers is that there is no airgap in the core. In contrast, in stacked lamination designs, cores are typically assembled by bonding U or I segments together, which creates an effective airgap, which increases the MMF necessary to obtain a desired flux level in the core [1], [2].

A first step in the design process is the derivation of a magnetic equivalent circuit-based model. Within the model, MMF sources are used to represent the primary and secondary windings. To model the flux paths, the transformer core is divided into flux tubes. The permeance of each tube is expressed in terms of the tube dimensions and permeability. A particular focus is on the derivation of the tubes used to model leakage paths, which are critical to accurately capture transformer performance. To enable rapid calculation, symmetry is used to minimize the number of unknowns. The MEC model has been validated using comparisons with 2D and 3D Finite Element models. Therein, a specific focus was to establish techniques to isolate and compare leakage inductances. It has been found that the predicted values obtained from the MEC are in reasonable agreement with finite element (FE) based values.

A second step is to derive expressions which represent the high frequency losses in the transformer windings. High frequency losses are caused by two phenomena. The first is the skin effect which occurs in a conductor carrying an AC current. The time changing flux density produced by the current induces a voltage between the conductor terminals which leads to a current density that is higher on the outside of the conductor than on the inside. By calculating the induced voltage and the current density throughout the

conductor and using the zero-order Bessel function [13], an expression of the conductor AC resistance is derived. This expression is then extended to derive the AC resistance of the transformer windings. The second phenomenon is often preferred to as proximity effect. Proximity effect occurs in a conductor when it is exposed to an external time changing flux density. An expression of the proximity effect in the conductor is derived as a function of the normalized peak flux density [13]. At a frequency of 1 MHz, the winding loss of a transformer can be a hundred times higher than the DC loss [15], which explains the importance of considering the high frequency loss when the transformer performance is evaluated.

As a third step, the transformer thermal equivalent circuit (TEC) is derived. Initially, the thermal equivalent circuit is derived for a cuboidal element. Then, the transformer is divided into 14 cuboidal elements and the TEC is evaluated for each element. Assuming thermal symmetry, only one-eighth of the transformer is analyzed which provide more rapid analysis. Since the transformer coils includes different materials (conductor, insulation, and air) surrounding each other, it is convenient to homogenize the coil to an equivalent anisotropic material [13]. It is noted that some of the cuboids are not rectangular; specifically, the core corner and the end winding curvatures. To resolve this issue, an effective rectangular element is derived such that the total surface area in each direction is held the same [13]. Using the Matlab based TEC toolbox [74], the nodal temperatures at the transformer cuboids are evaluated.

A fourth step is to establish coupling between the MEC and a T-equivalent circuit which includes a core resistance to model core loss, to iteratively establish transformer performance from specified primary voltage and load impedance. To do so, the approach proposed in [13] is applied. Specifically, the MEC model is used to establish leakage inductances and an initial guess of the magnetizing inductance. From these values, the T-equivalent circuit is used to predict magnetizing and secondary voltages and currents, as well as the primary current. These values are then used to update the magnetizing inductance. In addition, the winding currents are input to the MEC model to calculate core flux densities, which are used to update the core resistance. The final iteration is then used to obtain transformer performance, which includes voltage regulation, in-rush

current, core loss, and winding loss. Using the TEC model, the values of the winding resistances are updated.

Within the design process, a multi-objective optimization process based on a tradeoff between the transformer total mass and total loss is performed. In this optimization process, the winding and core geometries and material properties are considered as free or arbitrary parameters. In order to obtain practical designs, constraints include limits on in-rush current, physical dimensions of the transformer, mass, voltage regulation, current density, bending radius, winding height, no-load voltage, and primary current amplitude are imposed. The total mass and total loss correspond to each set of free parameters are evaluated. The process is repeated to obtain a Pareto-optimal front that constitutes the trade-off between the transformer mass and loss. Herein, this process is highlighted for a 5 kVA, 480/240 V, 60 Hz transformer.

The MEC model enables component design. However, in system-level design studies, one cannot represent each component in great detail. Rather, there is a desire to capture the performance (i.e. size and efficiency) based upon specifications of power and voltage. Herein scaling laws are considered on a path to develop a meta-model in which dimensions, parameters, and core loss are estimated based upon desired current density, power, and frequency [41]. The meta-model has been validated through comparison with results obtained using a detailed design process.

Prior to proceeding, it is necessary to consider literature related to these topics. Single- and multi-objective design of transformers has been explored by several researchers [13]-[26]. The typical performance objectives have been to minimize loss, minimize mass, minimize production cost, and minimize operating cost. The uniqueness of the design approach considered herein is primarily the model upon which the optimization has been performed, and in particular the accuracy of the leakage inductance predictions, which are critical to ensure actual performance matches predicted performance. More specifically, in [14]-[26], analytical expressions that relate excitation and core flux density are used as a basis for design. The analytical expressions are derived under the assumption that leakage flux is negligible. In [13], an MEC is used as

a basis for design and leakage permeances are included. However, the derivations are based upon a transformer with a rectangular core.

Related to the transformer modeling, several have considered methods to approximate transformer leakage inductance [27]-[39]. In [27] and [28] a technique was developed in which finite element methods are used to numerically solve for magnetic field within the transformer and surrounding air. Then the field solution is used to calculate the energy which is used to obtain the leakage and magnetizing inductances. Although interesting, a limitation of this method is that it is relatively expensive in terms of computational cost. Second, it requires overhead to establish and grid each new geometry and interface the FE model.

Leakage inductances can be estimated using analytical techniques to solve for the magnetic vector potential in the regions within and surrounding the core. Popular methods of doing so involve using a Fourier-series basis function to represent the vector potential. The resulting vector potential is used to establish field energy, which is then used to compute inductance [29]-[34]. In a related effort, the method of images [35]-[37] has been proposed wherein the boundary conditions are replaced by an infinite set of image conductors. The vector potential is solved for this set of image conductors. Subsequently, the total magnetic energy is expressed as a function of the magnetic vector of each image conductor. For a core type transformer with interleaved windings, this method tends to be prohibitively involved.

Historically, researchers have created generalized expressions for leakage paths around core-type transformers [38], [39]. It is difficult to find the original sources and derivations of these expressions, but they are often attributed to [40]. For example, Lebedev approximates the leakage inductance of a core type transformer as the sum of three parts: the first part is associated with the leakage flux path due to the coil segments inside the core window, the second part is related to the yoke leakage flux path, and the third part is used to represent the leakage flux path caused by the core segments exterior to the core. Since the two coil segments interior to the core window are analogous to the coils of a shell-type transformer then the first term of the leakage inductance can be calculated using the methods developed for estimating the leakage inductance of a shell-

type transformer. The second term is approximated as a function of the number of primary windings and the core conductivity. An expression for the third term was obtained by treating the exterior winding segments as a winding bundle which wound around the core. The problem with this method is that its application is restricted to two winding transformers with each winding created using a single coil. Extending this method to transformers that have multiple coils per winding adds significant complexity.

In this research, an analytical approach is used to obtain the leakage permeances associated with each coil using an approach similar to that proposed in [13]. Subsequently the leakage inductances are calculated using the magnetic equivalent circuit (MEC) [41]-[46]. The advantage of this method is that it is relatively straightforward to implement and is applicable to a wide range of transformer configurations.

In the literature, various methods to model the high frequency effect on the winding loss are discussed [47]-[62]. Dowell's method is used to evaluate a ratio between the AC and DC resistance [47]-[52]. To derive this ratio, the winding is divided into portions where each portion spans a region from zero mmf to a positive or a negative peak mmf. First, the DC resistance is obtained in terms of the transformer geometry. Then, a frequency dependent AC to DC resistance ratio is derived by calculating the induced voltage and the current density under the assumption that the leakage flux lines are parallel to the winding surface. This ratio is multiplied by the DC value to obtain the corresponding AC value. It should be noted that this method is derived for foil windings. To apply this method to round conductors, they need to be replaced by equivalent square conductors. The dimensions of the square conductors are calculated so that the DC resistance is kept the same. Then the square conductors are combined to form a foil winding; then the foil winding is stretched in the height direction until it has similar height to the core interior height. This increase in height is then compensated by a correction factor called the porosity factor. Drawback of this method is that it is only derived for two winding transformer and it is based on one-dimensional field analysis. In addition, replacing a round conductor by a square conductor tends to underestimate the AC resistance as frequency increases. Also, the correction factor makes the skin depth a

function of the transformer dimensions although the skin depth is typically defined a material and frequency related constant.

Another analytical method called Ferreira method which can be applied directly to round conductors is used to predict the transformer skin and proximity effect [53]-[57]. In this method, it is assumed that the magnetic field due to proximity effect is uniform within the conductor. Based on that it has been proved that the proximity effect and the skin effect are orthogonal and thus decoupled. Using Kelvin functions, the AC resistance can be expressed in terms of the DC resistance. This expression is composed of two terms; the first term represents the skin effect and the second term represents the proximity effect.

In a related method, a 2-D numerical simulation results is compared with the Dowell method and the Ferreira method [58]. Based on the simulation results, both methods are reasonably accurate for relatively low frequencies but the error in these methods can go up to 60% for frequencies in the MHz range. In addition, the Dowell method tends to be more accurate when the conductors are close to each other while the Ferreira method tends to be more accurate when the conductor are loosely packed. To compensate the error in the Dowell method, two coefficients were introduced to the Dowell function and their values are obtained using the curve fitting techniques. A good agreement with the simulation result was achieved using this modification.

Many analytical methods explained above are based on one dimensional field analysis of eddy current effects which may not be accurate in predicting the performance of a magnetic device that has multiple windings, an air-gap, or a relatively short winding depth [47]-[57]. On the other hand, using the numerical eddy current analysis to predict the high frequency loss in the device is computationally expensive [58]. Another issue with the numerical methods is the length scale problem where the dimensions of conductors or strands are too small compared to the transformer overall dimensions. To resolve this issue, the proximity effect in the transformer winding is calculated using the square field derivative (SFD) method discussed in [59]-[62]. The SFD method can be used to calculate the proximity effect in round and litz-wire conductors and it can also be derived for rectangular conductors. A first step is to calculate the flux density throughout

each winding using numerical magnetostatic analysis. Then, field analytical analysis is used to derive frequency independent matrix (uniform field) [59],[62] or frequency dependent matrix (non-uniform field) [60], [61] which can be used along with the numerically calculated flux density to evaluate the proximity effect loss. Therefore, computationally expensive numerical eddy current analysis is not required. The SFD method is valid for predicting the proximity effect due to two and three dimensional field with an arbitrary winding excitation. It also proves to be reasonably accurate for predicting the proximity effect loss in inductors and transformers that have air-gap [62].

In [13], the flux density throughout the transformer coil segments is obtained analytically by applying Amare's law to the leakage flux paths. In this research, a method similar to the one discussed in [13] is used to predict the transformer high frequency loss. An advantage of this method is that the proximity effect in some coil segments can be related to the leakage permeance associated with that segment which will be derived in Chapter 3.

To account for the skin effect in the transformer windings, the AC resistance expression derived in [13] is considered. In [13], the AC resistance is first derived for a round conductor. Using Faraday's law, Ampere's law, and the material relationships, a differential equation which relates the current density in the conductor with an arbitrary radius is derived. This differential equation is solved using the zero order Bessel equation and the conductor boundary conditions. Then the solution of the current density is used along with the induced voltage to obtain the conductor AC resistance. This result is then used to obtain the AC resistance of the transformer winding.

Performing the transformer thermal analysis is an important step in the performance evaluation. In previous literature, methods to predict the transformer transient and steady state temperature are discussed [62]-[68].

Finite element (FE) analysis can be used to perform the thermal analysis [63]-[65]. 2-D FE model [63] may not be accurate and 3-D FE model [64] can be computationally expensive. In [65] a combination of 2-D and 3-D models is considered. Since the thermal transient is slower than the electromagnetic transit, it is assumed that the electromagnetic quantities reach steady state before any significant change in the thermal quantities.

Based on this assumption, 3-D thermal analysis is performed in time domain while 2-D electromagnetic analysis is performed in the frequency domain. This method may be sufficient for predicting the temperature of a specific design when the computation time is not an issue. However, when it is required to repeat the thermal analysis thousands or millions of times like in the case of the design optimization problems, it is convenient to use a fast model with much less number of elements.

An alternative approach is a lumped parameter analytical model [66]-[68]. In [66], the 3-D thermal equivalent circuit was derived for a cuboidal element. The thermal model is derived in two steps. First the cuboidal element is analyzed with a zero internal heat source and then it is analyzed with a zero surface temperature. Using the boundary conditions, the heat equation is solved for each case and then the superposition concept is used to combine the results of the two cases.

In [13], the thermal equivalent circuit of an electromagnet is derived. The electromagnet is divided into several cuboidal regions. When a region, such as a coil, includes different materials, it is homogenized to an anisotropic material. Then the method in [66] is applied to each cuboid to obtain the thermal equivalent circuit of the whole device. The same approach is used to obtain the thermal equivalent circuit of a permanent magnet inductor [62], and of electric machines [67], [68].

Herein, similar approach to the one discussed in [13] is used to obtain the thermal equivalent circuit of the tape-wound transformer.

The remainder of this thesis is arranged as follows. In Chapter 2, the transformer dimensions and the T-equivalent circuit are defined as the background of the transformer model derivation. In Chapter 3, the MEC model is derived. The key components of the MEC model are the leakage permeances which are calculated analytically and validated using 2D and 3D finite element analysis. Expressions that account for the skin effect and proximity effect on the winding are established in Chapter 4. To conduct the transformer thermal analysis, a TEC model is derived in Chapter 5. In Chapter 6, the MEC, the T-equivalent circuit, and the TEC models are utilized to perform the operating point analysis and to predict the transformer resistive and core loss, voltage regulation, and inrush current. In Chapter 7, the stage is set for the transformer design process. After

defining the design space, constraints, and fitness function, a multi-objective optimization between mass and loss is performed using genetic algorithms. An example design is presented at the end of this chapter. In Chapter 8, a meta-model based scaling laws is developed for a two winding transformer. The meta-model is validated using a dedicated design code. Then, the scaling laws are extended to establish the meta-model for the tape-wound transformer discussed in previous chapters without including the high frequency loss effects and the thermal model. Finally, the conclusion of this work and the suggestion of future work are presented in Chapter 9.

2. BACKGROUND

Prior to deriving the MEC model, it is useful to define the dimensions of the transformer considered as well as the T-equivalent circuit that is used in concert with the MEC. A cross-sectional view taken from the front of a core-type tape wound transformer is shown in Fig. 2.1. The grey region is the core, the lighter orange region is the α-winding and the darker orange region is the β-winding. The variables α and β are used to denote secondary and primary windings, respectively. As depicted in Fig. 2.1 the core corners are curved and not rectangular since the core considered herein is tape wound. The advantage of curvature is the reduction of saturation at the corners which may improve the transformer performance. The bending of a coil is accomplished at a certain radius which is proportional to the radius of the coil conductors as illustrated by the top cross-sectional view shown in Fig. 2.2. Thus, parallel conductors are generally used to reduce the bending radius.

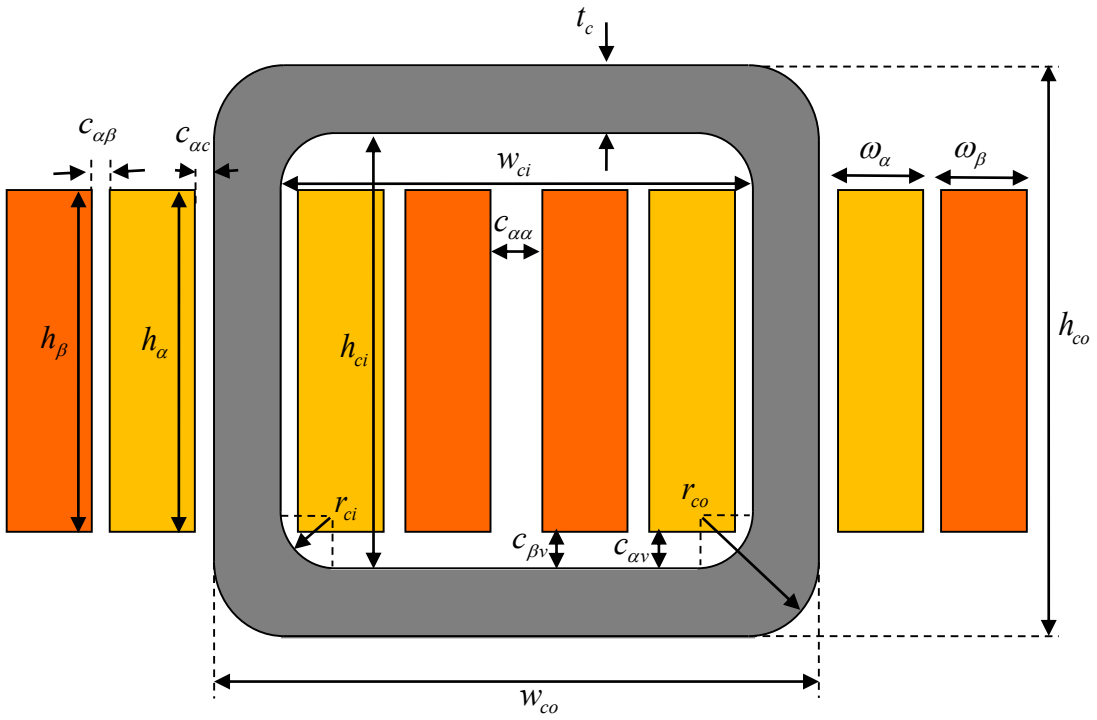

Fig. 2.1 Front Cross-sectional View of Tape-wound Transformer

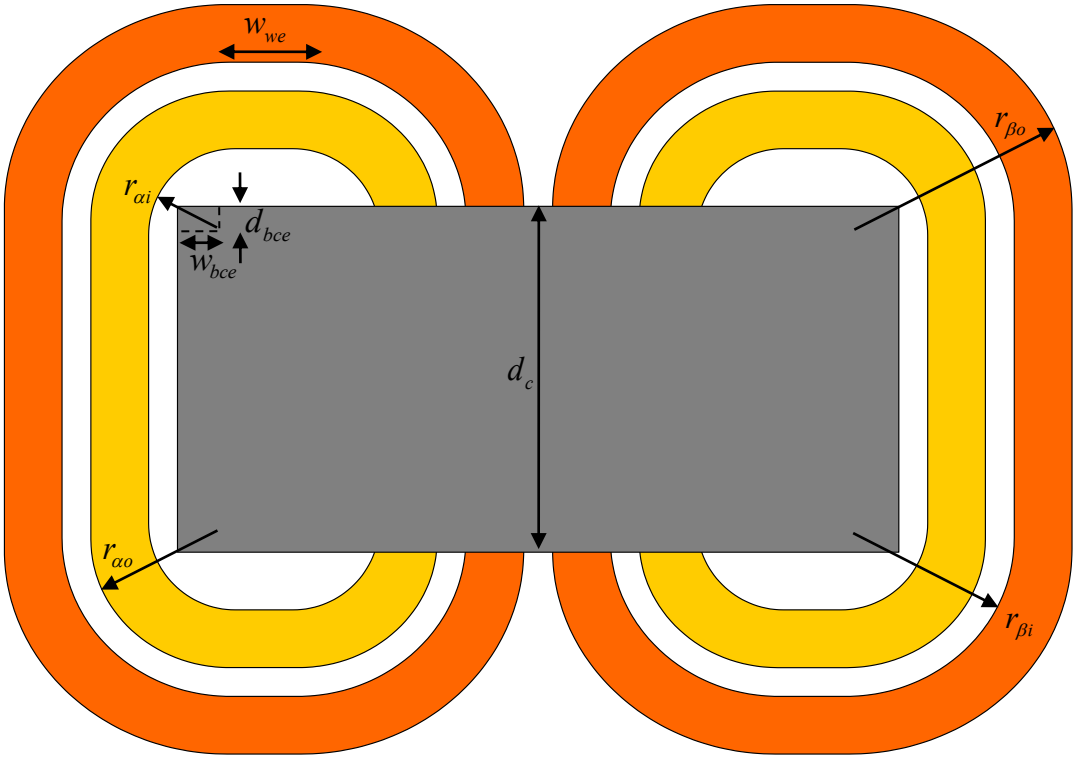

Fig. 2.2 Top Cross-sectional View of Tape-Wound Transformer

As depicted in Fig 2.1 and 2.2, the α and β windings each have 2 coils that can be either series or parallel connected. To be more specific, as part of the design process, the cellular structure shown in Fig. 2.3 is used to construct each coil. The cellular structure consists of first defining the number of parallel conductors, N_{xpr}, used to establish a turn. From the dimensions of the conductor, a unit width w_{xu} is calculated using the diameter of the conductor. The cell height, h_{xu}, is determined from the diameter of the conductor and number of conductors.

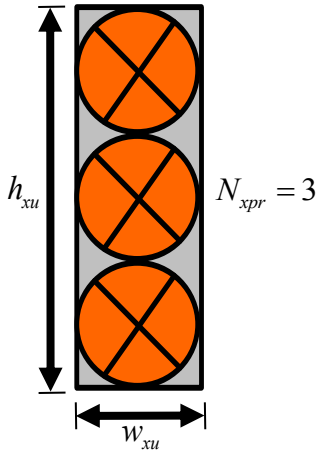

Fig. 2.3 Cell Construction

Subsequently, a coil is formed by defining the number of unit cells N_{xl} (turns) and the aspect ratio (coil height/coil width), which is a design parameter. These are used to establish the number of unit cells placed in the width direction, N_{xuw}, and unit cells placed in the height direction, N_{xuh}. An example is shown in Fig 2.4, wherein a coil with $N_{xl} = 7$ and each turn composed of $N_{xpr} = 3$ conductors, is created with $N_{xuw} = 4$, $N_{xuh} = 2$. This corresponds to an aspect ratio of 1/2.

As shown in Fig. 2.4, some unit cells remain unfilled with conductors; the number of the coil turns is equal to the number of cells that are filled. In this research it is assumed that all coils used to create a winding are identical. Each winding consists of connecting N_{xcs} coils in series and then connecting the resulting series-connected coils N_{xcp} times in parallel. In this research, it is assumed that each winding has $N_{xcs} = 1$ and $N_{xcp} = 2$. Referring back to Fig. 2.1, this means two coils are connected in parallel to form the α and β windings, respectively.

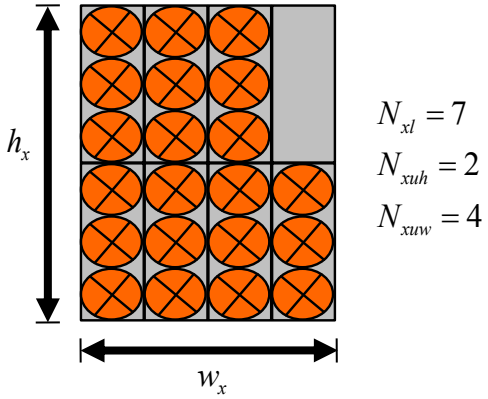

Fig. 2.4 Coil Construction

2.1. T-Equivalent Circuit Model

The equivalent circuit shown in Fig. 2.5 is a relatively common electrical model of the transformer. As shown, r_α and r_β are the α-winding and the β-winding resistances respectively, $L_{l\alpha}$ and $L_{l\beta}$ are the leakage inductances of each winding, L_m is the magnetizing inductance, and R_c is the core resistance which is used to represent the core loss. Using this circuit directly adds complication to analysis due to the presence of the ideal transformer (turns/ratio). Therefore, it is useful to utilize an alternative T-equivalent circuit model [13]. If Φ_m is the flux linking both windings, then by using Faraday's law the induced voltages on both sides of the ideal transformer shown in Fig. 2.5 are

$$e_\beta = N_\beta \frac{d\Phi_m}{dt} \tag{2.1}$$

$$e_\alpha = N_\alpha \frac{d\Phi_m}{dt} \tag{2.2}$$

Dividing (2.1) by (2.2) yields

$$\frac{e_\beta}{e_\alpha} = \frac{N_\beta}{N_\alpha} \tag{2.3}$$

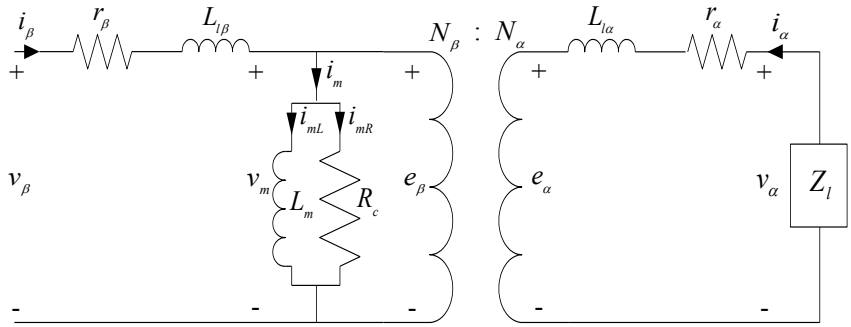

Fig. 2.5 Transformer Equivalent Circuit

Since the power on both sides of the ideal transformer must be the same,

$$e_\alpha i_\alpha = e_\beta \left(i_\beta - i_m \right) \tag{2.4}$$

Substituting (2.3) into (2.4) one obtains

$$\frac{N_\alpha}{N_\beta} i_\alpha + i_\beta = i_m \tag{2.5}$$

Letting

$$i_\alpha^{'} = \frac{N_\alpha}{N_\beta} i_\alpha \tag{2.6}$$

one can express

$$i_\alpha^{'} + i_\beta = i_m \tag{2.7}$$

Applying Kirchhoff's voltage law (K.V.L) to the right hand side of the transformer equivalent circuit, one obtains

$$e_\alpha = v_\alpha - r_\alpha i_\alpha - L_{l\alpha} \frac{di_\alpha}{dt} \tag{2.8}$$

Substituting (2.3) into (2.8), the α-winding voltage equation can be related to the β-winding induced voltage as

$$e_\beta = \frac{N_\beta}{N_\alpha} \left(v_\alpha - r_\alpha i_\alpha - L_{l\alpha} \frac{di_\alpha}{dt} \right) \tag{2.9}$$

From (2.6) and (2.9) the induced winding voltage can be expressed

$$e_{\beta} = \frac{N_{\beta}}{N_{\alpha}} v_{\alpha} - \left(\frac{N_{\beta}}{N_{\alpha}}\right)^2 r_{\alpha} i_{\alpha}^{'} - \left(\frac{N_{\beta}}{N_{\alpha}}\right)^2 L_{l\alpha} \frac{di_{\alpha}^{'}}{dt} \tag{2.10}$$

Defining

$$v_{\alpha}^{'} = \frac{N_{\beta}}{N_{\alpha}} v_{\alpha} \tag{2.11}$$

$$r_{\alpha}^{'} = \left(\frac{N_{\beta}}{N_{\alpha}}\right)^2 r_{\alpha} \tag{2.12}$$

$$L_{l\alpha}^{'} = \left(\frac{N_{\beta}}{N_{\alpha}}\right)^2 L_{l\alpha} \tag{2.13}$$

a final form

$$e_{\beta} = v_{\alpha}^{'} - r_{\alpha}^{'} i_{\alpha}^{'} - L_{l\alpha}^{'} \frac{di_{\alpha}^{'}}{dt} \tag{2.14}$$

is obtained, where $v_{\alpha}^{'}$, $r_{\alpha}^{'}$, $i_{\alpha}^{'}$, and $L_{l\alpha}^{'}$ are considered as the α-winding referred voltage, current, resistance, and leakage inductance, respectively.

One can use similar analysis to define referred load impedance in terms of actual load impedance as

$$Z_{l}^{'} = \left(\frac{N_{\beta}}{N_{\alpha}}\right)^2 Z_{l} \tag{2.15}$$

Using (2.7), (2.14), and (2.15), the ideal transformer windings can be eliminated from the equivalent circuit, yielding the T-equivalent circuit model shown in Fig. 2.6.

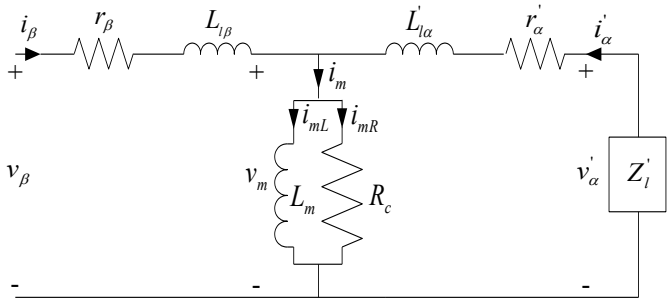

Fig. 2.6 Transformer T-Equivalent Circuit Model

2.2. Phasors

Phasor analysis is used in some of the performance calculations outlined in later chapters. To set the stage for their use, it is convenient to briefly consider a time varying sinusoidal quantity of the form

$$f_j = \sqrt{2} F_j \cos\left(\omega_e t + \phi_{fj}\right) \tag{2.16}$$

where f_j is a voltage, current, or flux linkage, and 'j' an 'α' or 'β', the phasor representation of this quantity is expressed

$$F_j = F_j e^{j\phi_{fj}} \tag{2.17}$$

The variables F_j and ϕ_{fj} are referred to as the magnitude and phase angle of the quantity, respectively.

3. MAGNETIC EQUIVALENT CIRCUIT (MEC)

The development of a magnetic equivalent circuit (MEC) model enables efficient magnetic analysis and design. In this chapter, a model of a tape-wound core transformer is set forth. To set the stage for the MEC model, the transformer core is subdivided into several segments and an expression for the permeance of each segment is derived. Subsequently, an analytical approach set forth in [1] is used to obtain permeances for the leakage paths. Finite element method (FEA) is used to validate the MEC model.

3.1. Core Permeances

The transformer core is subdivided into eight flux tubes as shown in Fig. 3.1. The permeance of each tube is calculated as a function of the tube's length and cross-sectional area and permeability. Permeability in the core is modeled as a function of the tube flux.

3.1.1. Core Leg Permeances

The permeance P_{ch} is associated with the two horizontal core legs which lie between the nodes n_2 and n_3 and between n_6 and n_7 in Fig. 3.1. It may be expressed

$$\mathrm{P}_{ch}\left(\Phi_{ch}\right)=\frac{A_c\mu_{\mathrm{c}}\left(\Phi_{ch}/A_c\right)}{l_{ch}} \tag{3.1}$$

where Φ_{ch} is the magnetic flux in the horizontal leg, μ_{c} is permeability of core material which is a function of the magnetic flux density in the tube, A_c is the core cross-sectional area, and l_{ch} is the flux path length in the horizontal leg. The core cross-sectional area is calculated as

$$A_c=t_c d_c \tag{3.2}$$

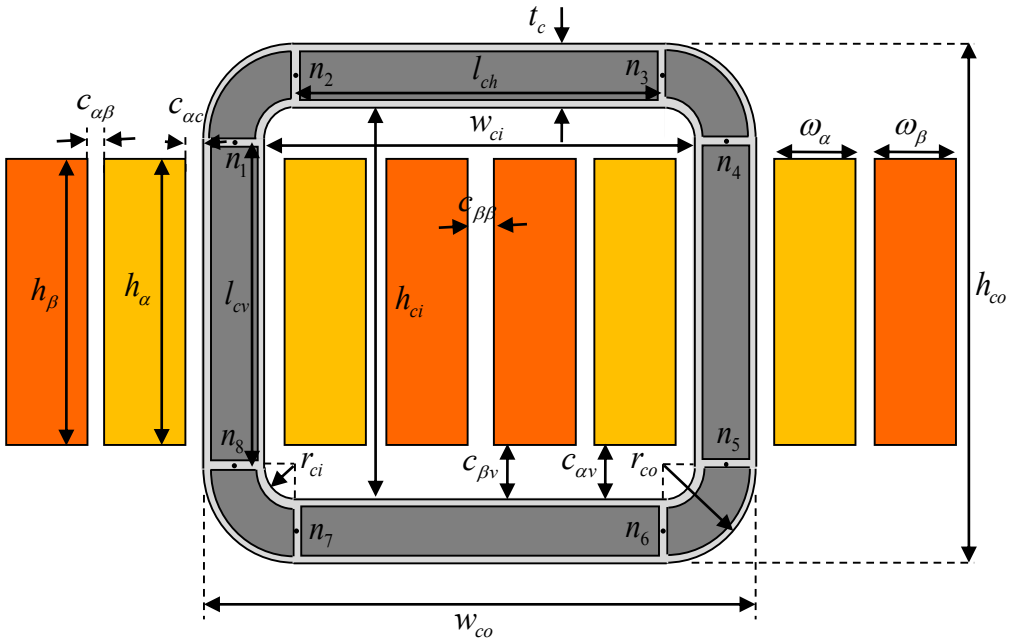

Fig. 3.1 Core Permeance Segments

where t_c is the core thickness and d_c is the core depth. The length of the horizontal leg is obtained using

$$l_{ch} = w_{ci} - 2r_{ci} \tag{3.3}$$

where w_{ci} is the width of the core interior window and r_{ci} is the inner radius of the core corner.

The permeance denoted P_{cv} corresponds to the vertical core legs which lie between n_4 and n_5 and between n_8 and n_1 in Fig.3.1. It is expressed as

$$\mathrm{P}_{cv}\left(\Phi_{cv}\right) = \frac{A_c \mu_c \left(\Phi_{cv} / A_c\right)}{l_{cv}} \tag{3.4}$$

where Φ_{cv} is the magnetic flux in the vertical leg and l_{cv} is the flux path length in the vertical leg which can be expressed

$$l_{cv} = h_{ci} - 2r_{ci} \tag{3.5}$$

where h_{ci} is the height of the core interior window.

3.1.2. Core Corner Permeances

The core corner permeances are those shown between nodes n_1 and n_2, n_3 and n_4, n_5 and n_6, and n_7 and n_8 shown in Fig. 3.1. Since the magnetic field is a function of position on the corners, the flux lines will not be uniformly distributed within the region. To capture the saturation effect, it is useful to divide each corner into a number of parallel segments. As depicted within Fig. 3.2, each corner is divided into *n* parallel segments which have the same cross-sectional area but different tube lengths. As shown in Fig. 3.2, the most inner segment will be the first segment of the core corner to saturate since it has the shortest flux path length and hence the highest permeance while the most outer segment, which has the longest flux path, will be the last segment to saturate.

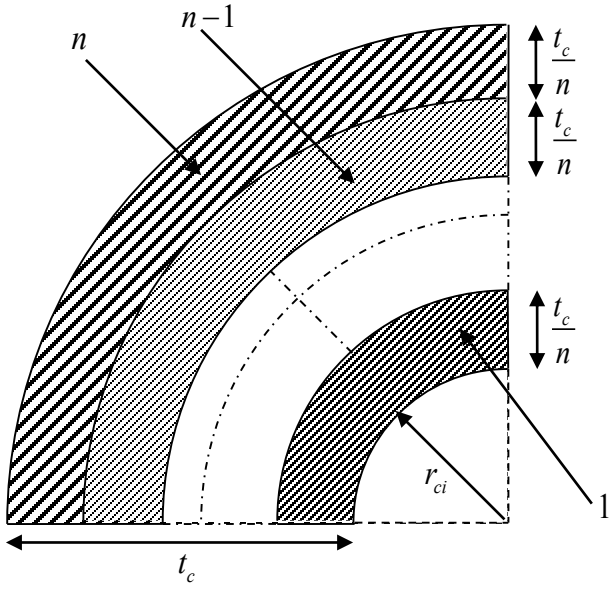

Fig. 3.2 Core Corner Parallel Segments

In order to derive a general expression for corner permeances, the differential permeance is expressed as a function of a differential radius

$$d\,\mathrm{P} = \frac{2\mu_c \left(n\Phi_{cc,i} / A_c \right) d_c dr}{\pi r} \tag{3.6}$$

where $\Phi_{cc,i}$ is the magnetic flux in the ith segment of the core corner. In (3.6), it is assumed that the flux is uniformly distributed throughout the corner. The corner permeance of segment 1, $\mathrm{P}_{co,1}$ is obtained by taking the integral of (3.6) between r_{ci} and $r_{ci}+\frac{t_c}{n}$

$$\mathrm{P}_{co,1}=\frac{2\mu_c\left(n\Phi_{cc,1}/A_c\right)d_c}{\pi}\int_{r_{ci}}^{r_{ci}+\frac{t_c}{n}}\frac{dr}{r} \tag{3.7}$$

Integrating and simplifying (3.7) yields

$$\mathrm{P}_{co,1}=\frac{2\mu_c\left(n\Phi_{cc,1}/A_c\right)d_c}{\pi}\ln\left(1+\frac{t_c}{nr_{ci}}\right) \tag{3.8}$$

Similarly for segment $n-1$

$$\mathrm{P}_{co,n-1}=\frac{2\mu_c\left(n\Phi_{cc,n-1}/A_c\right)d_c}{\pi}\ln\left(1+\frac{t_c}{nr_{ci}+\left(n-2\right)t_c}\right) \tag{3.9}$$

From (3.7) and (3.9) a general expression for the permeance of a segment, can be obtained as

$$\mathrm{P}_{co,k}=\frac{2\mu_c\left(n\Phi_{cc,k}/A_c\right)d_c}{\pi}\ln\left(1+\frac{t_c}{nr_{ci}+\left(k-1\right)t_c}\right),\quad k=1,....,n \tag{3.10}$$

In (3.10), the value of permeance goes down as k goes up which is consistent with Fig. 3.2 where the flux path length increases as one moves outward. Increasing the number of parallel segments n will help capture the saturation more accurately but it will increase the number of MEC meshes. In this research, three segments are used to represent the core corner.

3.2. Leakage Permeances

Leakage permeances are associated with the flux paths that do not have their complete path within the core. The leakage flux path is affected by whether the coil is inside or outside the core window and also by whether the coil is wound directly on the core leg or wound around another coil. To simplify analysis of the leakage paths, it is assumed the core is rectangular and infinitely permeable. Prior to establishing specific

leakage permeances for the α and β windings, it is convenient to derive expressions for the general leakage flux paths depicted in Fig. 3.3. In particular, from Fig. 3.3, one can see that general expressions are needed for the case in which a coil section is within the core window, when a coil section is outside the core window and adjacent to the core, and a coil section is outside the core winding and separated from the core.

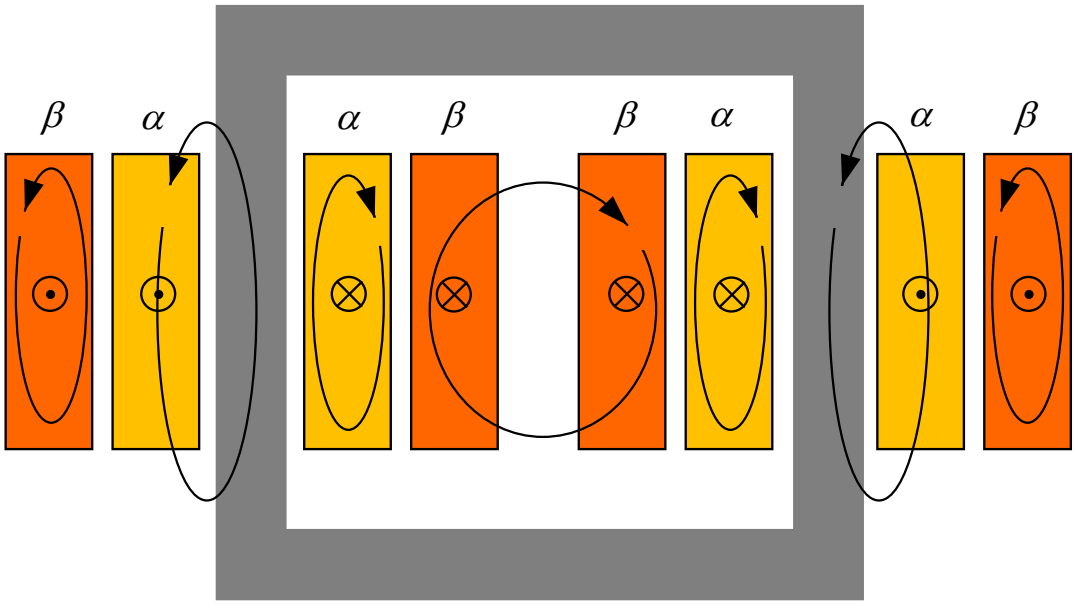

Fig. 3.3 Transformer Leakage Paths

Prior to deriving these generalized expressions, it is useful to define several path lengths and highlight some additional geometric details. Within the model, the distance between the center-point of the bending radius and the core edges are defined by the variables d_{bce} and w_{bce}. These are shown in Fig. 3.4. As shown, extending a horizontal line from the center-point of the bend radius to the coil provides the location where bending begins relative to the horizontal core edge. Similarly, extending a line vertically from the center-point of the bend radius to the coil provides the location where bending ends relative to the vertical core edge.

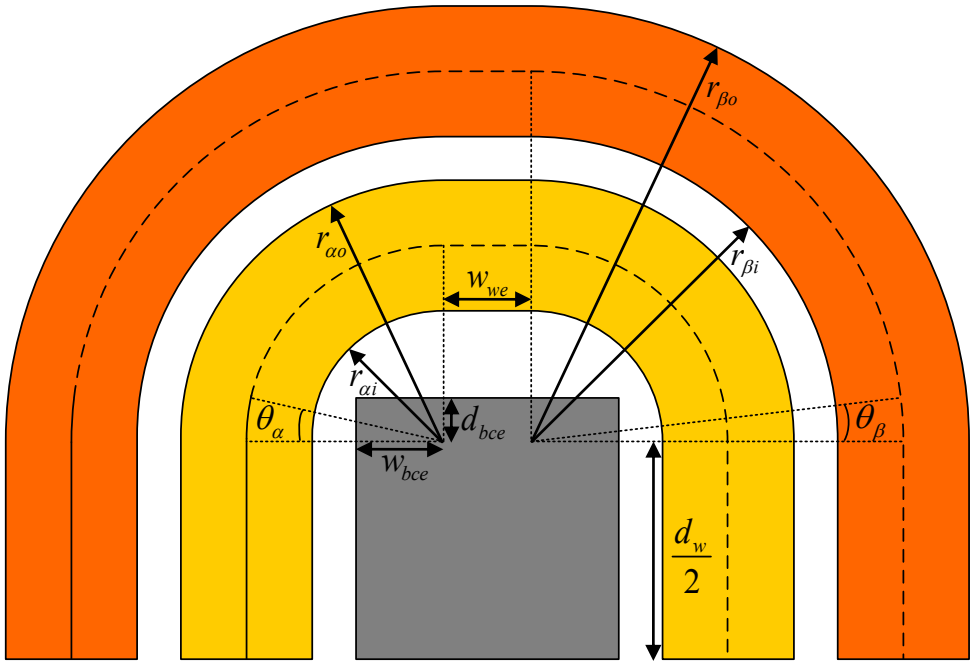

Fig. 3.4 Coils Interior and Exterior Sections

Since each coil is divided into a part that is interior to the core window and another part that is exterior, it is convenient to define which part is considered to be interior and which is considered to be exterior. To do so, the dimensions of the top view cross-section shown in Fig. 3.4 are helpful. Therein, the section of the coil that is interior to the window is shown as a solid line and the section that is exterior is shown as a dashed line. The point that separates the interior and the exterior sections of the coil is assumed to occur when the coil centerline intersects from the core edge as shown in Fig. 3.4. The angle that is formed between this line that connects this point and the center of the bending arc and the horizontal line extending from the arc center is

$$\theta_j = \text{asin}\left(\frac{2d_{bce}}{r_{ji} + r_{jo}}\right) \tag{3.11}$$

where the coil interior and exterior radii are calculated as

$$r_{ji} = \begin{cases} w_{bce} + c_{\alpha c} & \text{j} = '\alpha' \\ r_{\alpha o} + c_{\alpha\beta} & \text{j} = '\beta' \end{cases} \tag{3.12}$$

$$r_{jo} = r_{ji} + w_j \tag{3.13}$$

where w_{bce} and d_{bce} is the distance between the bending curve center and the core edge in the width and depth directions respectively. The length of the straight section of a coil is expressed

$$d_w = d_c - 2d_{bce} \tag{3.14}$$

The interior and the exterior length of the coil can be found as

$$l_{ji} = d_w + \theta_j \left(r_{ji} + r_{jo} \right) \tag{3.15}$$

$$l_{je} = d_w + 2w_{we} + \left(\pi - \theta_j \right) \left(r_{ji} + r_{jo} \right) \tag{3.16}$$

where w_{we} the width of the end winding, r_{ji} is the interior bending radius of winding j, r_{jo} is the exterior bending radius of winding j. After defining the leakage paths and their lengths, expressions for the leakage permeances of the primary and secondary coils can be obtained.

3.2.1. Interior coil leakage permeance

The first leakage paths considered are those attributed to a coil that is interior to the core window. The two paths that form the basis of the derivation are shown in Fig. 3.5. As shown, there is a path within the coil window and one that is external to the coil window but is internal to the core. To calculate the permeance associated with leakage flux within the coil window, an energy-based analysis is applied.

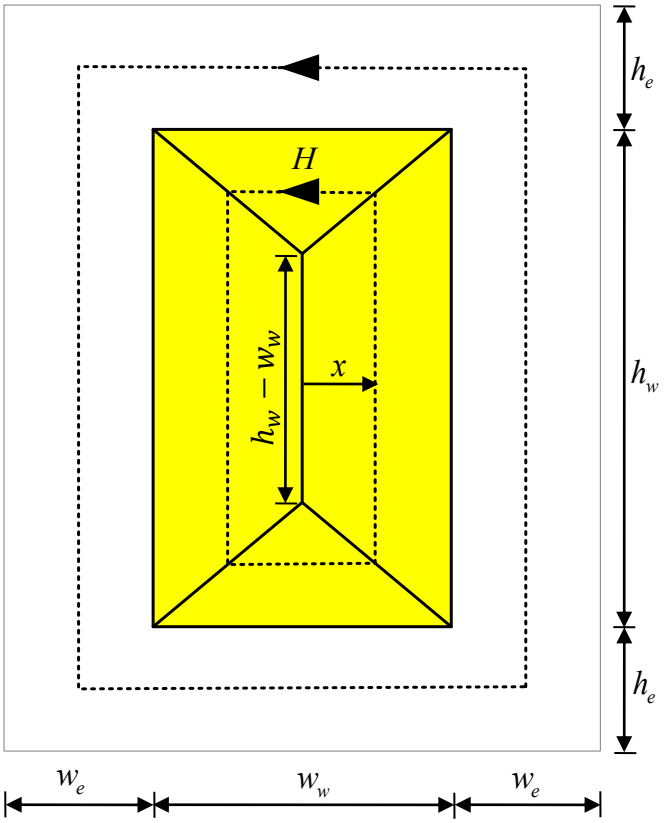

Fig. 3.5 Interior Coil Leakage Flux Paths

Specifically, it is useful to express the energy stored inside the coil window in terms of the magnetic field: [13]

$$E = \frac{1}{2}\mu \int_V H^2 dV \tag{3.17}$$

where H is the magnetic field, μ is the permeability, and V is the volume of the coil window. The energy within the coil window volume can also be expressed in terms of coil current, number of coil turns, and the leakage permeance as [13]

$$E = \frac{1}{2} P N^2 i^2 \tag{3.18}$$

Applying Ampere's law to the interior path shown in Fig. 3.5, assuming the magnetic field is uniform on the path, yields

$$Hl_p = \frac{a_p}{w_w h_w} Ni \tag{3.19}$$

where l_p is the path length and a_p the area enclosed by the path, respectively. These are calculated as

$$l_p = 2\left|h_w - w_w\right| + 8x \qquad 0 < x < x_{\max} \tag{3.20}$$

$$a_p = 2x\left|h_w - w_w\right| + 4x^2 \qquad 0 < x < x_{\max} \tag{3.21}$$

where $x_{\max} = \min\left(\frac{h_w}{2}, \frac{w_w}{2}\right)$

The differential volume of integration in (3.17) is expressed as

$$dV = l_p l_i dx \tag{3.22}$$

where in general l_i represents the coil length interior to the core window. It is noted that when performing comparisons of the MEC with 2D FEA, this length is taken to be the depth of the core. Using and (3.19)-(3.22) in (3.17) one can express

$$E = \frac{1}{2}\mu_0 \frac{N^2 i^2 l_i}{w_w^2 h_w^2} \int_0^{x_{\max}} \frac{\left(2x\left|h_w - w_w\right| + 4x^2\right)^2}{2\left|h_w - w_w\right| + 8x} \tag{3.23}$$

Solving (3.23) and equating the result with (3.18) the leakage permeance associated with the internal leakage flux is expressed as [13]

$$P_{ili} = \frac{\mu_0 l_i}{128 w_w^2 h_w^2}\left(4k_2^2 + 8k_1 k_2^3 + 2k_1^2 k_2^2 - 2k_1^3 k_2 + k_1^4 \ln\left(1 + \frac{2k_2}{k_1}\right)\right) \tag{3.24}$$

where

$$k_1 = \left|h_w - w_w\right| \tag{3.25}$$

$$k_2 = \min\left(h_w, w_w\right) \tag{3.26}$$

The leakage path exterior to the coil window but interior to the core is calculated by dividing the leakage path into two horizontal and two vertical flux tubes that are all series tied. The resulting permeance is obtained:

$$P_{eli} = \frac{\mu_0 l_i}{2\left(\frac{w_w + w_e}{h_e} + \frac{h_w + h_e}{w_e}\right)} \tag{3.27}$$

Finally, the total interior conductor leakage permeance of a coil is obtained as

$$P_{li} = P_{ili} + P_{eli} \tag{3.28}$$

3.2.2. Exterior leakage permeance of coil section external to the core window and adjacent to the core

A diagram that depicts the leakage paths of a coil section external to the core window and adjacent to the core is shown in Fig. 3.6. To calculate the leakage permeance associated with the internal leakage flux path, the path length and area are expressed as

$$l_p = |h_w - 2w_w| + 4x \tag{3.29}$$

$$a_p = x|h_w - 2w_w| + 2x^2 \tag{3.30}$$

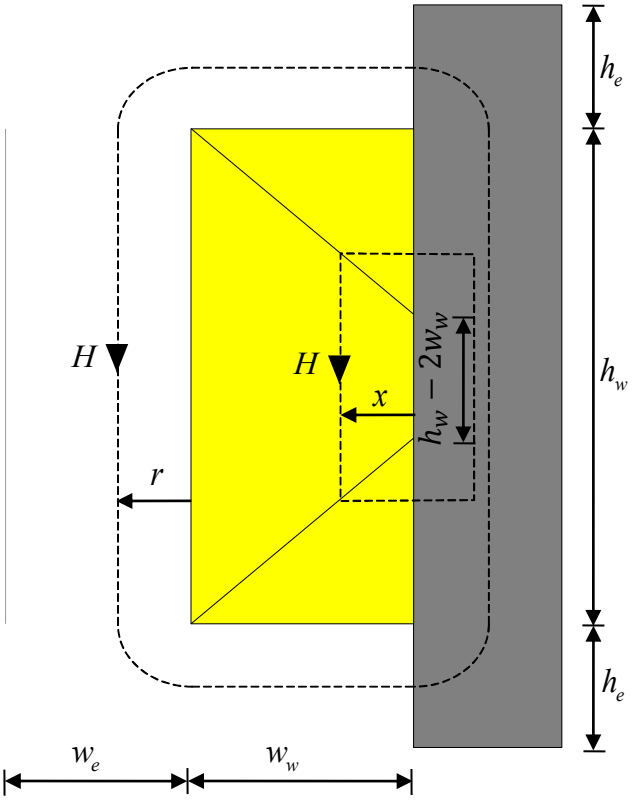

Fig. 3.6 Exterior Adjacent Coil Leakage Flux Paths

Repeating the same argument made in describing (3.17)-(3.23) with the new path length and area in (3.29) and (3.30), that results due to neglecting H in the iron, and using $x_{\max} = \min\left(\frac{h_w}{2}, w_w\right)$, one can obtain the permeance associated with the coil exterior and adjacent to the core as [13]

$$P_{ilea} = \frac{\mu_0 l_{ea}}{256 w_w^2 h_w^2}\left(16k_2^2 + 16\sqrt{2}k_1k_2^3 + 4k_1^2k_2^2 - 2\sqrt{2}k_1^3k_2 + k_1^4 \ln\left(1 + \frac{2\sqrt{2}k_2}{k_1}\right)\right) \tag{3.31}$$

where

$$k_1 = \left|h_w - 2w_w\right| \tag{3.32}$$

$$k_2 = \frac{1}{\sqrt{2}}\min\left(h_w, 2w_w\right) \tag{3.33}$$

The leakage permeance of the path exterior to the coil window that is exterior and adjacent to the core is expressed as

$$P_{elea} = \int_0^{x_{\max}} \frac{\mu_0 l_{ea} dr}{l_p} \tag{3.34}$$

where $x_{\max} = \min\left(h_e, w_e\right)$ and the path length is calculated as

$$l_p = h_w + 2w_w + \pi r \tag{3.35}$$

Substituting (3.35) into (3.34) and solving yields

$$P_{elea} = \frac{\mu_0 l_{ea}}{\pi}\ln\left(1 + \frac{\pi x_{\max}}{h_w + 2w_w}\right) \tag{3.36}$$

The total exterior adjacent conductor leakage permeance associated with coil external to the core window and adjacent to the core is obtained as

$$P_{lea} = P_{ilea} + P_{elea} \tag{3.37}$$

3.2.3. Exterior coil isolated from core leakage permeance

By comparing Fig. 3.7 with Fig. 3.5, one can notice that the leakage flux path within the coil window is the same. Thus,

$$P_{ilei} = P_{ili} \tag{3.38}$$

The leakage permeance representing flux external to the coil is expressed as

$$P_{elei} = \int_0^{x_{\max}} \frac{\mu_0 l_{ei} dr}{l_p} \tag{3.39}$$

where $x_{\max} = w_e$ and the path length is calculated as

$$l_p = 2h_w + 2w_w + 2\pi r \tag{3.40}$$

Substituting (3.40) into (3.39) and solving yields

$$P_{elei} = \frac{\mu_0 l_{ei}}{2\pi} \ln\left(1 + \frac{\pi w_e}{h_w + w_w}\right) \tag{3.41}$$

The total exterior isolated conductor leakage permeance is calculated as

$$P_{lei} = P_{elei} + P_{elei} \tag{3.42}$$

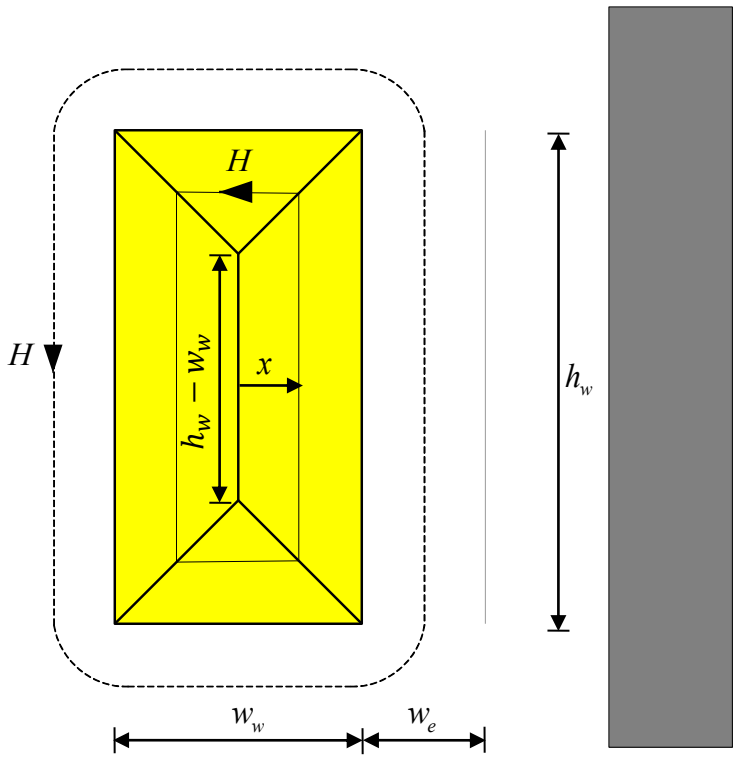

Fig. 3.7 Exterior Isolated Coil Leakage Flux Paths

3.2.4. Leakage permeances of α-winding

The permeances of the leakage flux paths shown in Fig. 3.8 are now considered using the results of the previous subsections. The leakage permeance of the α-winding $P_{\alpha l}$ is divided into two parts, one which represents the leakage flux path that is interior with respect to the core window, $P_{\alpha li}$, and one which represents the leakage flux path that is exterior with respect to the core window, $P_{\alpha le}$. The permeance $P_{\alpha li}$ is obtained using

$$P_{\alpha li} = P_{i\alpha li} + P_{e\alpha li} \tag{3.43}$$

In (3.43), (3.24) and (3.27) are used to establish

$$P_{i\alpha li} = \frac{\mu_0 l_{\alpha i}\left(4k_{\alpha i2}^4 + 8k_{\alpha i1}k_{\alpha i2}^3 + 2k_{\alpha i1}^2k_{\alpha i2}^2 - 2k_{\alpha i1}^3k_{\alpha i2} + k_{\alpha i1}^4 \ln\left(1+\frac{2k_{\alpha i2}}{k_{\alpha i1}}\right)\right)}{128 w_\alpha^2 h_\alpha^2} \tag{3.44}$$

$$P_{e\alpha li} = \frac{\mu_0 l_{\alpha i}}{\left(\left(h_{ci}+h_\alpha\right)\left(\frac{1}{2c_{\alpha c}}+\frac{1}{c_{\alpha\beta}}\right)+\frac{\left(2w_\alpha + c_{\alpha c} + c_{\alpha\beta}\right)}{c_{\alpha v}}\right)} \tag{3.45}$$

where

$$k_{\alpha i1} = \left|h_\alpha - w_\alpha\right| \tag{3.46}$$

$$k_{\alpha i2} = \min\left(h_\alpha, w_\alpha\right) \tag{4.47}$$

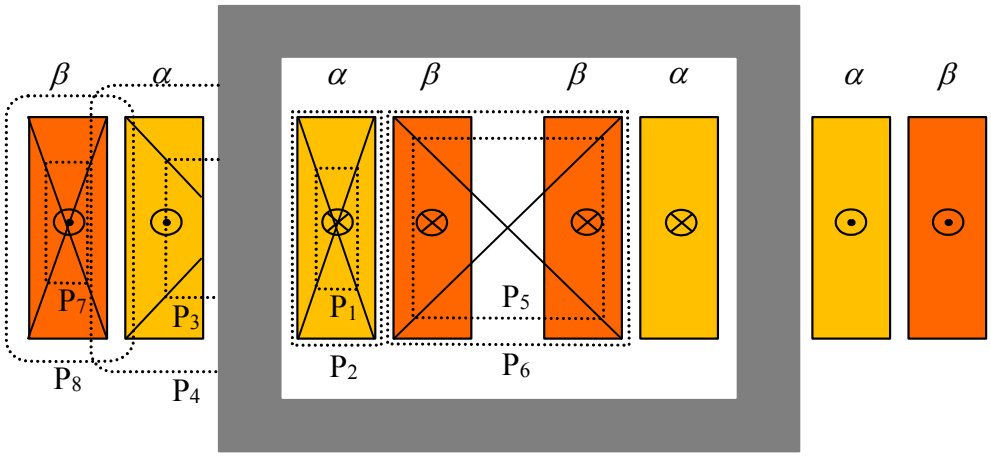

Fig. 3.8 Leakage Flux Paths

The permeance $P_{\alpha le}$, (which is associated with paths P_3 and P_4 shown in Fig. 3.8), is obtained using

$$P_{\alpha le} = P_{i\alpha le} + P_{e\alpha le} \tag{3.48}$$

In (3.48), the quantities $P_{i\alpha le}$ and $P_{e\alpha le}$ are obtained from (3.31) and (3.36); in particular

$$P_{i\alpha le} = \frac{\mu_0 l_{\alpha e}\left(16k_{\alpha e2}^4 + 16\sqrt{2}k_{\alpha e1}k_{\alpha e2}^3 + 4k_{\alpha e1}^2k_{\alpha e2}^2 - 2\sqrt{2}k_{\alpha e1}^3k_{\alpha e2} + k_{\alpha e1}^4 \ln\left(1+\frac{2\sqrt{2}k_{\alpha e2}}{k_{\alpha e1}}\right)\right)}{256w_\alpha^2 h_\alpha^2} \tag{3.49}$$

$$P_{e\alpha le} = \frac{\mu_0 l_{\alpha e}}{\pi}\ln\left(1+\frac{\pi\min\left(\left(c_{\alpha\beta}+0.5w_\beta\right),0.5\left(h_{co}-h_\alpha\right)\right)}{2w_\alpha + 2c_{\alpha c} + h_\alpha}\right) \tag{3.50}$$

where

$$k_{\alpha e1} = \left|h_\alpha - 2w_\alpha\right| \tag{3.51}$$

$$k_{\alpha e2} = \frac{1}{\sqrt{2}}\min\left(h_\alpha, 2w_\alpha\right) \tag{3.52}$$

and h_{co} is the height of the core outer window.

It might occur to the reader that (3.43) should be added to (3.48) since they represent the leakage permeances of the interior and exterior segments of the same coil. However, the leakage flux paths of the exterior coil are coupled through the vertical core leg as illustrated in Fig. 3.8 and thus adding the two could lead to inaccuracy in the MEC model.

3.2.5. Leakage permeances of β-winding

the leakage permeances of the β-winding are now considered. The interior flux is evaluated based on the paths P_5 and P_6 shown in Fig. 3.8. Using the results in Section 3.2.1, after the appropriate substitution of subscripts one can obtain

$$P_{\beta li} = P_{i\beta li} + P_{e\beta li} \tag{3.53}$$

In (3.53), (3.24) and (3.27) are used [13]

$$P_{i\beta li}=\frac{\mu_0 l_{\beta i}\left(4k_{\beta i2}^4+8k_{\beta i1}k_{\beta i2}^3+2k_{\beta i1}^2k_{\beta i2}^2-2k_{\beta i1}^3k_{\beta i2}+k_{\beta i1}^4\ln\left(1+\frac{2k_{\beta i2}}{k_{\beta i1}}\right)\right)}{64w_\beta^2h_\beta^2} \tag{3.54}$$

$$P_{e\beta li}=\frac{\mu_0 l_{\beta i}}{\left(\frac{h_{ci}+h_\beta}{c_{\alpha\beta}}+\frac{\left(2w_\beta+c_{\alpha\beta}+c_{\beta\beta}\right)}{c_{\beta v}}\right)} \tag{3.55}$$

where

$$k_{\beta i1}=\left|h_\beta-2w_\beta+c_{\beta\beta}\right| \tag{3.56}$$

$$k_{\beta i2}=\min\left(h_\beta,2w_\beta+c_{\beta\beta}\right) \tag{3.57}$$

As shown in Fig. 3.8, the two interior coil segments of the β-winding are treated as a single winding bundle with a width of $2w_\beta+c_{\beta\beta}$. Although this might seem a crude approximation, it is justified by the fact that the two coils are carrying the same current and practically, the clearance between them is likely small compared to their widths.

It should be noted that even though the two coils are treated as a single coil for the permeance calculation, two identical permeances are used to represent them within the MEC model. The reason is that one permeance is associated with the leakage flux caused by the current in the right hand side coil and the other is associated with the leakage flux produced by the current in the left hand side coil. Therefore, the result in (3.54) and (3.55) includes a factor of two.

The exterior leakage permeance of the β-winding denoted $P_{\beta le}$ is obtained by considering paths P_7 and P_8 in Fig. 3.8 and using the result in Section 3.2.3 for an exterior coil isolated from the core. Doing this yields

$$P_{\beta le}=P_{i\beta le}+P_{e\beta le} \tag{3.58}$$

In (3.58), the results of (3.38) and (3.41) are applied, which yields [13]

$$P_{i\beta le}=\frac{\mu_0 l_{\beta e}\left(4k_{\beta e2}^4+8k_{\beta e1}k_{\beta e2}^3+2k_{\beta e1}^2k_{\beta e2}^2-2k_{\beta e1}^3k_{\beta e2}+k_{\beta e1}^4\ln\left(1+\frac{2k_{\beta e2}}{k_{\beta e1}}\right)\right)}{128w_\beta^2h_\beta^2} \tag{3.59}$$

$$P_{e\beta le} = \frac{\mu_0 l_{\beta e}}{2\pi} \ln\left(1 + \frac{\pi\left(0.5w_\alpha + c_{\alpha\beta}\right)}{h_\beta + w_\beta}\right) \tag{3.60}$$

where

$$k_{\beta e1} = \left|w_\beta - h_\beta\right| \tag{3.61}$$

$$k_{\beta e2} = \min\left(w_\beta, h_\beta\right) \tag{3.62}$$

In this research the leakage flux due to the α-winding that is coupled to β-winding is neglected. This will lead to a slight overestimate of the leakage inductance. However, since the limit on the leakage inductance in the transformer design is typically an upper limit, the analysis presented will tend to a conservative value. Considering this approximation, the permeances due to the interior and exterior portion of the β-winding can be combined into a single permeance which is referred $P_{\beta l}$ and which may be expressed as

$$P_{\beta l} = P_{\beta li} + P_{\beta le} \tag{3.63}$$

3.3. Transformer Magnetic Equivalent Circuit

The transformer MEC based on the work in the previous sections is depicted in Fig. 2.11. The only components that have not been mentioned in the previous sections are the MMFs associated with the α-winding coils $N_{\alpha cl} i_{\alpha c}$ and the β-winding coils $N_{\beta cl} i_{\beta c}$, where $N_{\alpha cl}$ and $N_{\beta cl}$ are the number of turns and $i_{\alpha c}$ and $i_{\beta c}$ the currents of the α-winding coils and β-winding coils respectively. The coil current i_{jc} and the winding current i_j of winding j are related using

$$i_{jc} = \frac{i_j}{N_{jcp}} \tag{3.64}$$

where N_{jcp} is the number of parallel coils used to create the j-winding and ‘ j ’ may be ‘ α ’ or ‘ β ’.

In Fig. 3.9, the arrows are used to show that the relationship between flux and MMF is nonlinear.

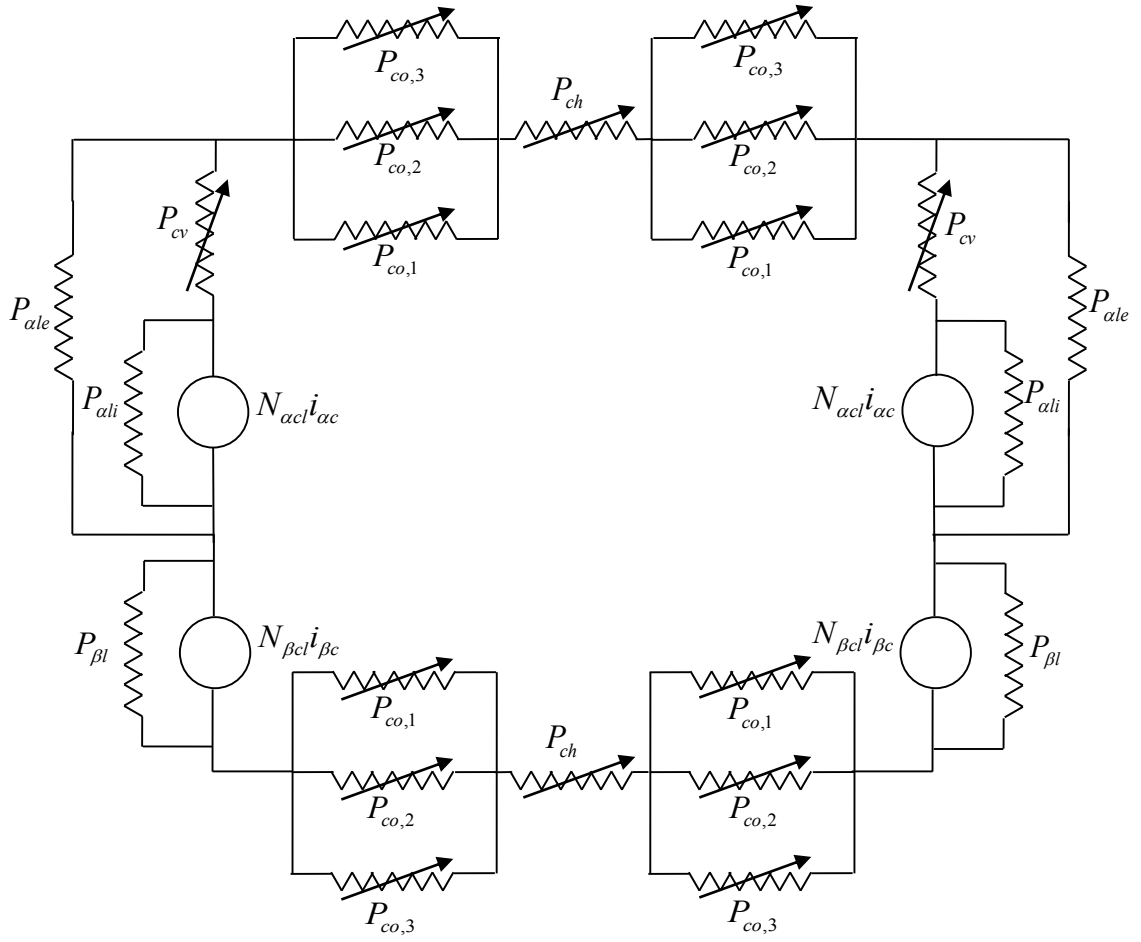

Fig. 3.9 Transformer Magnetic Equivalent Circuit

Taking advantage of the symmetry in Fig. 3.9, one can obtain the reduced magnetic circuit shown in Fig. 3.10. Mesh analysis is used to solve the reduced MEC where Φ_{m1}, Φ_{m2}, Φ_{m3}, and Φ_{m4} denote the mesh fluxes. The flux through each core permeance is also defined since it is needed to obtain the value of the corresponding permeance and for core loss calculation. This will be discussed in more detail in Chapter 4 when the nominal design approach is considered.

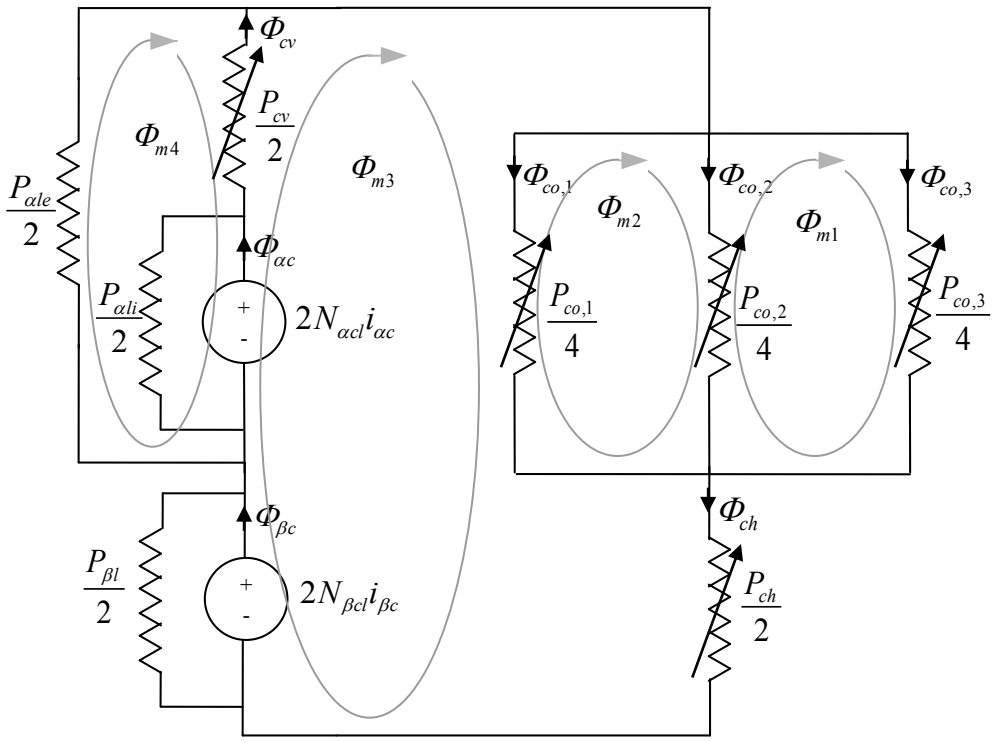

Fig. 3.10 Reduced Magnetic Equivalent Circuit

3.4. Leakage Inductances

Leakage inductances are critical parameters in the T-equivalent circuit as discussed in Chapter 2. A leakage inductance may be defined as the inductance that is associated with the flux paths that do not have their complete path within the core. As previously mentioned, when the leakage paths are considered, the core is assumed to be infinitely permeable and thus the leakage inductances are constant. This assumption is reasonable provided the core is not highly saturated; which is unlikely in high performance designs.

Since each winding consists of more than one coil, it is useful to relate the number of winding j turns, N_j, to the number of turns of the corresponding coils, N_{jcl}, as

$$N_j = N_{jcl} N_{jcs} \tag{3.65}$$

where N_{jcs} is the number of j-winding coils in series. Using the MEC in Fig 3.10 and the turns in (3.65), the α-winding and β-winding flux linkages can be expressed as

$$\lambda_\alpha = N_\alpha \left(\Phi_{m3} - \Phi_{m4} + N_{\alpha cl} i_{\alpha c} P_{\alpha li} \right) \tag{3.66}$$

$$\lambda_\beta = N_\beta \left(\Phi_{m3} + N_{\beta cl} i_{\beta c} P_{\beta l} \right) \tag{3.67}$$

To calculate leakage inductances, the magnetizing inductance is first considered. Due to saturation, the value of the magnetizing inductance depends on the magnetizing current. However, at low magnetizing currents, the anhysteretic *B-H* magnetizing curve is linear, and hence the magnetizing inductance is assumed constant. Using the T-equivalent circuit derived in Chapter 2, the magnetizing inductance in the linear region can be calculated as

$$L_{m0} = \frac{\lambda_\alpha \big|_{i_\beta = i_{\beta,t}, i_\alpha = 0} N_\beta}{N_\alpha i_{\beta,t}} \tag{3.68}$$

where $i_{\beta,t}$ is a test current applied to β-winding, which is taken to be small relative to the nominal magnetizing current.

The leakage inductance of the α-winding is referred to the β-winding using the appropriate turns ratio. From the T-equivalent circuit, leakage inductances can be expressed as

$$L'_{l\alpha} = \left(\frac{N_\beta}{N_\alpha} \right)^2 \frac{\lambda_\alpha \big|_{i_\beta = 0, i_\alpha = i_{\alpha,t}}}{i_{\alpha,t}} - L_{m0} \tag{3.69}$$

$$L_{l\beta} = \frac{\lambda_\beta \big|_{i_\beta = i_{\beta,t}, i_\alpha = 0}}{i_{\beta,t}} - L_{m0} \tag{3.70}$$

where the "prime" in (3.69) is used to denote referred variables.

Typically, in the transformer T-equivalent circuit, the impedance of the magnetizing branch is relatively high compared to the impedance of the leakage branch. Therefore, as an approximate the magnetizing branch can be shifted to the left side, which makes the α-winding and the β-winding leakage inductance appears as a series connection. Thus, the aggregate leakage inductance is obtained

$$L_l = L_{l\beta} + L'_{l\alpha} \tag{3.71}$$

3.5. Leakage Inductance Validation

Since the models of leakage permeance are different than ones developed previously in the literature [33]-[45], it is useful to validate the derivations presented. To do so, 2-D and 3-D finite element models for a transformer whose dimensions are shown in Table 3.1 were created. The dimensions in Table 3.1 are related to those of a design from the optimization process that is detalied in Chapter 4. The core material used in the design is M-19. Its anhysteretic *BH* and core loss properties are provided in [50].

Table. 3.1 Transformer Dimensions for Leakage Inductance Validation.

Parameter	**Value**	**Parameter**	Value
r_{ci} (mm)	1.276	$c_{\alpha c}$ (mm)	2.5
d_c (m)	0.2594	$c_{\alpha\beta}$ (mm)	2.5
h_{ci} (m)	0.1002	$c_{\beta\beta}$ (mm)	2.5
w_α (m)	0.01813	$N_{\alpha cl}$	164
h_α (m)	0.09519	$N_{\alpha cs}$	1
w_β (m)	0.02324	$N_{\alpha cp}$	2
h_β (m)	0.09152	$N_{\beta cl}$	334
x_{rw} (m)	0.023205	$N_{\beta cs}$	1
y_{rw} (m)	0	$N_{\beta cp}$	2
w_{we} (m)	0.0574		

Figures of the 2-D and 3-D geometries used in the FEA are shown in Fig. 3.11. To reduce the simulation time, it is useful to take advantage of the transformer symmetry. As shown in Fig. 3.11, one fourth of the transformer in the case of the 2-D and one eighth of the transformer in the case of the 3-D are sufficient to predict the transformer performance and reduce the simulation time significantly. The maximum allowed percentage error in the total energy was set to 0.001% in the 2-D case and 0.4% in the 3-D case. To calculate the inductances using FEA, the energy in the system resulting from winding excitation is calculated. Analytically, the field energy can be expressed as [52]

$$E = \frac{1}{2}\left(L'_{l\alpha} + L_{lm} + L_m\right)i'^2_\alpha + \left(L_{lm} + L_m\right)i'_\alpha i_\beta + \frac{1}{2}\left(L_{l\beta} + L_{lm} + L_m\right)i^2_\beta \tag{3.72}$$

In (3.72), the inductances $L_{l\alpha}^{'}$, $L_{l\beta}$, and L_m are associated with previous analysis of the winding leakage and magnetizing inductances. The additional term L_{lm} is used to represent mutual leakage coupling that occurs between the windings, but has been neglected in the MEC model.

To obtain values of $L_{l\alpha}^{'}$ and $L_{l\beta}$ predicted from the FEA, the winding currents are set to $i_{\alpha}^{'} = -I_t$ and $i_{\beta} = I_t + \Delta i$. Substituting these values into (3.72), one can express the resulting energy as

$$E = \frac{1}{2} L_{l\alpha}^{'} \left(I_t + \Delta i \right)^2 + \frac{1}{2} L_{l\beta} I_t^2 + \frac{1}{2} L_{lm} \Delta i^2 \tag{3.73}$$

where Δi is a current increment. Using three current increments of Δi_1, Δi_2, and Δi_3, the corresponding energies E_1, E_2, and E_3 are used to determine the leakage and mutual inductances from

$$\begin{bmatrix} L_{l\alpha}^{'} \\ L_{l\beta} \\ L_{lm} \end{bmatrix} = \frac{1}{2} \begin{bmatrix} \left(I_t + \Delta i_1 \right)^2 & I_t^2 & \Delta i_1^2 \\ \left(I_t + \Delta i_2 \right)^2 & I_t^2 & \Delta i_2^2 \\ \left(I_t + \Delta i_3 \right)^2 & I_t^2 & \Delta i_3^2 \end{bmatrix}^{-1} \begin{bmatrix} E_1 \\ E_2 \\ E_3 \end{bmatrix} \tag{3.74}$$

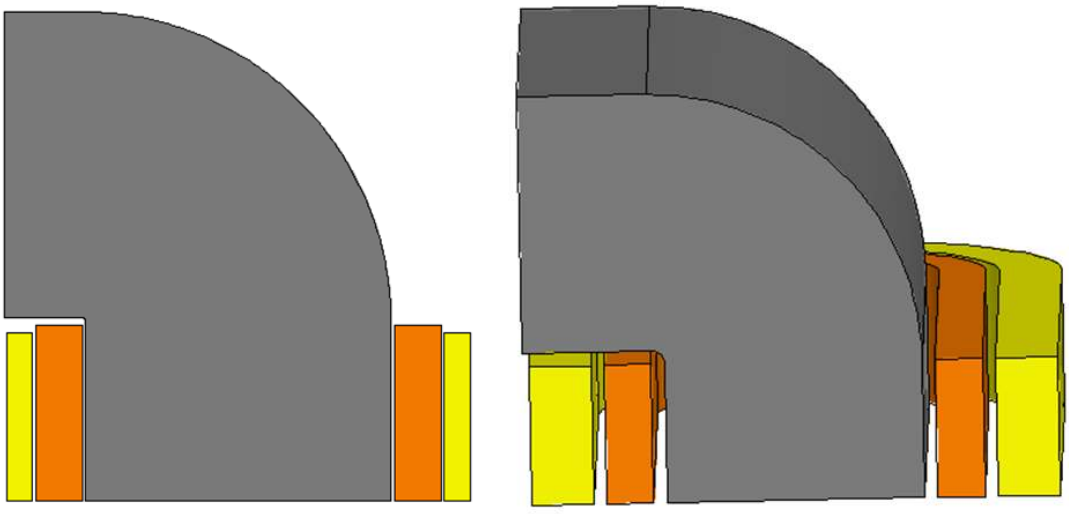

(a) (b)

Fig. 3.11 Transformer FEA models: (a) 2-D Model and (b) 3-D Model

The comparison between the FEA and the MEC for the 2-D and the 3-D models are shown in Table 3.2 and Table 3.3, respectively. For both models, the leakage inductances are calculated using (3.69)-(3.71). In the 2-D MEC model, the interior and exterior leakage path lengths are both taken to be equal to the depth of the core. For the 3-D MEC, the interior and exterior leakage path lengths are calculated using (3.15) and (3.16), respectively. From the results in Tables 2.2 and 2.3 it is observed that the discrepancy between FEA and MEC results are within a reasonable range and in particular that the error in the total leakage inductance is within 10% for both 2-D and 3-D cases. It is noted that the value of the leakage inductance obtained by the MEC is underestimated in the 2-D case and it is overestimated in the 3-D case.

Table. 3.2 Comparison of Leakage Inductances from 2-D MEC and FEA Models.

Parameter	**MEC**	**FEA**	Error (%)
$L_{l\beta}$ (H)	0.7745	0.8013	-3.34
$L'_{l\alpha}$ (H)	0.3840	0.4625	-16.97
L_l (H)	1.1585	1.2638	-8.33

Table. 3.3 Comparison of Leakage Inductances from 3-D MEC and FEA Models.

Parameter	**MEC**	**FEA**	Error (%)
$L_{l\beta}$ (H)	1.1667	1.1239	3.808
$L'_{l\alpha}$ (H)	0.5125	0.4559	12.415
L_l (H)	1.6791	1.5798	6.286

4. HIGH FREQUENCY LOSSES

Developing a model of the transformer resistance requires consideration of high frequency losses. High frequency losses are caused by two phenomena. The first is the skin effect which leads to a current density on the outside of a conductor. The uneven distribution of current density leads to an increase in the conductor effective resistance which leads to additional loss. The second phenomenon is often referred to as proximity effect. When a conductor is exposed to an external time changing field, eddy currents within the conductor are induced which translate to loss. At low frequency, skin and proximity effect losses are negligible compared to the loss associated with the DC resistance. As frequency increases, it is required to account for skin and proximity effect losses to accurately predict the performance of an electromagnetic device. In this chapter, the high frequency loss model is derived for a cylindrical conductor. The model is then extended to predict the high frequency loss associated with transformer windings.

4.1. Skin Effect

When a conductor is carrying an AC current, a time-changing field is produced. This field causes the current density within the conductor to become larger on the exterior than on the interior of the conductor. This phenomenon is referred to as the skin effect. Due to the skin effect, the conductor resistance denoted as the AC resistance tends to be higher than the DC resistance.

In this section, an expression for the AC resistance of a cylindrical conductor is derived. To do so, Fig. 4.1 is considered. According to Faraday's law

$$\int \mathrm{E}\cdot dl = -\int_S \frac{d\,\mathrm{B}}{dt}\cdot ds \tag{4.1}$$

Applying (4.1) around the voltage loop shown in Fig 4.1 yields

$$\int_0^1 \mathrm{E}(r)\,dl + \int_1^2 \mathrm{E}(r)\,dl + \int_2^3 \mathrm{E}(r)\,dl + \int_3^0 \mathrm{E}(r)\,dl = l\int_0^r \frac{d\,\mathrm{B}_\phi}{dt}dr \tag{4.2}$$

Assuming that $l \gg$, where l is the conductor length and R is the conductor radius, one obtains

$$\mathrm{E}_z(r) - \mathrm{E}_z(0) = \int_0^r \frac{\mathrm{d}\,\mathrm{B}_\phi}{dt}dr \tag{4.3}$$

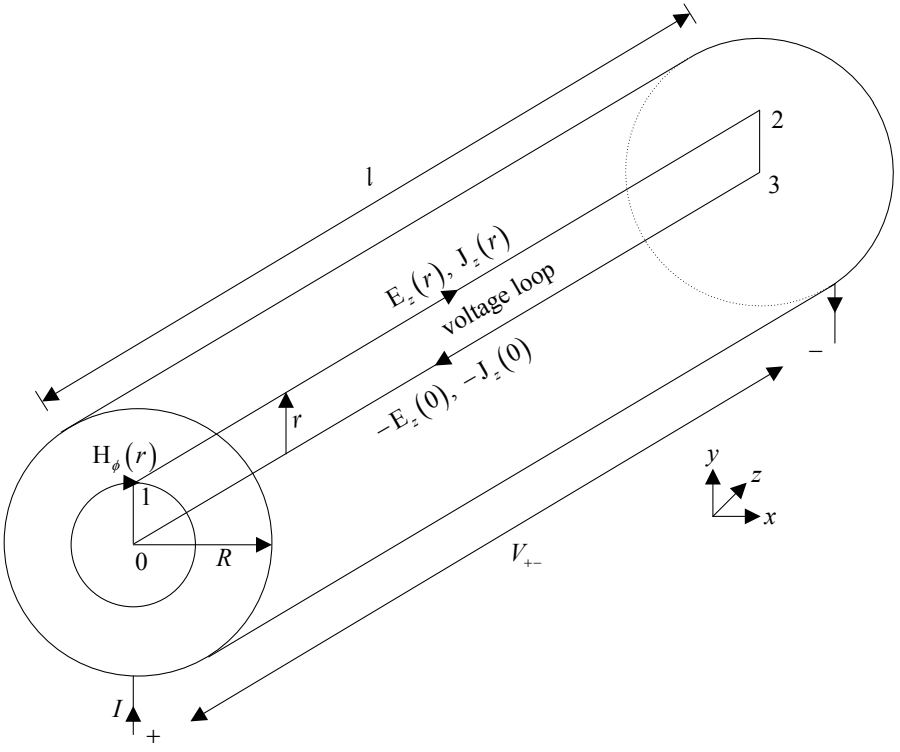

Fig. 4.1 Calculation of Skin Effect for a Cylindrical Conductor

For a sinusoidal waveform, a phasor transformation can be applied to (4.3) which yields

$$\mathrm{E}_z(r) - \mathrm{E}_z(0) = j\omega\int_0^r \mathrm{B}_\phi\,dr \tag{4.4}$$

Taking the derivative of both sides of (4.4) with respect to r yields

$$\frac{d\,\mathrm{E}_z}{dr} = j\omega\,\mathrm{B}_\phi \tag{4.5}$$

Applying the material relationships

$$\mathrm{J}_z = \sigma \mathrm{E}_z \tag{4.6}$$

$$\mathrm{B}_\phi = \mu \mathrm{H}_\phi \tag{4.7}$$

to (4.5) and simplifying yields

$$j\omega\sigma\mu \mathrm{H}_\phi = \frac{d\,\mathrm{J}_z}{dr} \tag{4.8}$$

By applying Ampere's law around the circular path at radius r shown in Fig. 4.1

$$2\pi r \mathrm{H}_\phi(r) = \int_0^r \mathrm{J}_z(r) 2\pi r dr \tag{4.9}$$

Taking the derivative with respect to r yields

$$r\frac{\partial \mathrm{H}_\phi(r)}{\partial r} + \mathrm{H}_\phi(r) = \mathrm{J}_z(r) r \tag{4.10}$$

For sinusoidal waveforms, a phasor relationship can be expressed

$$r\frac{d\,\mathrm{H}_\phi(r)}{dr} + \mathrm{H}_\phi(r) = \mathrm{J}_z(r) r \tag{4.11}$$

By substituting $\tilde{\mathrm{I}}$ obtained from (4.8) into (4.11), one obtains

$$r\frac{d^2\,\mathrm{J}_z(r)}{dr^2} + \frac{d\,\mathrm{J}_z(r)}{dr} - rj\omega\sigma\mu\,\mathrm{J}_z(r) = 0 \tag{4.12}$$

Letting

$$\hat{r} = \frac{r}{k} \tag{4.13}$$

where

$$k = \sqrt{\frac{j}{\omega\sigma\mu}} \tag{4.14}$$

and substituting (4.13) into (4.12) yields

$$\hat{r}^2\frac{d^2\,\mathrm{J}_z(\hat{r})}{dr^2} + \hat{r}\frac{d\,\mathrm{J}_z(\hat{r})}{dr} + \hat{r}^2\,\mathrm{J}_z(\hat{r}) = 0 \tag{4.15}$$

It is noted that (4.15) is the same form as the zero order Bessel equation, which has the solution

$$\mathrm{J}_z\left(\hat{r}\right)=c_1\,\mathrm{J}_B\left(\hat{r}\right)+c_2\,\mathrm{Y}_B\left(\hat{r}\right) \tag{4.16}$$

where c_1 and c_2 are constants determined by boundary conditions, and where $\mathrm{J}_B\left(\hat{r}\right)$ and $\mathrm{Y}_B\left(\hat{r}\right)$ are the Bessel function of the first kind of order zero and the Bessel function of the second kind of order zero, respectively. These are expressed as

$$\mathrm{J}_B\left(\hat{r}\right)=1+\sum_{m=1}^{\infty}\frac{\left(-1\right)^m\hat{r}^{2m}}{2^{2m}\left(m!\right)^2}\quad \hat{r}\geq 0 \tag{4.17}$$

and

$$\mathrm{Y}_B\left(\hat{r}\right)=\left[\left(\gamma+\ln\left(\frac{2}{\hat{r}}\right)\right)\mathrm{J}_B\left(\hat{r}\right)+\sum_{m=1}^{\infty}\frac{\left(-1\right)^{m+1}y_m}{2^{2m}\left(m!\right)^2}\hat{r}^{2m}\right]\quad \hat{r}\geq 0 \tag{4.18}$$

where

$$y_m=\sum_{k=0}^{m-1}\frac{1}{m-k} \tag{4.19}$$

and

$$\gamma=\lim_{m\to\infty}\left(y_m-\ln m\right)\cong 0.5772 \tag{4.20}$$

In order to solve (4.16), two boundary conditions are applied. The first is that J_y must be finite at any radius r. However, it is noted from (4.18) that when $r=0$ at which $\hat{r}=0$, $\mathrm{Y}_B\left(0\right)$ is infinite. Therefore, c_2 must be zero in order to satisfy this boundary condition. This reduces (4.18) to

$$\mathrm{J}_z\left(\hat{r}\right)=c_1\,\mathrm{J}_B\left(\hat{r}\right) \tag{4.21}$$

Substituting the value of $\hat{r}$ using (4.13) and then taking the derivative of (4.21) with respect to the radius and then setting $r=R$ yields

$$\frac{d\,\mathrm{J}_z\left(R\right)}{dr}=\frac{c_1}{k}\mathrm{J}_B^{'}\left(R/k\right) \tag{4.22}$$

In (4.22)

$$\mathrm{J}^{'}\left(R/k\right)=\frac{d}{dx}\mathrm{J}\left(R/k\right) \tag{4.23}$$

According to Ampere's law

$$H_{\phi}(R) = \frac{I}{2\pi R} \tag{4.24}$$

From (4.8) and (4.24)

$$\frac{dJ_z(R)}{dr} = \frac{j\omega\mu\sigma I}{2\pi R} \tag{4.25}$$

Equating the right side of (4.22) and (4.25) yields

$$J_1 = -\frac{I}{2\pi R k \, \mathrm{J}_B'(R/k)} \tag{4.26}$$

By substituting (4.26) into (4.21), the conductor current density at radius r is obtained

$$J_z = -\frac{I \, \mathrm{J}_B(r/k)}{2\pi R k \, \mathrm{J}_B'(R/k)} \tag{4.27}$$

In order to calculate the conductor internal impedance, Fig. 4.1 is considered. The voltage between the positive and negative node is expressed as

$$V_{+-} = E_z(R) l \tag{4.28}$$

From (4.6), (4.27), and (4.28), the conductor AC impedance is obtained

$$Z = \frac{V_{+-}}{I} = -\frac{l \, \mathrm{J}_B(r/k)}{2\pi R k \sigma \, \mathrm{J}_B'(R/k)} \tag{4.29}$$

4.2. Proximity Effect

To derive an expression for the proximity effect, Fig. 4.2 is considered. As depicted in Fig. 4.2, the current is flowing into the page through an infinitely small band with width dy and a distance y below the center line of the conductor and it is flowing out of the page through a band with width dy and a distance y above the center line of the conductor. To neglect the conductor end effect, it is assumed that the conductor length into page is much greater than the conductor radius which is typically the case for many electromagnetic devices.

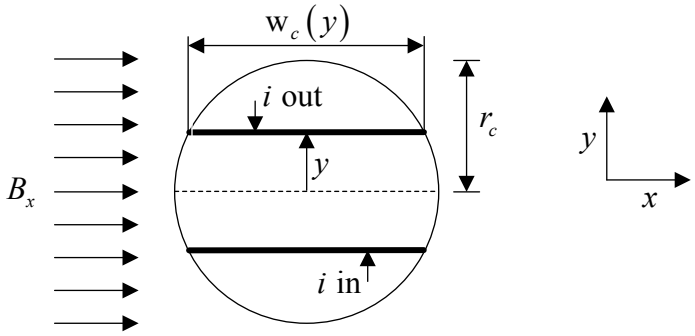

Fig. 4.2 Calculation of Proximity Effect for a Cylindrical Conductor

As depicted in Fig. 4.2, the current flowing in the conductor is due to an external field and there is no voltage applied across the conductor terminals. Therefore, applying Kirchhoff's voltage law around a loop beginning at the lower band, traveling into the conductor and returning through the upper band neglecting the voltage drop on the ends of the conductor yields

$$ri + \frac{d\lambda}{dt} = 0 \tag{4.30}$$

where r is the resistance of the conductor which is expressed as

$$r = \frac{2l}{\sigma w_c(y)dy} \tag{4.31}$$

In (4.31), $w_c(y)$ is defined as

$$w_c(y) = 2\sqrt{r_c^2 - y^2} \tag{4.32}$$

Assuming a uniform field, the flux linking the conductor may be expressed as

$$\lambda = 2ylB_x \tag{4.33}$$

Substituting (4.31)-(4.33) into (4.30) and simplifying gives

$$i = -2y\sigma\sqrt{r_c^2 - y^2}\,\frac{dB_x}{dt}dy \tag{4.34}$$

The differential power loss in the differential loop caused by the proximity effect field can be calculated as

$$dS = i^2 r \tag{4.35}$$

By substituting (4.31), (4.32), and (4.34) into (4.35) one obtains

$$dS = 4\sigma l\left(\frac{dB_x}{dt}\right)^2 y^2\sqrt{r_c^2 - y^2}\,dy \tag{4.36}$$

The total instantaneous power lost in the conductor is obtained by taking the integral of (4.36) as follows

$$S = \int_0^{r_c} 4\sigma l\left(\frac{dB_x}{dt}\right)^2 y^2\sqrt{r_c^2 - y^2}\,dy \tag{4.37}$$

Solving (4.37) and simplifying yields

$$S = \frac{\pi}{4}\sigma r_c^4 l\left(\frac{dB_x}{dt}\right)^2 \tag{4.38}$$

The total average power is obtained by taking the time average of (4.38) using

$$\overline{S} = \frac{\pi}{4}\sigma r_c^4 l\frac{1}{T}\int_0^T\left(\frac{dB_x}{dt}\right)^2 dt \tag{4.39}$$

Due to the conductor symmetry, the results in (4.39) can also be applied if the external filed is in the y- direction, thus,

$$\overline{S} = \frac{\pi}{4}\sigma r_c^4 l\frac{1}{T}\int_0^T\left(\frac{dB_y}{dt}\right)^2 dt \tag{4.40}$$

For more general expression, it is assumed that

$$B_x = B_p\cos\phi \tag{4.41}$$

$$B_y = B_p\sin\phi \tag{4.42}$$

where B_p is the peak flux density at an arbitrary angle ϕ which denotes the direction of the external field with respect to the x- axis. Substituting (4.41) into (4.39) and (4.42) into (4.40), the total average power due to the external field can be expressed as

$$\overline{S} = \frac{\pi}{4}\sigma r_c^4 l\overline{\left(\frac{dB_p}{dt}\right)^2} \tag{4.43}$$

where

$$\overline{\left(\frac{dB_p}{dt}\right)^2} = \frac{1}{T}\int_0^T \left(\frac{dB_p}{dt}\right)^2 dt \tag{4.44}$$

Assuming that a winding w with N_w conductors is uniformly distributed throughout a region r. The proximity effect associated with this winding may be expressed as

$$\overline{S}_{pwr} = N_w \frac{\pi}{4}\sigma r_c^4 l_c \left\langle \overline{\left(\frac{dB_p}{dt}\right)^2} \right\rangle_r \tag{4.45}$$

In (4.45) $\langle\ \rangle_\Omega$ is the spatial average over a region Ω and it is defined as

$$\langle x \rangle_\Omega = \frac{1}{\Omega}\int_S x d\Omega \tag{4.46}$$

where Ω could be length, area, or volume.

4.2.1. Proximity Effect Loss in adjacent windings

In a multi-winding device, the leakage flux associated with adjacent windings may be coupled which lead to proximity effect loss due to this coupling. To demonstrate the proximity effect caused by this coupling, two adjacent windings a and b are considered. Assuming that the j-component of the leakage flux density associated with each winding is B_{aj} and B_{bj} respectively, the proximity effect loss in the region inside the w-winding is expressed as

$$\overline{S}_{pwr} = \gamma_{wr} \sum_{j=x,y} \left\langle \overline{\left(\frac{dB_{aj}}{dt}\right)^2} + 2\overline{\left(\frac{dB_{aj}}{dt}\frac{dB_{bj}}{dt}\right)} + \overline{\left(\frac{dB_{bj}}{dt}\right)^2} \right\rangle_{wr} \tag{4.47}$$

where w is a or b and x and y denote the x- and y-component of the leakage flux density, and

$$\gamma_{wr} = N_w \frac{\pi}{4}\sigma r_c^4 l_c \tag{4.48}$$

It is convenient to represent the loss in terms of the winding current. To achieve this, the normalized flux density is defined as

$$\hat{B}_{wj} \quad \frac{B_{wj}\big|_{\text{due to } i_w}}{i_w} \tag{4.49}$$

where i_w is the w- winding current. Substituting (4.49) into (4.47) yields

$$\overline{S}_{jwr} = \gamma_{wr} \sum_{j=x,y} \left\langle \hat{B}_{aj}^2 \overline{\left(\frac{di_a}{dt}\right)^2} + 2\hat{B}_{aj}\hat{B}_{bj} \overline{\left(\frac{di_a}{dt}\frac{di_b}{dt}\right)} + \hat{B}_{bj}^2 \overline{\left(\frac{di_b}{dt}\right)^2} \right\rangle_{wr} \tag{4.50}$$

The result in (4.50) can be expressed in matrix form as

$$\overline{S}_{jwr} = \overline{\frac{di^T}{dt} r_{D_{wr}} \frac{di}{dt}} \tag{4.51}$$

where

$$i = [i_a \quad i_b]^T \tag{4.52}$$

and $r_{D_{wr}}$ is the dynamic resistance in the region inside the w- winding which is defined as

$$r_{D_{wr}} = \gamma_{wr} \left\langle \begin{matrix} \hat{B}_{ax}^2 + \hat{B}_{ay}^2 & \hat{B}_{ax}\hat{B}_{bx} + \hat{B}_{ay}\hat{B}_{by} \\ \hat{B}_{ax}\hat{B}_{bx} + \hat{B}_{ay}\hat{B}_{by} & \hat{B}_{bx}^2 + \hat{B}_{by}^2 \end{matrix} \right\rangle_{wr} \tag{4.53}$$

4.2.2. Expressing the Dynamic Resistance in terms of Leakage Permeance

In order to calculate the dynamic resistance, it is required to obtain the value of the mean squared flux density which depends on the corresponding flux path. When the flux path associated with the proximity effect is similar to the flux path associated with the leakage permeance, the mean squared field can be related to the leakage permeance expression derived previously in Chapter 3. To obtain this relationship, an energy approach is used. The energy stored in a volume U_{wr} is expressed as

$$E = \frac{1}{2} \int_{U_{wr}} BHdU \tag{4.54}$$

where B and H are scalar components of fields directed along the assumed leakage path of the flux density and the field intensity within the volume.

The energy in a volume that encloses a transformer coil may be expressed in terms of the leakage permeance P as

$$E = \frac{1}{2} N^2 i^2 P \tag{4.55}$$

Equating (4.54) and (4.55) yields

$$P = \frac{\int_{U_r} B_p H_p dU}{N^2 i^2} \tag{4.56}$$

By applying the normalization of (4.49) to (4.56), one obtains

$$P = \frac{\int_{U_r} \hat{B}_p^2 dU}{\mu_0 N^2} \tag{4.57}$$

Applying the spatial average definition in (4.46) into (4.57) and simplifying yields

$$\left\langle \hat{B}_p^2 \right\rangle_r = \frac{\mu_0 N^2 P}{U_r} \tag{4.58}$$

The dynamic resistance may be expressed in terms of the leakage permeance by substituting (4.48) and (4.58) into (4.53)

$$r_{D_r} = \frac{\mu_0 \pi N^3 \sigma r_c^4 l_c P}{4 U_r} \tag{4.59}$$

4.3. Transformer High Frequency Loss

The expressions for the skin effect and the proximity effect losses which are derived in the previous sections can be applied to the tape-wound transformer considered in this research. First the skin effect is considered. From (4.29), the AC resistance of the j-coil may be expressed as

$$r_{jcl} = -\frac{N_{jcl}}{N_{jpr}} \mathrm{Re}\left(\frac{U_{jcl} J_B\left(r_{jc}/k\right)}{2\pi r_{jc} A_{jcl} k \sigma J_B'\left(r_{jc}/k\right)} \right) \tag{4.60}$$

where r_{jc} is the conductor radius of the j-coil and U_{jcl} and A_{jcl} is the volume and cross sectional area of the j-coil respectively.

The transformer total resistive loss due to the AC resistance may be calculated as

$$S_{se} = 2 \sum_{j=\alpha,\beta} r_{jcl} i_{jcl}^2 \tag{4.61}$$

It should be noted that (4.61) includes the loss due the DC resistance.

Prior to evaluating the proximity effect loss in the transformer windings, it is required to calculate the dynamic resistance associated with each coil segment. To do so, the flux paths shown in Fig. 4.3 are considered. To simplify analysis, it is assumed, as done in Chapter 3, that the core is rectangular and infinitely permeable.

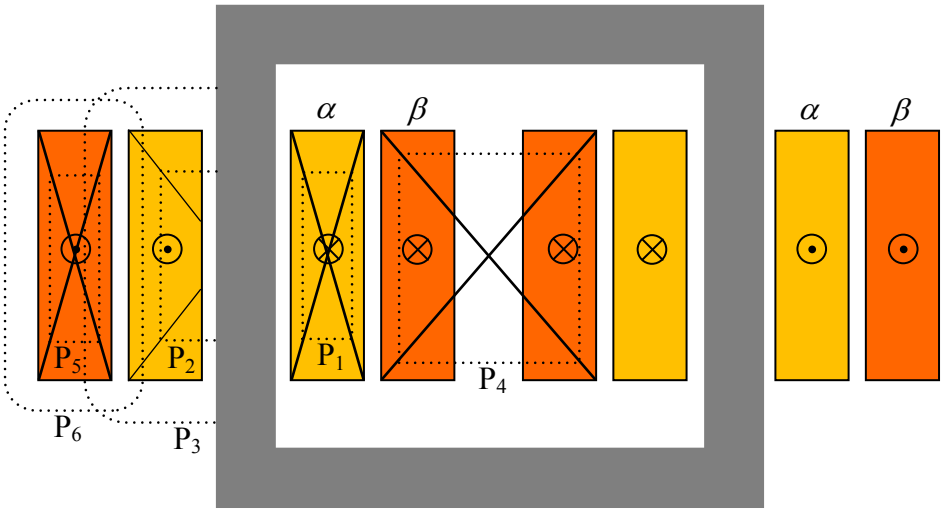

Fig. 4.3 Proximity Effect Flux Paths

4.3.1. Proximity Effect Loss in The Interior Segment of *α*-coil

It is noted that path P_1 in Fig. 4.3 is the same as path P_1 in Fig. 3.8. Therefore, the mean squared flux density associated with this path can be expressed in terms of the leakage permeance as

$$\left\langle \hat{B}_{\alpha p}^2 \right\rangle_{\alpha ir} = \frac{\mu_0 N_{\alpha cl}^2 P_{i\alpha li}}{U_{\alpha cl}} \tag{4.62}$$

and the dynamic resistance associated with the inner segment of α-coil is expressed as

$$r_{D_{\alpha ir}} = \frac{\mu_0 \pi N_{\alpha cl}^3 \sigma_{\alpha c} r_{\alpha c}^4 l_{\alpha i} P_{i\alpha li}}{4 U_{\alpha cl}} \tag{4.63}$$

where $\sigma_{\alpha c}$ and $r_{\alpha c}$ are the conductivity and radius of the α-coil conductor and $U_{\alpha cl}$ is the α-coil volume. The permeance $P_{i\alpha li}$ is calculated suing (3.44).

The proximity effect loss in the inner segment of α-coil is expressed as

$$\bar{S}_{p\alpha ir} = r_{D_{\alpha ir}} \overline{\left(\frac{di_{\alpha c}}{dt} \right)^2} \tag{4.64}$$

4.3.2. Proximity Effect Loss in The Exterior Segment of α-coil

As depicted in Fig. 4.3, there are two flux paths affecting the exterior segment of α-coil; path P_2 is caused by the coil self-leakage flux and path P_6 is due the flux produced by the exterior segment of β-coil. Due to the coupling, the result in (4.51)-(4.53) is used to obtain the proximity effect loss associated with the exterior segment of α-coil. To do so, the dynamic resistance associated with the exterior segment of α-coil is expressed as

$$r_{D_{\alpha er}} = \gamma_{\alpha er} \left\langle \begin{matrix} \hat{B}_{\alpha x}^2 + \hat{B}_{\alpha y}^2 & \hat{B}_{\alpha x}\hat{B}_{\beta x} + \hat{B}_{\alpha y}\hat{B}_{\beta y} \\ \hat{B}_{\alpha x}\hat{B}_{\beta x} + \hat{B}_{\alpha y}\hat{B}_{\beta y} & \hat{B}_{\beta x}^2 + \hat{B}_{\beta y}^2 \end{matrix} \right\rangle_{\alpha er} \tag{4.65}$$

To calculate the proximity effect loss in the exterior segment of α-coil, it is required to evaluate the elements of (4.65). To do so, Fig. 4.4 is considered.

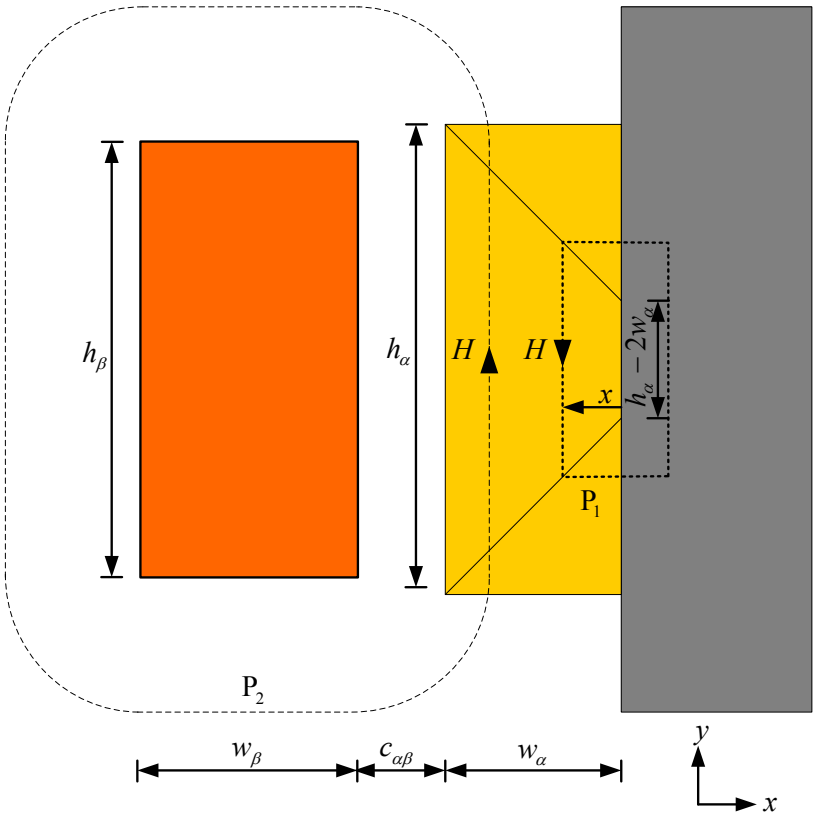

Fig. 4.4 Flux Paths Affecting the Exterior Segment of α-coil

Applying Ampere's law around the path P_1 in Fig. 4.4 yields

$$Hl_{p\alpha} = \frac{N_{\alpha cl} i_{\alpha c} a_{p\alpha}}{h_\alpha w_\alpha} \tag{4.66}$$

where $l_{p\alpha}$ is the path length and $a_{p\alpha}$ the area enclosed by the path, respectively. These are calculated as

$$l_{p\alpha} = |h_\alpha - 2w_\alpha| + 4x \qquad 0 < x < x_{\max} \tag{4.67}$$

$$a_{p\alpha} = x|h_\alpha - 2w_\alpha| + 2x^2 \qquad 0 < x < x_{\max} \tag{4.68}$$

where $x_{\max} = \min\left(\frac{h_\alpha}{2}, w_\alpha\right)$. One may notice from the result in (4.67) that the clearance between the exterior segment of α-coil and the core is neglected. This assumption simplifies the analysis but leads to slightly more pessimistic estimation of proximity effect loss in the coil segment. From (4.7), (4.49), and (4.66), the normalized flux density in the direction of the path is obtained

$$\hat{B}_{\alpha p} = \frac{\mu_0 N_{\alpha cl} a_{p\alpha}}{h_\alpha w_\alpha l_{p\alpha}} \tag{4.69}$$

Prior to evaluating $\left\langle \hat{B}_{\alpha x}^2 \right\rangle_{\alpha er}$ and $\left\langle \hat{B}_{\alpha y}^2 \right\rangle_{\alpha er}$, the value of $\left\langle \hat{B}_{\alpha p}^2 \right\rangle_{\alpha er}$ is first obtained. By substituting (4.67) and (4.68) into (4.69) and applying the spatial average definition in (4.46) to the square of the result one obtains

$$\left\langle \hat{B}_{\alpha p}^2 \right\rangle_{\alpha er} = \frac{\mu_0^2 N_{\alpha cl}^2}{h_\alpha^3 w_\alpha^3} \int_0^{x_{\max}} \frac{\left(x|h_\alpha - 2w_\alpha| + 2x^2\right)^2}{\left(|h_\alpha - 2w_\alpha| + 4x\right)^2} dA \tag{4.70}$$

To evaluate $\left\langle \hat{B}_{\alpha x}^2 \right\rangle_{\alpha er}$, the differential area of integration in (4.70) is expressed as

$$dA = 2x dx \tag{4.71}$$

Substituting (4.71) into (4.70) and integrating yields

$$\left\langle \hat{B}_{\alpha x}^2 \right\rangle_{\alpha er} = \frac{\mu_0^2 N_{\alpha cl}^2}{768 h_\alpha^3 w_\alpha^3} \left(24k_2^4 + 16\sqrt{2}k_2^3 k_1 - 6k_2^2 k_1^2 - \frac{3\sqrt{2}k_2 k_1^4}{2\sqrt{2}k_2 + k_1} + \frac{3k_1^4}{4} \ln\left(1 + \frac{8k_2^2 + 4\sqrt{2}k_2 k_1}{k_1^2}\right)\right) \tag{4.72}$$

where

$$k_1 = \left| h_\alpha - 2w_\alpha \right| \tag{4.73}$$

$$k_2 = \frac{1}{\sqrt{2}} \min\left(h_\alpha, 2w_\alpha \right) \tag{4.74}$$

To obtain $\left\langle \hat{B}_{\alpha y}^2 \right\rangle_{\alpha er}$ the differential area of integration in (4.70) is expressed as

$$dA = \left(\left| h_w - 2w_w \right| + 2x \right) dx \tag{4.75}$$

Substituting (4.75) into (4.70) and integrating yields

$$\left\langle \hat{B}_{\alpha y}^2 \right\rangle_{\alpha er} = \frac{\mu_0^2 N_{\alpha cl}^2}{768 h_\alpha^3 w_\alpha^3} \left(24k_2^4 + 32\sqrt{2}k_2^3 k_1 + 18k_2^2 k_1^2 - 6\sqrt{2}k_2 k_1^3 + \frac{3\sqrt{2}k_2 k_1^4}{2\sqrt{2}k_2 + k_1} + \frac{3k_1^4}{4} \ln\left(1 + \frac{8k_2^2 + 4\sqrt{2}k_2 k_1}{k_1^2} \right) \right) \tag{4.76}$$

To calculate $\left\langle \hat{B}_{\alpha y} \hat{B}_{\beta y} \right\rangle_{\alpha er}$, the path P_6 depicted in Fig. 4.3 is considered. As depicted in Fig. 4.4, the path length can be expressed as

$$l_{p\beta} = 2\left(h_\beta + w_\beta \right) + 2\pi y \tag{4.77}$$

where

$$y = \left(w_\alpha + c_{\alpha\beta} \right) - x \tag{4.78}$$

Applying Ampere's law around P_2 in Fig. 4.4 and the material relationship in (4.7), the normalized flux density is obtained

$$\hat{B}_{\beta p} = \frac{\mu_0 N_{\beta cl}}{l_{p\beta}} \tag{4.79}$$

Multiplying (6.69) by (6.79) and applying the spatial average definition in (4.46) to the result yields

$$\left\langle \hat{B}_{\alpha y} \hat{B}_{\beta y} \right\rangle_{\alpha er} = \frac{-\mu_0^2 N_{\alpha cl} N_{\beta cl}}{h_\alpha^2 w_\alpha^2} \int_0^{x_{\max}} \frac{a_{p\alpha}}{l_{p\alpha} l_{p\beta}} dA \tag{4.80}$$

The negative sign in (4.80) is due to the fact that the two flux paths are in in opposite directions. Substituting (6.67), (6.68), (6.75), and (6.77) into (4.80) and integrating yields

$$\left\langle \hat{B}_{\alpha y}\hat{B}_{\beta y}\right\rangle_{\alpha er}=\frac{\mu_0^2 N_{\alpha cl}N_{\beta cl}}{8\pi h_\alpha^2 w_\alpha^2\left(4k_\alpha+k_1\right)}\left(4k_2^2\left(k_1+4k_\beta\right)-2\sqrt{2}k_2\left(k_1^2-4\left(k_1+2k_\beta\right)^2\right)+\right.$$
$$\left.k_1^3\ln\left(1+\frac{2\sqrt{2}k_2}{k_1}\right)+16k_\beta\left(k_1+2k_\beta\right)^2\ln\left(1-\frac{k_2}{\sqrt{2}k_\beta}\right)\right) \tag{4.81}$$

where

$$k_\beta=\frac{1}{\pi}\left(h_\beta+w_\beta\right)+\left(w_\alpha+c_{\alpha\beta}\right) \tag{4.82}$$

The expression of $\left\langle \hat{B}_{\beta y}^2\right\rangle_{\alpha er}$, is obtained by substituting (4.77) into (4.79) and then applying the spatial average in (4.46) is applied to the square of the result

$$\left\langle \hat{B}_{\beta y}^2\right\rangle_{\alpha er}=\frac{\mu_0^2 N_{\beta cl}^2}{4h_\alpha w_\alpha}\int_{c_{\alpha\beta}}^{c_{\alpha\beta}+w_\alpha}\frac{1}{\left(h_\beta+w_\beta+\pi x\right)^2}dA \tag{4.83}$$

From Fig. 4.4, the differential area in (4.83) can be expressed as

$$dA=h_\alpha dy \tag{4.84}$$

Substituting (4.84) into (4.83) and integrating yields

$$\left\langle \hat{B}_{\beta y}^2\right\rangle_{\alpha er}=\frac{\mu_0^2 N_{\beta cl}^2}{4\left(h_\beta+w_\beta+\pi c_{\alpha\beta}\right)\left(h_\beta+w_\beta+\pi\left(c_{\alpha\beta}+w_\alpha\right)\right)} \tag{4.85}$$

As shown in Fig. 4.3, the flux path due to β-coil segment that couple the α-coil segment has only y-component and thus $\left\langle \hat{B}_{\beta x}^2\right\rangle_{\alpha er}$ and $\left\langle \hat{B}_{\alpha x}\hat{B}_{\beta x}\right\rangle_{\alpha er}$ are equal to zero.

Since all the parameters of $r_{D_{\alpha er}}$ are obtained, the proximity effect loss in the region inside the exterior segment of α-coil can be calculated using

$$\bar{S}_{p\alpha er}=\overline{\frac{di^T}{dt}r_{D_{\alpha er}}\frac{di}{dt}} \tag{4.86}$$

where

$$i=\left[i_{\alpha c}\quad i_{\beta c}\right]^T \tag{4.87}$$

4.3.3. Proximity Effect Loss in The Interior Segment of β-coil

To calculate the proximity effect loss in the inner segment of β-coil, path P_4 which depicted in Fig. 4.3 is considered. As shown, the path P_4 is similar to the path P_5 in Fig. 3.8. and thus the mean squared flux density associated with this path can be expressed in terms of the leakage permeance as

$$\left\langle \hat{B}_{\beta p}^2 \right\rangle_{\beta ir} = \frac{\mu_0 N_{\beta cl}^2 P_{i\beta li}}{U_{\beta cl}} \tag{4.88}$$

and the dynamic resistance associated with the inner segment of β-coil is expressed as

$$r_{D_{\beta ir}} = \frac{\mu_0 \pi N_{\beta cl}^3 \sigma_{\beta c} r_{\beta c}^4 l_{\beta i} P_{i\beta li}}{4U_{\beta cl}} \tag{4.89}$$

where $\sigma_{\beta c}$ and $r_{\beta c}$ are the conductivity and radius of the β-coil conductor and $U_{\beta cl}$ is the β-coil volume. The permeance $P_{i\beta li}$ is calculated using (3.54). As mentioned in Chapter 3, the permeance $P_{i\beta li}$ is only associated with one coil segment and thus it is equal to twice the value of the permeance associated with path P_4 in Fig. 4.3. Then the proximity effect in the region inside the coil segment is obtained

$$\overline{S}_{p\beta ir} = r_{D_{\beta ir}} \overline{\left(\frac{di_{\beta c}}{dt} \right)^2} \tag{4.90}$$

4.3.4. Proximity Effect Loss in The Exterior Segment of β-coil

As shown in Fig. 4.3, path P_5 is associated with the leakage flux due to Exterior Segment of β-coil and the path P_3 is associated with the leakage flux due to the exterior segment of α-coil. Similar to (4.66), the dynamic resistance is expressed as

$$r_{D_{\beta er}} = \gamma_{\beta er} \left\langle \begin{matrix} \hat{B}_{\alpha x}^2 + \hat{B}_{\alpha y}^2 & \hat{B}_{\alpha x}\hat{B}_{\beta x} + \hat{B}_{\alpha y}\hat{B}_{\beta y} \\ \hat{B}_{\alpha x}\hat{B}_{\beta x} + \hat{B}_{\alpha y}\hat{B}_{\beta y} & \hat{B}_{\beta x}^2 + \hat{B}_{\beta y}^2 \end{matrix} \right\rangle_{\beta er} \tag{4.91}$$

To evaluate the elements of (4.91), Fig. 4.5 is considered

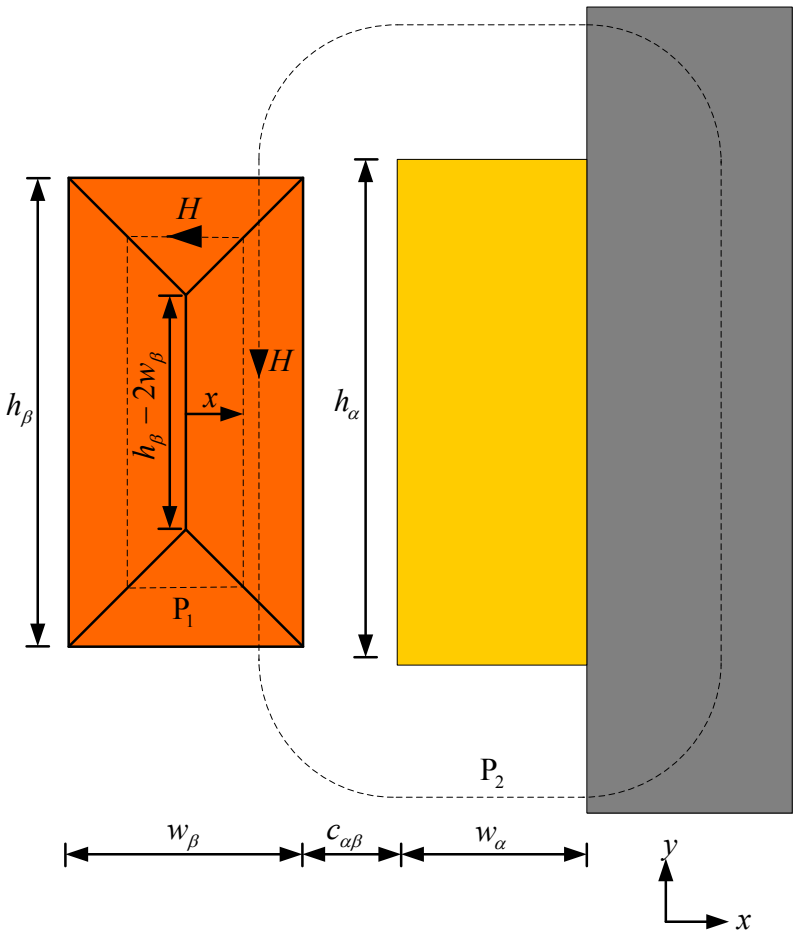

Fig. 4.5 Flux Paths Affecting the Exterior Segment of β-coil

Prior to evaluating $\left\langle \hat{B}_{\beta x}^2 \right\rangle_{\beta er}$ and $\left\langle \hat{B}_{\alpha y}^2 \right\rangle_{\beta er}$ the value of $\left\langle \hat{B}_{\beta p}^2 \right\rangle_{\beta er}$ is first obtained by considering the path P_1 in Fig. 4.5. The normalized flux density can be obtained by applying Ampere's law around this path

$$\hat{B}_{\beta p} = \frac{\mu_0 N_{\beta cl} a_{p\beta}}{h_\alpha w_\alpha l_{p\beta}} \tag{4.92}$$

where

$$l_{p\beta} = 2\left|h_\beta - 2w_\beta\right| + 8x \tag{4.93}$$

$$a_{p\beta} = 2x\left|h_\beta - 2w_\beta\right| + 4x^2 \tag{4.94}$$

Substituting (4.93) and (4.94) into (4.92) and applying the spatial average definition to the result yields

$$\left\langle \hat{B}_{\beta p}^2 \right\rangle_{\beta er} = \frac{\mu_0^2 N_{\beta cl}^2}{h_\beta^3 w_\beta^3} \int_0^{x_{\max}} \frac{\left(x\left|h_\beta - 2w_\beta\right| + 2x^2 \right)^2}{\left(\left|h_\beta - 2w_\beta\right| + 4x \right)^2} dA \tag{4.95}$$

where $x_{\max} = \min\left(\frac{h_\beta}{2}, \frac{w_\beta}{2} \right)$.

To evaluate $\left\langle \hat{B}_{\beta x}^2 \right\rangle_{\beta er}$, the differential area of integration in (4.95) is expressed as

$$dA = 4x dx \tag{4.96}$$

By substituting (4.96) into (4.95) and integrating one obtains

$$\left\langle \hat{B}_{\beta x}^2 \right\rangle_{\beta er} = \frac{\mu_0^2 N_{\beta cl}^2}{768 h_\beta^3 w_\beta^3} \left(12k_2^4 + 16k_2^3 k_1 - 6k_2^2 k_1^2 - \frac{3k_2 k_1^4}{2k_2 + k_1} + \frac{3k_1^4}{2} \ln\left(1 + \frac{4k_2^2 + 4k_2 k_1}{k_1^2} \right) \right) \tag{4.97}$$

where

$$k_1 = \left| h_\beta - w_\beta \right| \tag{4.98}$$

$$k_2 = \min\left(h_\beta, w_\beta \right) \tag{4.99}$$

Similarly,

$$\left\langle \hat{B}_{\beta y}^2 \right\rangle_{\beta er} = \frac{\mu_0^2 N_{\beta cl}^2}{768 h_\beta^3 w_\beta^3} \left(12k_2^4 + 32k_2^3 k_1 + 18k_2^2 k_1^2 - 12k_2 k_1^3 + \frac{3k_2 k_1^4}{2k_2 + k_1} + \frac{3k_1^4}{2} \ln\left(1 + \frac{4k_2^2 + 4k_2 k_1}{k_1^2} \right) \right) \tag{4.100}$$

To calculate $\left\langle \hat{B}_{\alpha y}^2 \right\rangle_{\beta er}$, the path P_2 depicted in Fig. 4.5 is considered. Assuming that the core is infinitely permeable, the path length can be expressed as

$$l_{p\alpha} = h_\alpha + 2w_\alpha + \pi y \tag{4.101}$$

where

$$y = \left(\frac{w_\beta}{2} + c_{\alpha\beta} \right) - x \tag{4.102}$$

Applying Ampere's law around P_2 in Fig. 4.5 and the material relationship in (4.7), the normalized flux density is obtained

$$\hat{B}_{\alpha p} = \frac{\mu_0 N_{\alpha cl}}{l_{p\alpha}} \tag{4.103}$$

Multiplying (6.103) by (6.92) and applying the spatial average definition in (4.46) to the result yields

$$\left\langle \hat{B}_{\alpha y} \hat{B}_{\beta y} \right\rangle_{\beta er} = \frac{-\mu_0^2 N_{\alpha cl} N_{\beta cl}}{h_\beta^2 w_\beta^2} \int_{c_{\alpha\beta}}^{c_{\alpha\beta}+w_\alpha} \frac{a_{p\beta}}{l_{p\alpha} l_{p\beta}} dA \tag{4.104}$$

The differential area of integration in (4.104) is expressed as

$$dA = 2\left(\left|h_\beta - 2w_\beta\right| + 2x\right)dx \tag{4.105}$$

Substituting (4.93), (4.94), (4.101), and (4.105) into (4.104) and integrating yields

$$\left\langle \hat{B}_{\alpha y} \hat{B}_{\beta y} \right\rangle_{\beta er} = \frac{\mu_0^2 N_{\alpha cl} N_{\beta cl}}{8\pi h_\beta^2 w_\beta^2 \left(4k_\alpha + k_1\right)} \left(2k_2^2\left(k_1 + 4k_\alpha\right) - 2k_2\left(k_1^2 - 4\left(k_1 + 2k_\alpha\right)^2\right) + k_1^3 \ln\left(1 + \frac{2k_2}{k_1}\right) + 16k_\alpha\left(k_1 + 2k_\alpha\right)^2 \ln\left(1 - \frac{k_2}{2k_\alpha}\right)\right) \tag{4.106}$$

where

$$k_\alpha = \frac{1}{\pi}\left(h_\alpha + 2w_\alpha\right) + \left(\frac{w_\beta}{2} + c_{\alpha\beta}\right) \tag{4.107}$$

The expression of $\left\langle \hat{B}_{\alpha y}^2 \right\rangle_{\beta er}$ is obtained by substituting (4.101) into (4.103) and then applying the spatial average in (4.46) is applied to the square of the result

$$\left\langle \hat{B}_{\alpha p}^2 \right\rangle_{\beta er} = \frac{\mu_0^2 N_{\alpha cl}^2}{h_\beta w_\beta} \int_{c_{\alpha\beta}}^{c_{\alpha\beta}+w_\beta} \frac{1}{\left(h_\alpha + 2w_\alpha + \pi x\right)^2} dA \tag{4.108}$$

From Fig. 4.5, the differential area in (4.108) can be expressed as

$$dA = h_\beta dy \tag{4.109}$$

By substituting (4.109) into (4.108) and integrating one obtains

$$\left\langle \hat{B}_{\alpha y}^2 \right\rangle_{\beta er} = \frac{\mu_0^2 N_{\alpha cl}^2}{\left(h_\alpha + 2w_\alpha + \pi c_{\alpha\beta}\right)\left(h_\alpha + 2w_\alpha + \pi\left(c_{\alpha\beta} + w_\beta\right)\right)} \tag{4.110}$$

As shown in Fig. 4.5, the flux path due to α-coil segment that couple the β-coil segment has only y-component and thus $\left\langle \hat{B}_{\alpha x}^2 \right\rangle_{\beta er}$ and $\left\langle \hat{B}_{\alpha x} \hat{B}_{\beta x} \right\rangle_{\beta er}$ are equal to zero.

The proximity effect loss in the region inside the exterior segment of β-coil can be calculated using

$$\bar{S}_{p\beta er} = \overline{\frac{di^T}{dt} r_{D_{\beta er}} \frac{di}{dt}} \tag{4.111}$$

where

$$i = [i_{\alpha c} \quad i_{\beta c}]^T \tag{4.112}$$

The total proximity loss effect is equal to the sum of the proximity effect in all coil segments. Since each winding has to coils, the total proximity effect loss in the transformer windings is calculated as

$$S_{pe} = 2\left(\bar{S}_{p\alpha ir} + \bar{S}_{p\alpha er} + \bar{S}_{p\beta ir} + \bar{S}_{p\beta er}\right) \tag{4.113}$$

Finally, the transformer total resistive loss are calculated using

$$S_{rl} = S_{se} + S_{pe} \tag{4.114}$$

5. THERMAL EQUIVALENT CIRCUIT (TEC)

When the design of electromagnetic devices such as a transformer is considered, it is desired to accurately predict the temperature within the device. In Chapter 7, constraints on temperature of the coil and core are imposed. In this chapter, a thermal equivalent circuit (TEC) is derived to predict the temperature throughout the transformer core and coils.

5.1. Thermal Equivalent Circuit of Cuboidal Element

To a TEC of a cuboid is first considered. To do so, the heat equation of the cuboidal element Ω shown in Fig. 5.1 is expressed as [13]

$$\frac{de_\Omega}{dt} = p_\Omega + k_{\Omega x}\frac{\partial^2 T_\Omega}{\partial x^2} + k_{\Omega y}\frac{\partial^2 T_\Omega}{\partial y^2} + k_{\Omega z}\frac{\partial^2 T_\Omega}{\partial z^2} \tag{5.1}$$

where e_Ω and p_Ω are the thermal energy and power loss densities within the cuboid, respectively, $k_{\Omega x}$, $k_{\Omega y}$, and $k_{\Omega z}$ are the thermal conductivities along the x-, y-, and z- axes respectively, and T_Ω is the temperature at an arbitrary location within the element. For simplicity, the heat flow is assumed to be independent in each axis and thus the solution of (5.1) is of the form [13]

$$T_\Omega = c_{2x}x^2 + c_{1x}x + c_{2y}y^2 + c_{1y}y + c_{2z}z^2 + c_{1z}z + c_0 \tag{5.2}$$

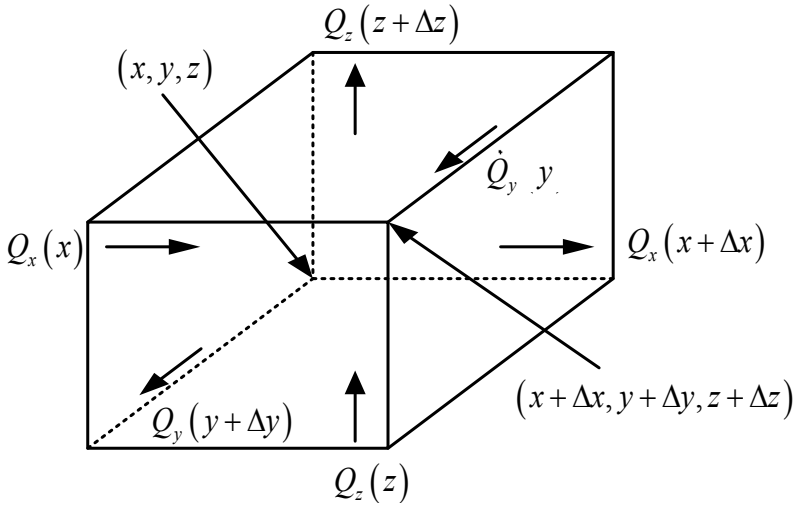

Fig. 5.1 Cuboidal Element

To begin the derivation, the mean temperature over the cuboid is defined as

$$\langle T_\Omega \rangle = \frac{1}{U_\Omega} \int_{U_\Omega} T_\Omega dU \tag{5.3}$$

where U_Ω is the volume of the cuboid. Applying (5.3) to (5.2) yields

$$\langle T_\Omega \rangle = \frac{1}{3} c_{2x} l_{\Omega x}^2 + \frac{1}{2} c_{1x} l_{\Omega x} + \frac{1}{3} c_{2y} l_{\Omega y}^2 + \frac{1}{2} c_{1y} l_{\Omega y} + \frac{1}{3} c_{2z} l_{\Omega z}^2 + \frac{1}{2} c_{1z} l_{\Omega z} + c_0 \tag{5.4}$$

The mean temperature on the plane $x = 0$ is obtained by applying (5.3) to (5.2) at $x = 0$; thus,

$$\langle T_{\Omega 0x} \rangle = \frac{1}{3} c_{2y} l_{\Omega y}^2 + \frac{1}{2} c_{1y} l_{\Omega y} + \frac{1}{3} c_{2z} l_{\Omega z}^2 + \frac{1}{2} c_{1z} l_{\Omega z} + c_0 \tag{5.5}$$

Similarly, the mean temperature at $x = l_{\Omega x}$ is expressed as

$$\langle T_{\Omega lx} \rangle = c_{2x} l_{\Omega x}^2 + c_{1x} l_{\Omega x} + \frac{1}{3} c_{2y} l_{\Omega y}^2 + \frac{1}{2} c_{1y} l_{\Omega y} + \frac{1}{3} c_{2z} l_{\Omega z}^2 + \frac{1}{2} c_{1z} l_{\Omega z} + c_0 \tag{5.6}$$

From (5.4)-(5.6), one can show that

$$\langle T_{\Omega 0x} \rangle = \langle T_\Omega \rangle - \frac{1}{3} c_{2x} l_{\Omega x}^2 - \frac{1}{2} c_{1x} l_{\Omega x} \tag{5.7}$$

and

$$\langle T_{\Omega lx} \rangle = \langle T_{\Omega} \rangle + \frac{2}{3} c_{2x} l_{\Omega x}^2 + \frac{1}{2} c_{1x} l_{\Omega x} \tag{5.8}$$

According to Fourier's law, the heat flow in a material can be expressed as [13]

$$\mathrm{q} = -\left(k_{\Omega x} \frac{\partial T_{\Omega}}{\partial x} \mathrm{a}_x + k_{\Omega y} \frac{\partial T_{\Omega}}{\partial y} \mathrm{a}_y + k_{\Omega z} \frac{\partial T_{\Omega}}{\partial z} \mathrm{a}_z \right) \tag{5.9}$$

where a_x, a_y, and a_z are unit vectors in the x-, y-, and z- directions respectively. The thermal flux through a surface Γ is obtained using

$$Q_{\Gamma} = \int_{A_{\Gamma}} \mathrm{q}.dA \tag{5.10}$$

where A_{Γ} is the area of the surface Γ.

Substituting (5.2) into (5.9) and placing the result in (5.10), the heat flux at the planes $x = 0$ and $x = l_{\Omega x}$ can be obtained

$$Q_{\Omega 0x} = -c_{1x} k_{\Omega x} l_{\Omega y} l_{\Omega z} \tag{5.11}$$

$$Q_{\Omega lx} = -\left(2c_{2x} l_{\Omega x} + c_{1x}\right) k_{\Omega x} l_{\Omega y} l_{\Omega z} \tag{5.12}$$

From (5.11) and (5.12)

$$c_{1x} = -\frac{Q_{\Omega 0x}}{k_{\Omega x} l_{\Omega y} l_{\Omega z}} \tag{5.13}$$

$$c_{2x} = \frac{Q_{\Omega 0x} - Q_{\Omega lx}}{2k_{\Omega x} l_{\Omega x} l_{\Omega y} l_{\Omega z}} \tag{5.14}$$

By substituting (5.13) and (5.14) into (5.7) and (5.8) one can obtain

$$\langle T_{\Omega 0x} \rangle = T_{\Omega cx} + R_{\Omega x} \dot{Q}_{\ x} \tag{5.15}$$

and

$$\langle T_{\Omega lx} \rangle = T_{\Omega cx} - R_{\Omega x} \dot{Q}_{\ lx} \tag{5.16}$$

where

$$R_{\Omega x} = \frac{l_{\Omega x}}{2k_{\Omega x} A_{\Omega x}} \tag{5.17}$$

and

$$T_{\Omega cx} \quad \langle T_\Omega \rangle - \frac{1}{3} R_{\Omega x} \left(Q_{\Omega 0 x} - Q_{\Omega l x} \right) \tag{5.18}$$

Repeating along the y- axis yields

$$c_{1y} = -\frac{Q_{\Omega 0 y}}{k_{\Omega y} l_{\Omega x} l_{\Omega z}} \tag{5.19}$$

$$c_{2y} = \frac{Q_{\Omega 0 y} - Q_{\Omega l y}}{2 k_{\Omega y} l_{\Omega x} l_{\Omega y} l_{\Omega z}} \tag{5.20}$$

The mean temperature on the plane $y = 0$ and $y = l_{\Omega y}$ are

$$\left\langle T_{\Omega 0 y} \right\rangle = T_{\Omega cy} + R_{\Omega y} Q_{\Omega 0 y} \tag{5.21}$$

and

$$\left\langle T_{\Omega l y} \right\rangle = T_{\Omega cy} - R_{\Omega y} Q_{\Omega l y} \tag{5.22}$$

where

$$R_{\Omega y} = \frac{l_{\Omega y}}{2 k_{\Omega y} A_{\Omega y}} \tag{5.23}$$

and

$$T_{\Omega cy} \quad \langle T_\Omega \rangle - \frac{1}{3} R_{\Omega y} \left(Q_{\Omega 0 y} - Q_{\Omega l y} \right) \tag{5.24}$$

and along the z- axis, it yields

$$c_{1z} = -\frac{Q_{\Omega 0 z}}{k_{\Omega z} l_{\Omega x} l_{\Omega y}} \tag{5.25}$$

$$c_{2z} = \frac{Q_{\Omega 0 z} - Q_{\Omega l z}}{2 k_{\Omega z} l_{\Omega x} l_{\Omega y} l_{\Omega z}} \tag{5.26}$$

The mean temperature on the plane $z = 0$ and $z = l_{\Omega z}$ are

$$\left\langle T_{\Omega 0 z} \right\rangle = T_{\Omega cz} + R_{\Omega z} Q_{\Omega 0 z} \tag{5.27}$$

and

$$\left\langle T_{\Omega l z} \right\rangle = T_{\Omega cz} - R_{\Omega z} Q_{\Omega l z} \tag{5.28}$$

where

$$R_{\Omega z} = \frac{l_{\Omega z}}{2k_{\Omega z}A_{\Omega z}} \tag{5.29}$$

and

$$T_{\Omega cz} \quad \langle T_\Omega \rangle - \frac{1}{3} R_{\Omega z} \left(Q_{\Omega 0 z} - Q_{\Omega l z} \right) \tag{5.30}$$

Using (5.13), (5.14), (5.19), (5.20), (5.25), and (5.26) in (5.2) and substituting into (5.1) yields

$$\frac{de_\Omega}{dt} = p_\Omega + \frac{1}{U_\Omega}\left(Q_{\Omega 0 x} - Q_{\Omega l x} + Q_{\Omega 0 y} - Q_{\Omega l y} + Q_{\Omega 0 z} - Q_{\Omega l z} \right) \tag{5.31}$$

Since e_Ω is independent of position, the total time changing energy in the volume can be obtained by multiplying (5.23) by the volume

$$\frac{dE_\Omega}{dt} = P_\Omega + Q_{\Omega 0 x} - Q_{\Omega l x} + Q_{\Omega 0 y} - Q_{\Omega l y} + Q_{\Omega 0 z} - Q_{\Omega l z} \tag{5.32}$$

where P_Ω is the power dissipated in the cuboid and E_Ω is the thermal energy. Since the thermal analysis is performed in steady state

$$\frac{dE_\Omega}{dt} = 0 \tag{5.33}$$

Equations (5.15)-(5.18), (5.21)-(5.24), and (5.27)-(5.33) represent the basis of the thermal equivalent circuit of a cuboidal element that is illustrated in Fig. 5.2. Specifically, R represents the resistance to heat flow, T is analogous to electric potential, and $\dot{\zeta}$ (heat flow) is analogous to current.

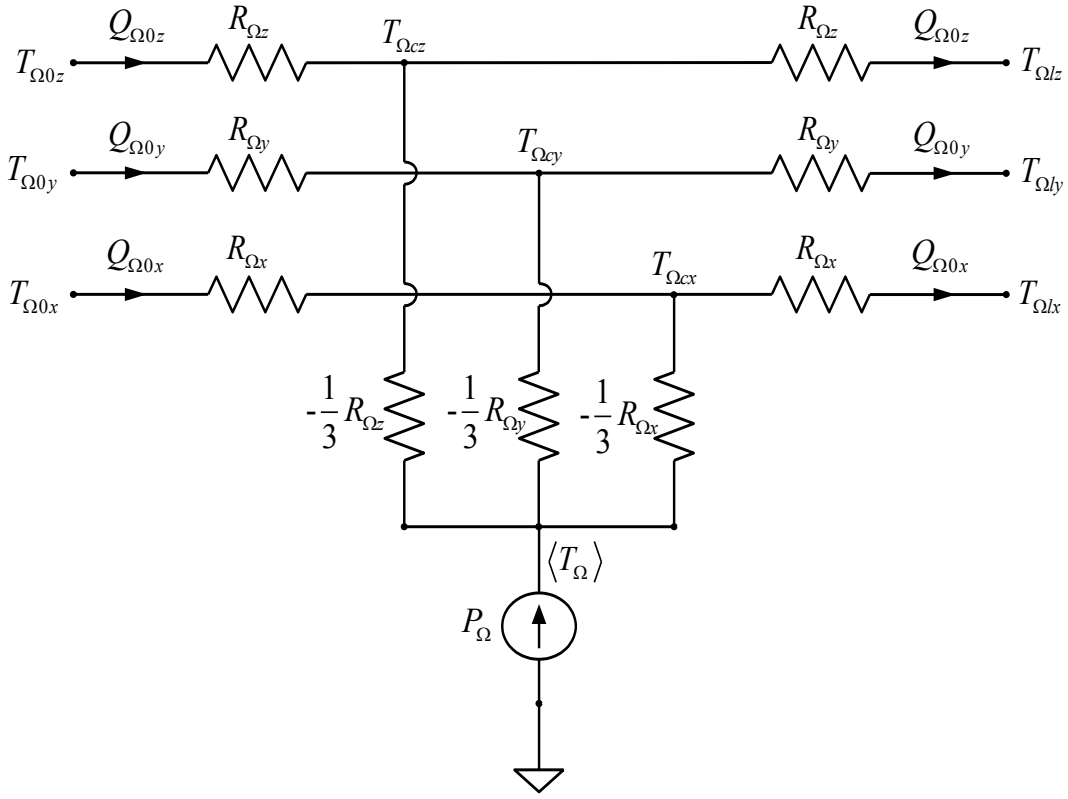

Fig. 5.2 Thermal Equivalent Circuit of a Cuboidal Element

5.2. Peak Temperature

From Fig. 5.2 one can observe that given the power dissipated in a cube, cube dimensions, and the surface temperatures, $\langle T_\Omega \rangle$ and $T_{\Omega cx}$, $T_{\Omega cy}$, and $T_{\Omega cz}$ are readily obtained. However, it is often necessary to calculate peak temperature. Typically, it is desired to limit the peak temperature of an electromagnetic device. To do so, (5.2) is first expressed in a form:

$$T_\Omega = T_x + T_y + T_z + c_0 \tag{5.34}$$

where

$$T_i = c_{2i} i^2 + c_{1i} i \tag{5.35}$$

and $i = x, y,$ or z.

To obtain c_0 in (5.34), one can use (5.4), (5.13), (5.14), (5.19), (5.20), (5.25), and (5.26).

By taking the derivative of (5.34) and equating the answer to zero, one can yield

$$i_e = -\frac{c_{1i}}{2c_{2i}} \ , \quad c_{2i} \neq 0 \tag{5.36}$$

The extremum (minimum or maximum) value of T_i is obtained by substituting (5.36) into (5.35) which yields

$$T_{ei} = -\frac{c_{1i}^2}{4c_{2i}} \ , \quad c_{2i} \neq 0 \tag{5.37}$$

Considering that T_{ei} could be a minimum and c_{2i} could be zero, the i-component of the cuboid peak temperature is expressed as

$$T_{\mathrm{i},pk} = \begin{cases} \max\left(T_{\Omega 0i}, T_{\Omega li}\right) \ , & c_{2i} = 0 \text{ or } \left(c_{2i} \neq 0 \text{ and } \left(i_e < 0 \text{ or } i_e > l_{\Omega i}\right)\right) \\ \max\left(T_{\Omega 0i}, T_{ei}, T_{\Omega li}\right) \ , & c_{2i} \neq 0 \text{ and } 0 \leq i_e \leq l_{\Omega i} \end{cases} \tag{5.38}$$

Using (5.38), the peak temperature along the x-, y- and z-axis are evaluated and then the peak temperature of the cuboid is obtained

$$T_{\Omega,pk} = T_{x,pk} + T_{y,pk} + T_{z,pk} + c_0 \tag{5.39}$$

5.3. Transformer Thermal Model

In the previous sections, the thermal equivalent circuit of a cuboidal element was derived. In this section, this circuit will be used as the basis for deriving the transformer thermal equivalent circuit. To set the stage, the transformer is divided into 14 cuboids. Assuming thermal symmetry, only one-eighth of the transformer is analyzed as depicted in Fig. 5.3, Cuboids A, B, C, and F represent the transformer core, cuboids E, G, I, J, and K represent the α-coil, and cuboids D, H, L, M, and N represent the β-coil.

Prior to deriving the TEC, two issues need to be resolved. First, as illustrated in Fig. 5.3, cuboids C, I, K, L, and M are not rectangular. However, the thermal equivalent circuit discussed in Section 5.1 was derived for a rectangular element. In addition, each transformer coil is composed of a conductor surrounded by an insulation and air which makes representing the transformer coils in the TEC a challenge.

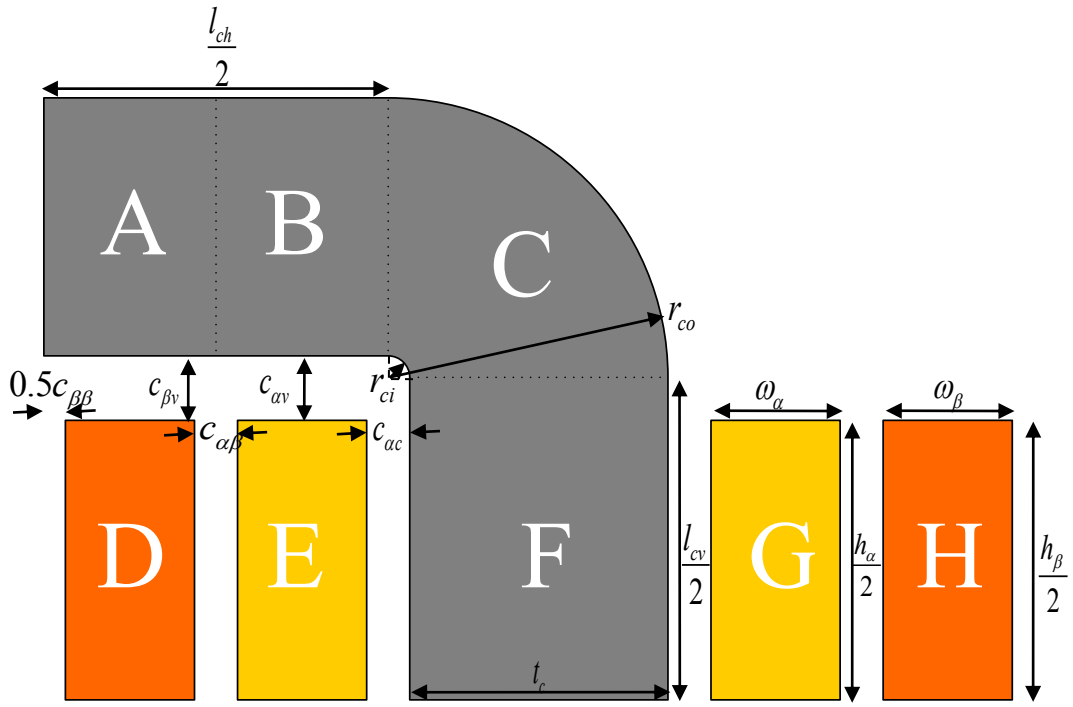

(a) Front Cross-Sectional View

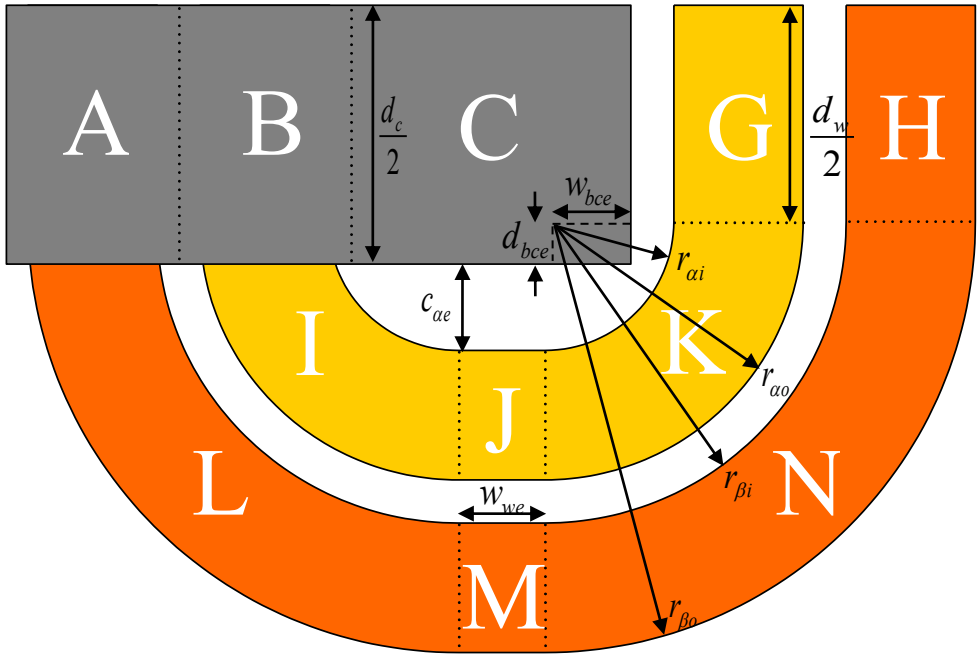

(b) Top View

Fig. 5.3 Cuboids of a Tape-Wound Transformer

5.3.1. Coil Homogenization

When transformer coils are considered for thermal analysis, representing each material separately is a challenge. The reason is that each coil turn is composed of a conductive material with a thermal conductivity k_c surrounded by an insulating material with a thermal conductivity k_i in addition to the air with a thermal conductivity k_a which occupies the region between the conductors as shown in Fig. 5.4 (a). Therefore, prior to deriving its thermal equivalent circuit, homogenization of the coil is convenient [13].

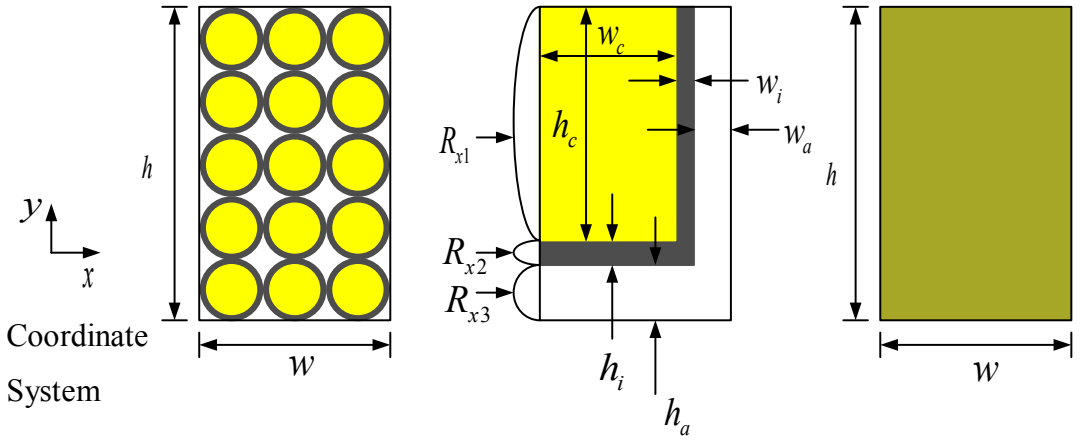

(a) Coil (b) Dimensions of Effective Materials (c) Homogenized Coil

Fig. 5.4 Coil Homogenization

To set the stage, the coil in Fig. 5.4 is considered. The width of the coil is assumed to be w and the height is assumed to be h. The coil is assumed to have N conductors, each with a radius of r_c and an insulation thickness of t_i. The basis of the homogenization process is to keep the areas of each material fixed. The cross-sectional areas of the conductor, insulation, and air are expressed as

$$a_c = N\pi r_c^2 \tag{5.40}$$

$$a_i = N\pi\left(\left(r_c + t_i\right)^2 - r_c^2\right) \tag{5.41}$$

$$a_a = wh - a_c - a_i \tag{5.42}$$

The coil aspect ratio is defined as

$$\zeta = \frac{w}{h} \tag{5.43}$$

The next step is to calculate the dimensions of an effective material shown in Fig. 5.4 (b). These dimensions are calculated such that the area of each material is kept the same as the original coil (Fig. 5.4 (a)). Furthermore, the aspect ratio of each material must be equal to the aspect ratio evaluated using (5.43).

The yellow rectangle shown in Fig. 5.4 (b) represents the effective dimensions of conductor material. In order to maintain the same conductor area and the coil aspect ratio, it is required that

$$w_c h_c = a_c \tag{5.44}$$

and

$$\frac{w_c}{h_c} = \zeta \tag{5.45}$$

where h_c and w_c are the effective height and width of the conductor material respectively. By solving (5.44) and (5.45) one obtains

$$w_c = \sqrt{a_c \zeta} \tag{5.46}$$

$$d_c = \sqrt{\frac{a_c}{\zeta}} \tag{5.47}$$

Similarly, to keep the same area for the insulating material (the gray region in Fig. 5.4 (b)) and the same aspect ratio, one can observe that

$$\left(w_c + w_i\right)\left(h_c + h_i\right) = a_i \tag{5.48}$$

and

$$\frac{w_i}{h_i} = \zeta \tag{5.49}$$

where h_i and w_i are the effective height and width of the insulation material respectively. Solving (5.48) and (5.49) yields

$$h_i = \sqrt{h_c^2 + \frac{a_i}{\zeta}} - h_c \tag{5.50}$$

$$w_i = h_i \zeta \tag{5.51}$$

Finally, the dimensions of the white region in Fig. 5.4 (b) which represent the effective area of the air can be obtained using

$$w_a = w - w_c - w_i \tag{5.52}$$

$$h_a = h - h_c - h_i \tag{5.53}$$

where h_a and w_a are the effective height and width of the surrounding air respectively. Using (5.52) and (5.53) it can also be shown that the area and the aspect ratio of the effective air region is kept the same.

Using (5.46), (5.47), and (5.50)-(5.53), the coil of Fig. 5.4 (a) is replaced geometrically with Fig. 5.4 (b).

Since the aspect ratio is kept the same for all regions, the thermal conductivity of the homogenized region will be the same in the x- and y- directions. If the x-direction is considered then the three parallel thermal resistances of this effective material representation shown in Fig. 5.4 (b) can be calculated as

$$R_{x1} = \frac{w_c}{k_c h_c l} + \frac{w_i}{k_i h_c l} + \frac{w_a}{k_a h_c l} \tag{5.54}$$

$$R_{x2} = \frac{w_c + w_i}{k_c h_i l} + \frac{w_a}{k_a h_i l} \tag{5.55}$$

$$R_{x3} = \frac{w}{k_a h_a l} \tag{5.56}$$

where l is the coil length in the z- direction. The parallel combination of the three thermal resistances is expressed as

$$R_x = \frac{1}{\frac{1}{R_{x1}} + \frac{1}{R_{x2}} + \frac{1}{R_{x3}}} \tag{5.57}$$

To further simplify and replace Fig. 5.4 (b) with a uniform material of Fig. 5.4 (c), the thermal conductivity of the homogenized material in the x- and y- directions is denoted k_{xyh}, and the thermal resistance is expressed as

$$R_x = \frac{w}{k_{xyh} lh} \tag{5.58}$$

Substituting (5.54)-(5.56) into (5.57) and equating the result to (5.58) yields,

$$k_{xyh} = \frac{1}{\frac{1}{k_c} + \frac{h_i}{k_i h_c} + \frac{h_a}{k_a h_c}} + \frac{1}{\frac{h_c + h_i}{k_i h_i} + \frac{h_a}{k_a h_i}} + \frac{1}{\frac{h}{k_a h_a}} \tag{5.59}$$

Although, the thermal conductivity is the same in the x- and y- directions, the homogenized material will be anisotropic. This is because the thermal conductivity in the z- direction is different. As shown in Fig. 5.4 (b), the conductor material is continuous and thus the homogenized material will have a good thermal conductivity in the z- direction. This is because most of the heat flux will run through the conductive material. The thermal resistance of the homogenized material in the z- direction is equal to the parallel combination of the resistances of the three different materials. Therefore,

$$R_z = \frac{1}{\frac{a_c k_c}{l} + \frac{a_i k_i}{l} + \frac{a_a k_a}{l}} \tag{5.60}$$

If the thermal conductivity of the homogenized material in the z- direction is denoted k_{zh}, then the thermal resistance in the z- direction can also be expressed as

$$R_z = \frac{w}{k_{zh} wh} \tag{5.61}$$

After equating (5.60) to (5.61) and simplifying,

$$k_{zh} = \frac{a_c k_c + a_i k_i + a_a k_a}{wd} \tag{5.62}$$

Consequently, the coil shown in Fig. 5.4 (a) is replaced by anisotropic homogenized material shown in Fig. 5.4 (c) with a thermal conductivity k_{xyh} in the x- and y- directions and a thermal conductivity of k_{zh} in the z- direction. Now the stage is set for the derivation of the transformer thermal equivalent circuit (TEC).

5.3.2. Rounded Corner Element Representation

As discussed earlier, some of the transformer cuboids are not rectangular. A relatively straight forward approach to tackle this problem is to represent these elements as effective rectangular cuboids. The effective cuboid is derived on the basis that the total surface area in each direction is maintained the same.

To calculate the dimensions of the effective material, the corner element depicted in Fig. 5.5(a) is considered. This element is reflective of the elements labeled 'I', 'K', 'L' and 'N' in Fig. 5.4 (b). The area in the y- direction (direction into page) of the corner element is expressed as

$$A_y = \frac{\pi}{4} w(r_o + r_i) \tag{5.63}$$

As shown in Fig. 5.5(b), the area of the effective element in the y- direction is

$$A_e = w l_e \tag{5.64}$$

where l_e is the effective length. Since it is desired to keep the same area, then (5.63) and (5.64) must be equal; as a result,

$$l_e = \frac{\pi}{4}(r_o + r_i) \tag{5.65}$$

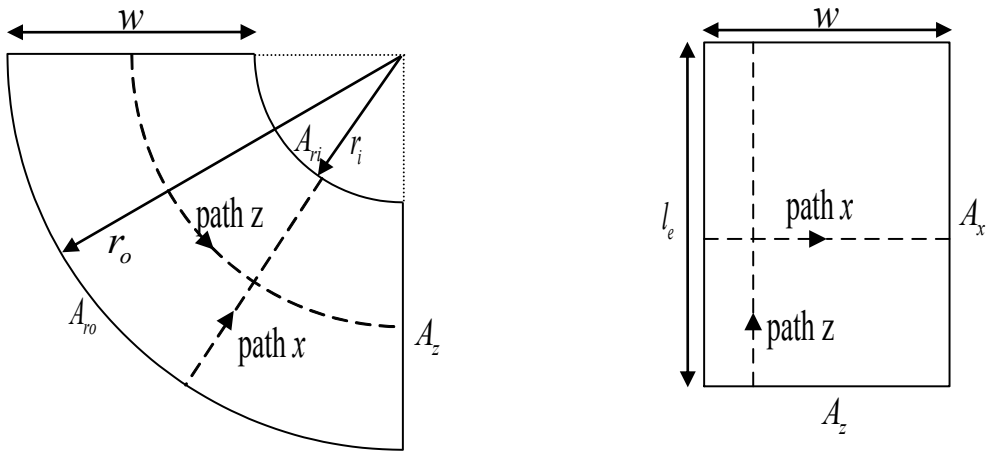

(a) Anisotropic corner element (b) Effective corner element

Fig. 5.5 Corner Element Representation

As shown in Fig. 5.5, the cuboid area in the z-direction A_z is maintained the same, in the x-direction the total area is maintained

$$A_{ro} + A_{ri} = 2A_x \tag{5.66}$$

where A_x is the area of the effective cuboid in the x-direction, A_{ri} is the area of the corner element in x-direction at the winding inner radius, and A_{r0} is the area of the corner element in the x-direction at the winding outer radius as depicted in Fig. 5.5. The result in (5.66) means that the contact area between the element and the ambient is the same for the corner element and the effective element which is the desired result.

For element 'C', a similar result can be obtained. This is done by considering Fig. 5.5 and assuming that the x-axis is in the angular direction, the y-axis is in radial direction, and the z-axis is into the page; Thus,

$$A_z = wl_e \tag{5.67}$$

and

$$A_{ro} + A_{ri} = 2A_y \tag{5.68}$$

5.3.3. Transformer Thermal Equivalent Circuit (TEC)

Using the results in the previous sections, the transformer thermal equivalent circuit depicted in Fig. 5.6 is derived. Each cuboid is thermally represented by the equivalent cuboidal circuit of Fig. 5.2. To simplify representation, following the notation of [13] each cuboid is replaced by a rectangle that shows the cuboid name and nodes as shown in Fig. 5.6.

As shown in Fig 5.6, some cuboids are thermally connected to each other through air. This is accomplished using a thermal resistance (gray rectangles in Fig. 5.6) which depend on the contact area A_{ij} and the clearance c_{ij} between cuboids i and j; where both i and j could be any cuboid 'A' through 'N'. The thermal resistance between cuboids i and j is expressed as

$$R_{ij} = \frac{c_{ij}}{A_{ij}k_a} \tag{5.69}$$

where k_a is thermal conductivity of air.

To be specific, the $0y$ node of 'A' is connected to the $1y$ node of 'D' through R_{AD}. The resistance R_{AD} can be obtained using (5.69) by setting $c_{AD} = c_{\beta v}$. The contact area is selected to be the average area between the two cuboids, i.e., $A_{AD} = \left(0.5(c_{\beta\beta} + c_{\alpha\beta}) + 2w_\beta\right) d_c / 4$.

Similarly, the $0y$ node of 'B' is connected to the $1y$ node of 'E' through R_{BE}. By setting $c_{BE} = c_{\alpha v}$ and $A_{BE} = \left(0.5c_{\alpha\beta} + c_{\alpha c} + 2w_\alpha - r_{ci}\right) d_c / 4$, R_{BE} is obtained.

The $0x$ node of 'F' is connected to the $1x$ node of 'E' through R_{EF}. The resistance R_{EF} is obtained using (5.69) by setting $c_{EF} = c_{\alpha c}$ and the contact area is expressed as $A_{EF} = \left(l_{ch} + h_\alpha\right) d_c / 8$. It is noted that the resistance R_{FG} which connects nodes $0x$ and $1x$ of cuboids 'G' and 'F' respectively is equal to R_{EF}.

The $0z$ node of 'F' is connected to the $1x$ node of 'J' through R_{FJ}. The resistance R_{FJ} can be obtained using (5.69) by setting $c_{FJ} = c_{\alpha e}$ and the contact area is expressed as $A_{FJ} = \left(t_c + w_{we}\right)\left(l_{ch} + h_\alpha\right) / 8$.

The $0x$ nodes of 'E', 'G', 'I', 'J', and 'K' are connected to the $1x$ nodes of 'D', 'H', 'L', 'M', and 'N', through R_{DE}, R_{GH}, R_{IL}, R_{JM}, and R_{KN} respectively. These thermal resistances are calculated using (5.69) with the clearance is set to $c_{\alpha\beta}$ for all resistances. The contact areas between cuboids 'E' and 'D' and between 'G' and 'H' are set to $A_{DE} = A_{GH} = \left(h_\alpha + h_\beta\right) d_c / 8$. The contact area between 'I' and 'L' and between 'K' and 'N' is expressed as $A_{IL} = A_{KN} = \pi\left(r_{\alpha o} + r_{\beta i}\right)\left(h_\alpha + h_\beta\right) / 16$. The contact area for cuboids 'J' and 'M' is expressed as $A_{JM} = w_{we}\left(h_\alpha + h_\beta\right) / 4$.

Some nodes of the cuboidal elements are in contact with the ambient as shown in Fig. 5.6. This contact is represented by a temperature source T_a with a value equal to the

ambient temperature in series with a thermal resistance R_{ja} with a value depends on the contact area A_{ja} and the heat transfer coefficient h_{ja} between cuboid j and ambient. Thus,

$$R_{ja} = \frac{1}{A_{ja} h_{ja}} \tag{5.70}$$

By applying (5.70) to the TEC in Fig. 5.6, the thermal resistances to ambient shown in Table 5.1 are obtained.

Table. 5.1 Thermal Resistances to Ambient.

Elements A-C:

$$R_{A0za} = \frac{1}{h_{ca}\left(0.5(c_{\beta\beta} + c_{\alpha\beta}) + w_\beta\right) t_c} \qquad R_{Alya} = \frac{2}{h_{ca}\left(0.5(c_{\beta\beta} + c_{\alpha\beta}) + w_\beta\right) d_c}$$

$$R_{B0za} = \frac{1}{h_{ca}\left(0.5c_{\alpha\beta} + c_{\alpha c} + w_\alpha - r_{ci}\right) t_c} \qquad R_{Blya} = \frac{2}{h_{ca}\left(0.5c_{\alpha\beta} + c_{\alpha c} + w_\alpha - r_{ci}\right) d_c}$$

$$R_{C0ya} = \frac{8}{h_{ca}\pi\left(r_{co} + r_{ci}\right) d_c} \qquad R_{Clya} = \frac{8}{h_{ca}\pi\left(r_{co} + r_{ci}\right) d_c} \qquad R_{C0za} = \frac{4}{h_{ca}\pi\left(r_{co} + r_{ci}\right) t_c}$$

Elements D-H:

$$R_{Glya} = \frac{2}{h_{ca} w_\alpha d_c} \qquad R_{Hlya} = \frac{2}{h_{ca} w_\beta d_c} \qquad R_{Hlxa} = \frac{4}{h_{ca} h_\beta d_c}$$

Elements I-K:

$$R_{Ilya} = \frac{4}{h_{ca}\pi(r_{\alpha o} + r_{\alpha i}) w_\alpha} \qquad R_{Jlya} = \frac{1}{h_{ca} w_{we} w_\alpha} \qquad R_{Klya} = \frac{4}{h_{ca}\pi(r_{\alpha o} + r_{\alpha i}) w_\alpha}$$

Elements L-N:

$$R_{Llya} = \frac{4}{h_{ca}\pi(r_{\beta o} + r_{\beta i}) w_\beta} \qquad R_{Mlya} = \frac{1}{h_{ca} w_{we} w_\beta} \qquad R_{Nlya} = \frac{4}{h_{ca}\pi(r_{\beta o} + r_{\beta i}) w_\beta}$$

$$R_{L0xa} = \frac{4}{h_{ca}\pi r_{\beta o} h_\beta} \qquad R_{M0xa} = \frac{2}{h_{ca} w_{we} h_\beta} \qquad R_{N0xa} = \frac{4}{h_{ca}\pi r_{\beta o} h_\beta}$$

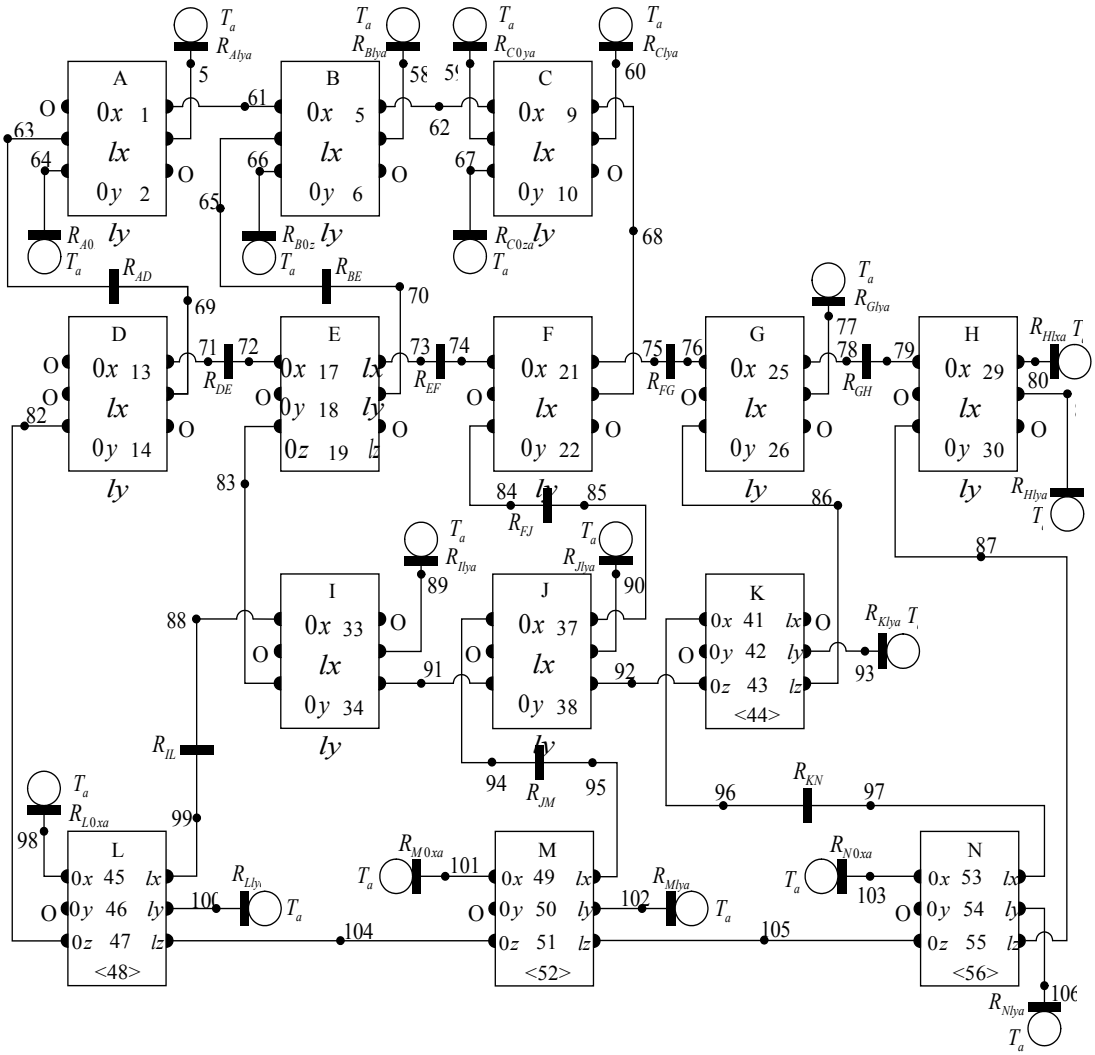

Fig. 5.6 Transformer Thermal Equivalent Circuit

6. PERFORMANCE EVALUATION

In the previous chapters, a transformer MEC and T-equivalent circuit model were developed and the leakage inductances were validated using a finite element-based model. In addition, expressions of the transformer high frequency losses were derived. In order to predict the temperature within the transformer windings and core, a transformer TEC model was established. In this chapter, the transformer design is considered in which the T-equivalent, MEC, and thermal models are used together to establish the transformer performance including voltage regulation and magnetizing and inrush currents. The transformer thermal analysis is conducted using the TEC.

6.1. Transformer Mass and Volume

The calculation of transformer dimensions is first considered starting with winding geometry. In the design process, the conductor area is determined. The calculated conductor area may not exactly match the conductor area from a standard wire gauge (SWG) list. Therefore, the round operator is used to select the closest conductor area from the SWG list as

$$a_{jc} = round_{SWG}\left(\frac{a_{jt}^{*}}{N_{jpr}}\right) \tag{6.1}$$

In (6.1), a_{jt}^{*} is the total area required for the parallel conductors of a single coil turn. From the conductor area one can obtain the radius of a cylindrical conductor using

$$r_{jc} = \sqrt{\frac{a_{jc}}{\pi}} \tag{6.2}$$

The winding bending constant is defined as

$$k_{jbd} = \frac{r_{ji}}{r_{jc}} \tag{6.3}$$

The bending constant is used in the design process to help ensure the feasibility of forming the radius of the end winding curvature.

The constant k_{jb} is defined as the winding build factor. From Chapter 2, the width and height of a unit cell of a coil is calculated as

$$w_{ju} = 2r_{jc}k_{jb} \tag{6.4}$$

$$h_{ju} = 2r_{jc}N_{jpr}k_{jb} \tag{6.5}$$

$$w_j = w_{ju}N_{jtuw} \tag{6.6}$$

$$h_j = h_{ju}N_{juh} \tag{6.7}$$

The coil area is obtained as

$$A_{jcl} = w_j h_j \tag{6.8}$$

and the packing factor is defined as

$$k_{jpf} = \frac{a_{jc}N_{jpr}N_{jcl}}{A_{jcl}} \tag{6.9}$$

The volume of a coil is calculated

$$U_{jcl} = h_j\left(\pi\left(r_{jo}^2 - r_{ji}^2\right) + 2w_j\left(d_w + w_{we}\right)\right) \tag{6.10}$$

where the dimensions in (6.10) are shown in Fig. 2.1 and Fig. 2.2.

Finally, the winding mass is computed

$$M_j = N_{jcp}N_{jcs}U_{jcl}k_{jpf}\rho_{jc} \tag{6.11}$$

where ρ_{jc} is the conductor mass density.

To determine the core and clearance dimensions, the width and height of the core interior window are first calculated as

$$w_{ci} = 2w_\alpha + 2w_\beta + 2c_{\alpha c} + 2c_{\alpha\beta} + c_{\beta\beta} \tag{6.12}$$

$$h_{ci} = \max\left(h_\alpha + 2c_{\alpha v}^*, h_\beta + 2c_{\beta v}^*\right) \tag{6.13}$$

the vertical clearance between the α-winding and the core and between the β-winding and the core is obtained

$$c_{\alpha v} = \frac{1}{2}\left(h_{ci} - h_{\alpha}\right) \tag{6.14}$$

$$c_{\beta v} = \frac{1}{2}\left(h_{ci} - h_{\beta}\right) \tag{6.15}$$

After computing the core interior width and height, the core exterior width and height are determined

$$w_{co} = w_{ci} + 2t_c \tag{6.16}$$

$$h_{co} = h_{ci} + 2t_c \tag{6.17}$$

The core volume is calculated as

$$U_c = d_c\left(\pi\left(r_{co}^2 - r_{ci}^2\right) + 2t_c\left(l_{cv} + l_{ch}\right)\right) \tag{6.18}$$

The core mass is determined using

$$M_c = U_c\rho_c \tag{6.19}$$

where ρ_c is the core mass density.

In some cases, there is a limit on the transformer total volume. Thus, it is useful to compute the total depth, width, and height of the transformer as

$$d_T = d_w + 2r_{\beta o} \tag{6.20}$$

$$w_T = w_{co} + 2\left(c_{\alpha c} + w_{\alpha} + c_{\alpha\beta} + w_{\beta}\right) \tag{6.21}$$

$$h_T = h_{co} \tag{6.22}$$

It is also useful to calculate the total mass as

$$M_T = M_c + M_{\alpha} + M_{\beta} \tag{6.23}$$

6.2. Transformer Performance

The transformer performance can be predicted using the T-equivalent circuit shown in Fig. 2.6, in conjunction with the MEC model which was set forth in Chapter 3. The transformer TEC is then used to perform a transformer thermal analysis and to update the transformer resistances. Prior to describing how this is done, it is convenient to first consider winding resistance.

6.2.1. T-equivalent Circuit Parameters

The resistance of the j-winding is expressed as

$$r_j = \frac{N_{jcs}}{N_{jcp}} r_{jcl} \tag{6.24}$$

where r_{jcl} is the resistance of the j-winding coil which is calculated using (4.58). It should be noted that for the α-winding, the referred resistance is obtained from the actual value using (2.12). A method to obtain the core resistance will be discussed when the operating point analysis is considered.

Also it is useful to include the dynamic resistances obtained in Section 4.3 in the T-equivalent circuit model. To do so, the sum of the dynamic resistances of the coil segments is expressed as

$$r_D = \begin{vmatrix} r_{D_{\alpha\alpha}} & r_{D_{\alpha\beta}} \\ r_{D_{\alpha\beta}} & r_{D_{\beta\beta}} \end{vmatrix} \tag{6.25}$$

Substituting (6.25) into (4.51) yields

$$\bar{S}_{pe} = \left\langle r_{D_{\alpha\alpha}} \overline{\left(\frac{di_\alpha}{dt}\right)^2} + 2 r_{D_{\alpha\beta}} \overline{\left(\frac{di_\alpha}{dt}\frac{di_\beta}{dt}\right)} + r_{D_{\beta\beta}} \overline{\left(\frac{di_\beta}{dt}\right)^2} \right\rangle \tag{4.26}$$

Using the T-equivalent circuit, the derivative of magnetizing current squared can be related to the winding currents as

$$\left(\frac{di_m}{dt}\right)^2 = \left(\frac{di'_\alpha}{dt}\right)^2 + 2\left(\frac{di'_\alpha}{dt}\right)\left(\frac{di_\beta}{dt}\right) + \left(\frac{di_\beta}{dt}\right)^2 \tag{6.27}$$

From (2.6), (4.26), and (4.27), one can yield

$$\bar{S}_{pe} = \left\langle r'_{D_\alpha} \overline{\left(\frac{di'_\alpha}{dt}\right)^2} + r_{D_m} \overline{\left(\frac{di_m}{dt}\right)^2} + r_{D_\beta} \overline{\left(\frac{di_\beta}{dt}\right)^2} \right\rangle \tag{6.28}$$

where

$$r_{D_m} = \left(\frac{N_\beta}{N_\alpha}\right) r_{D_{\alpha\beta}} \tag{6.29}$$

$$r_{D_\alpha}^{'} = \left(\frac{N_\beta}{N_\alpha}\right)^2 r_{D_{\alpha\alpha}} - r_{D_m} \tag{6.30}$$

$$r_{D_\beta} = r_{D_{\beta\beta}} - r_{D_m} \tag{6.31}$$

Assuming sinusoidal currents, the result in (6.28) can be represented using the T-equivalent circuit by adding a resistance $\omega_e^2 r_{D_\alpha}^{'}$ in series with the α-winding impedance, a resistance $\omega_e^2 r_{D_\beta}$ in series with the β-winding impedance, and a resistance $\omega_e^2 r_{D_m}$ in series with the magnetizing branch impedance as depicted in Fig. 6.1.

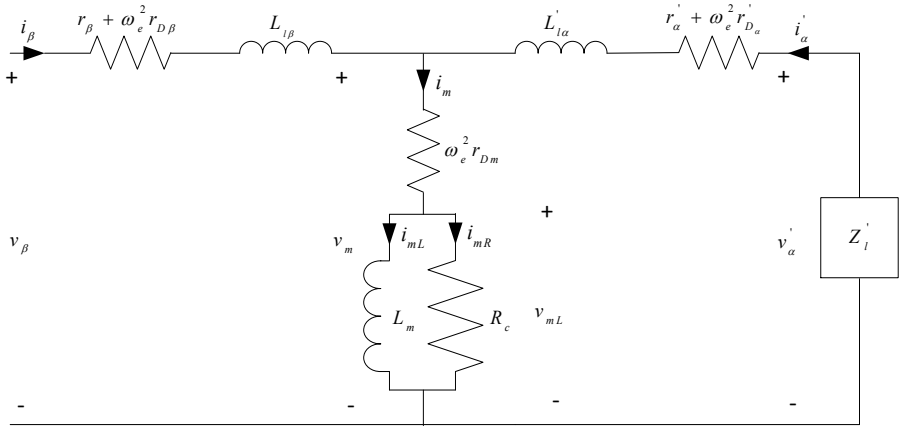

Fig. 6.1 High Frequency T-Equivalent Circuit Model

6.2.2. Voltage Regulation

The winding resistances and leakage inductances are sources of a voltage drop such that load voltage is dependent on the load current. The variation of the load voltage is typically limited since many loads are sensitive to voltage variation. Therefore, to set limits within the design, it is useful to define voltage regulation as

$$\chi = \left| \frac{V_{\alpha,fl} - V_{\alpha,nl}}{V_{\alpha,nl}} \right| \tag{6.32}$$

In (6.32) $\tilde{V}$ and $\tilde{V}$ are the phasor representations of the full-load and no-load load voltages, respectively. Using the T-equivalent circuit model illustrated in Fig. 6.1, the no-load and the full-load voltages can be calculated as

$$V_{\alpha,nl} = \frac{Z_m}{r_\beta + \omega_e^2 r_{D_\alpha}^{'} + Z_m + j\omega_e L_{l\beta}} \frac{N_\alpha}{N_\beta} V_\beta \tag{6.33}$$

$$V_{\alpha,fl} = \frac{Z_m}{r_\beta + \omega_e^2 r_{D_\beta} + Z_m + j\omega_e L_{l\beta}} \frac{N_\alpha}{N_\beta} V_\beta - \left(r_\alpha^{'} + \omega_e^2 r_{D_\alpha}^{'} + j\omega_e L_{l\alpha}^{'} + \frac{Z_m \left(r_\beta + \omega_e^2 r_{D_\beta} + j\omega_e L_{l\beta} \right)}{r_\beta + \omega_e^2 r_{D_\beta} + Z_m + j\omega_e L_{l\beta}} \right) \left(\frac{N_\alpha}{N_\beta} \right)^2 I_{\alpha,fl}^{'} \tag{6.34}$$

where

$$Z_m = \omega_e^2 r_{D_m} + \frac{j\omega_e L_m R_c}{R_c + j\omega_e L_m} \tag{6.35}$$

Substituting (6.33) and (6.34) into (6.32) and simplifying yields

$$\chi = \left| \left(r_\alpha^{'} + \omega_e^2 r_{D_\alpha}^{'} + j\omega_e L_{l\alpha}^{'} \right) \left(1 + \frac{r_\beta + \omega_e^2 r_{D_\beta} + j\omega_e L_{l\beta}}{Z_m} \right) + r_\beta + \omega_e^2 r_{D_\beta} + j\omega_e L_{l\beta} \right| \frac{I_{\alpha,fl}^{'}}{V_\beta} \tag{6.36}$$

6.2.3. Operating Point Analysis

The high frequency T-equivalent circuit in tandem with the MEC form the basis for the operating point analysis using the procedure set forth in [13]. It is assumed that the analysis is performed under normal loading conditions which means that the load current varies between no-load and full-load. The leakage inductances are assumed to be constant; however, the magnetizing inductance and core loss resistance are a function of load current. It is also assumed that the input voltage $\tilde{V}_{,}$ and the referred load impedance $Z_l^{'}$ are constant. A numerical method is used to compute the steady-state operating point. This method utilizes the T-equivalent circuit along with the magnetic equivalent circuit and the TEC model. A Pseudo-code illustrating the operating point analysis is shown in Table 6.1. A discussion at each step will follow.

Table 6.1 Operating Point Analysis Pseudo-Code

1. express magnetizing current as a function of magnetizing flux linkage (6.38)
2. initialization

   $k = 1$ and $T_{\Omega}^{1} = T_{A}^{1}$ (ambient temperature)

   initialize core resistance (6.39) and magnetizing inductance (6.40)

   initialize magnetizing current component in core resistance (6.41)
3. solving the T-equivalent circuit

   evaluate the electrical resistivity of coil cuboids (6.42)

   evaluate the electrical resistances of cuboids (6.43)

   evaluate winding resistances (6.44) and dynamic resistances (6.29)-(6.31)

   evaluate impedances (6.45)-(6.49)

   calculate magnetizing voltage and referred α –winding voltage (6.50)-(6.51)

   calculate referred α –winding current (6.52)
4. magnetizing current

   evaluate magnetizing flux linkage (6.54)

   calculate magnetizing current (6.55)- (6.56)
5. update magnetizing branch parameters

   calculate β –winding current (6.57)

   use the MEC and the MSE to compute core loss, S_{cl}^{k}

   update core resistance (6.58)

   update magnetizing inductance (6.60)- (6.63)
6. update the cuboid temperatures

   calculate power lost in each winding cuboid (6.65)

   use the TEC model to update the cuboid temperatures
7. check convergence

   calculate e_m, the magnetizing branch parameters error (6.66)

   calculate e_T, the temperature error (6.67)

Table 6.1 (Continued)

if $e_T > e_{Tmxa}$ or $e_m > e_{mmxa}$

$k = k + 1$

return to Step 3

end

8. final calculations

evaluate voltage regulation (6.36) and winding power loss (4.114)

calculate transformer total power loss (6.68)

end

The steps of this method are as follows:

Step 1 – Magnetizing Current as a Function of Magnetizing Flux Linkage

In order to perform the operating point analysis it is useful to express the magnetizing current as a function of the magnetizing flux linkage. To obtain this function using the MEC, the β –winding current is set to zero and test currents between zero and a multiple of the expected value of the magnetizing current are applied to the α – winding. The magnetizing flux linkage corresponding to a test current i_m is calculated as

$$\lambda_m = \lambda_\beta \big|_{i_\beta = 0, i_\alpha = N_\beta i_m / N_\alpha} \tag{6.37}$$

From this data, a magnetizing current function is generated. This function may be represented as

$$i_{mL} = F_{im}\left(\lambda_m\right) \tag{6.38}$$

Step 2 – Initialization

Since transformer electrical and thermal parameters are interrelated, it is required to conduct an electro-thermal analysis. The effect of the temperature on the core loss is neglected and thus the value of the power source of elements ‘A’, ‘B’, ‘C’, and ‘F’ in the thermal model shown in Fig. 5.4 is only a function of the core parameters at a nominal

temperature. Due to the coupling between the electrical and thermal models, an iterative approach is used to conduct this analysis. The process is initialized with the iteration index $k=1$. The initial temperature is assumed to be equal to the ambient temperature.

The initial estimate of the magnetizing inductance and the core resistance are:

$$R_c^1 = \infty \tag{6.39}$$

$$L_m^1 = L_{m0} \tag{6.40}$$

Also from (6.39) the component of the magnetizing current that flows in the core resistance is initialized to

$$i_{mR}^1 = 0 \tag{6.41}$$

Step 3 – Solving the T-equivalent

The resistivity (the reciprocal of the conductivity) of each of the coil cuboidal elements depends on temperature. The relationship between the resistivity and the temperature of element Ω is approximated as

$$\rho_\Omega^k = k_T \left(\frac{T_\Omega^k}{T_0} \right)^{n_T} + b_T \tag{6.42}$$

where T_Ω^k is the mean temperature of element at iteration k, T_0 is the temperature at which the nominal value of the resistivity is measured, and k_T, n_T, and b_T are temperature coefficients of resistivity.

Using the result in (4.60), the partition of the coil resistance associated with element Ω is expressed as

$$r_\Omega^k = -\frac{N_{jcl}}{2N_{jpr}} \mathrm{Re}\left(\frac{U_\Omega \rho_\Omega^k J_B\left(r_{jc}/k\right)}{2\pi r_{jc} A_\Omega k J_B^{'}\left(r_{jc}/k\right)} \right) \tag{6.43}$$

where U_Ω, A_Ω, and r_{jc} are the volume, area, and the conductor radius of element Ω; where Ω may be the 'D', 'E', or 'G' through 'N' cuboids.

After obtaining the resistance of all conductor cuboidal elements, the j-winding resistance can be calculated as

$$r_j^k = \frac{4N_{jcs}}{N_{jcp}} \sum\nolimits_{\Omega \in j} r_\Omega^k \tag{6.44}$$

The resistivity obtained in (6.42) is also used to update the value of the dynamic resistance of the α- and β-coil segments derived in Section 4.3 after replacing the length of the coil segment with the length of the cuboid and then dividing the result by two. The division by two is due to the fact that the height of the cuboids associated with the transformer windings is equal to half of the corresponding coil segment height. Then the value of $r_{D_m}^k$, $r_{D_\alpha}^{'k}$, and $r_{D_\beta}^k$ are obtained using (6.29)-(6.31).

As expressed in (6.38), saturation is represented by expressing the magnetizing current as a function of the magnetizing flux linkage. To solve the T-equivalent circuit, it is helpful to define some equivalent impedances. The impedance at the magnetizing branch is defined as:

$$Z_m^k = \frac{j\omega_e L_m^k R_c^k}{R_c^k + j\omega_e L_m^k} + \omega_e^2 r_{D_m}^k \tag{6.45}$$

the α-winding branch impedance and referred β-winding branch impedance are defined as

$$Z_\beta^k = r_\beta^k + + \omega_e^2 r_{D_\beta}^k + j\omega_e L_{l\beta} \tag{6.46}$$

$$Z_\alpha^{'k} = r_\alpha^{'k} + + \omega_e^2 r_{D_\alpha}^{'k} + j\omega_e L_{l\alpha}^{'} \tag{6.47}$$

the series combination of $Z_\alpha^{'k}$ and $Z_l^{'k}$ is expressed

$$Z_{\alpha l}^{'k} = Z_\alpha^{'k} + Z_l^{'} \tag{6.48}$$

And finally, the parallel combination of $Z_m^{'k}$ and $Z_{\alpha l}^{'k}$ is expressed

$$Z_{m\alpha l}^k = \frac{Z_m^k Z_{\alpha l}^{'k}}{Z_m^k + Z_{\alpha l}^{'k}} \tag{6.49}$$

Using the impedances of (6.45)-(6.49), the magnetizing voltage and the referred voltage and current at the load side are calculated

$$V_m^k = \frac{Z_{m\alpha l}^k}{Z_{m\alpha l}^k + Z_\beta^k} V_\beta^k \tag{6.50}$$

$$V_{\alpha}^{'k} = \frac{Z_l^{'}}{Z_l^{'} + Z_{\alpha}^{'k}} V_m^k \tag{6.51}$$

$$I_{\alpha}^{'k} = \frac{V_{\alpha}^{'k}}{Z_l^{'}} \tag{6.52}$$

The voltage across the magnetizing inductance is calculated as

$$V_{mL}^k = \frac{Z_m^k - \omega_e^2 r_{D_m}^k}{Z_m^k} V_m^k \tag{6.53}$$

Step 4 – Magnetizing Current

Due to the non-linear magnetizing characteristic, the magnetizing current may not be sinusoidal. Therefore, one cannot utilize phasor analysis to obtain its value. In this step, the analysis is performed in the time domain, using the magnetizing voltage whose phasor value is obtained step 4. Specifically, it is assumed magnetizing voltage is sinusoidal and has a form

$$v_{mL}^k = \sqrt{2}\left|V_{mL}^k\right| \sin\left(\omega_e t + \phi_{vmL}^k\right) \tag{6.54}$$

where V_{mL}^k and ϕ_{vmL}^k are obtained using (6.54). One may object to the assumption that the magnetizing voltage is sinusoidal. However, in general the voltage drop across the leakage inductances and winding resistances is small. In addition, the magnetizing current compared to the load current is also small. Therefore, one can argue that the influence of the harmonics of the magnetizing current on the magnetizing voltage is negligible. Under this approximation, the magnetizing flux linkage obtained from the magnetizing voltage using Faraday's law is expressed:

$$\lambda_m^k = \frac{\sqrt{2}\left|V_{mL}^k\right|}{\omega_e} \cos\left(\omega_e t + \phi_{vmL}^k\right) \tag{6.55}$$

Using (6.38), the current through the magnetizing inductance is obtained

$$i_{mL}^k\left(t\right) = F_{im}\left(\lambda_m^k\left(t\right)\right) \tag{6.56}$$

The total magnetizing current is then calculated as

$$i_m^k\left(t\right) = i_{mL}^k\left(t\right) + i_{mR}^k\left(t\right) \tag{6.57}$$

Step 5 – Updating the Magnetizing Branch Parameters

In this step, the magnetizing inductance and the core resistance for the following iteration are calculated. First the β-winding current is calculated

$$i_{\beta}^{k}(t) = i_{m}^{k}(t) - i_{\alpha}^{'k}(t) \tag{6.58}$$

Now since both winding current are known, the flux density in the core tubes is obtained from the MEC. Then MSE is used to compute core loss of the core cuboids, S_{cl}^{k} [13].

Then, the core resistance is updated

$$R_{c}^{k+1} = \frac{\left(V_{mL}^{k}\right)^{2}}{S_{cl}^{k}} \tag{6.59}$$

The current in the core resistance for the next iteration is thus computed as

$$i_{mR}^{k+1} = \frac{v_{mL}^{k}}{R_{c}^{k+1}} \tag{6.60}$$

Next, the Fourier series is used to obtain the fundamental component of the current through the magnetizing inductance. To do so, Fourier series coefficient are expressed as

$$a_{mL1} = \frac{4}{T}\int_{0}^{T/2} i_{mL}^{k}(t)\cos(\omega_{e}t)\,dt \tag{6.61}$$

$$b_{mL1} = \frac{4}{T}\int_{0}^{T/2} i_{mL}^{k}(t)\sin(\omega_{e}t)\,dt \tag{6.62}$$

The rms value of the magnetizing current through the magnetizing inductance is computed as

$$\hat{I}_{mL}^{k} = \frac{1}{\sqrt{2}}\sqrt{\left(a_{mL1}^{2} + b_{mL1}^{2}\right)} \tag{6.63}$$

In (6.63), the notation '^' is used to indicate that only the fundamental component of the magnetizing current is considered. Subsequently, magnetizing inductance for the next iteration is updated as

$$L_{m}^{k+1} = \frac{V_{mL}^{k}}{\omega_{e}\hat{I}_{mL}^{k}} \tag{6.64}$$

Step 6 – Updating the Temperatures of each Cuboid

To update the cuboid temperatures, the power loss of each cuboid is calculated at the next iteration using

$$S_{\Omega}^{k+1} = r_{\Omega}^{k} i_{jcl}^{k2} + \omega_e^2 i^T r_{D_\Omega}^{k+1} i \tag{6.65}$$

In (6.65), r_{D_Ω} denotes the dynamic resistance of element Ω at iteration $k+1$ which is calculated using the expressions derived in Section 4.3 and the electrical resistivity in (6.42). The core loss of each core cuboid, $S_{\Omega cl}^{k}$, is evaluated by multiplying the core loss obtained in Step 7 by the volume of the cuboid and dividing the result by the volume of the core.

After evaluating the power loss of each cuboid, the temperature at iteration $q+1$ which is denoted T_{Ω}^{q+1} is obtained using the TEC.

Step 7 – Checking Convergence

The error metrics associated with the magnetizing branch are defined

$$e_m = \max\left(\left| \frac{R_c^{k+1} - R_c^{k}}{R_c^{k+1}} \right|, \left| \frac{L_m^{k+1} - L_m^{k}}{L_m^{k+1}} \right| \right) \tag{6.66}$$

The error associated with the cuboid temperature is defined as

$$e_T = \max\left(\left| \mathbf{T}_{\Omega}^{q+1} - \mathbf{T}_{\Omega}^{q} \right| \right) \tag{6.67}$$

Finally, if $e_T < e_{T\max}$ or $e_m < e_{\mathrm{m}\max}$, where $e_{T\max}$ and $e_{\mathrm{m}\max}$ are the corresponding maximum allowed errors, then the algorithm converges and the performance evaluation process proceeds to the final step ; otherwise, the iterative process is repeated starting at Step 3.

Step 8 – Final Calculations

Once convergence is established, the transformer voltage regulation and the winding power loss are evaluated using (6.36) and (4.105) respectively. The total power loss is then calculated as

$$S_l = S_{rl} + S_{cl} \tag{6.68}$$

6.2.4. Inrush Current

In addition to steady-state behavior, some aspects of transient performance are crucial and must be considered in the transformer design. One key metric is transformer inrush current which occurs when a transformer is connected to a voltage source.

To determine inrush current, it is assumed that at time $t = t_c$ a sinusoidal voltage source v_β is applied to the β-winding side. If the winding resistances are neglected then the β-winding flux linkage can be calculated as

$$\lambda_\beta(t) = \int_{t_c}^{t} v_\beta(t)dt \tag{6.69}$$

If $v_\beta = \sqrt{2}V_\beta \cos\left(\omega_e t + \phi_{v\beta}\right)$, solving the integral of (6.69) yields

$$\lambda_\beta(t) = \frac{\sqrt{2}V_\beta}{\omega_e}\left(\sin\left(\omega_e t + \phi_{v\beta}\right) - \sin\left(\omega_e t_c + \phi_{v\beta}\right)\right) \tag{6.70}$$

The maximum possible value of the magnetizing flux linkage occurs when the second term in (6.70) is equal to -1. This happens when

$$\omega_e t_c + \phi_{v\beta} = -\frac{\pi}{2} \tag{6.71}$$

As a result, the worst case scenario of the peak magnetizing flux density will be twice its nominal value, i.e.

$$\lambda_{\beta,wcs} = \frac{2\sqrt{2}V_\beta}{\omega_e} \tag{6.72}$$

7. NOMINAL DESIGN APPROACH

A transformer detailed model was derived in previous chapters. Now the stage is set to set forth the transformer design process. In this section, the design space, constraints, and fitness function are defined in a manner similar to [13]. Then, a multi-objective optimization between mass and power loss is performed using GOSET which a Matlab based toolbox [71]. In this algorithm the number of generation was selected to be 1000 with a population size of 1000. The result of this optimization process is a set of non-dominated designs referred to as the Pareto-optimal front. Finally, a design from the Pareto-optimal front is presented.

7.1. Transformer Analysis Organization

One may notice that the transformer involves a large number of parameters and two coupled models that form the basis of analysis. It is useful to organize these parameters into categories. The variables that are related to the transformer configuration are organized into four vectors: vector '$\mathbf{C}$' which contains the core variables, '$\mathbf{G}$' which contains gap (or clearance) values, and the last two, $\mathbf{W}_\alpha$ and $\mathbf{W}_\beta$ which are related to the α-winding and the β-winding respectively. It is useful to divide each vector into two sets, one that corresponds to the independent variables denoted by the subscript 'I' and one that corresponds to the dependent variables denoted by the subscript 'D'. The sets which are related to the independent variables are defined as

$$\mathbf{C}_I = \left[m_c \;\; r_{ci} \;\; t_c \;\; d_c \right]^T \tag{7.1}$$

$$\mathbf{G}_I = \left[c_{\alpha\beta} \;\; c_{\beta\beta} \;\; c^*_{\alpha v} \;\; c^*_{\beta v} \right]^T \tag{7.2}$$

$$\mathbf{W}_{\alpha I} = \left[m_\alpha \;\; \mathrm{a}^*_{\alpha t} \;\; k_{\alpha b} \;\; \mathrm{N}_{\alpha pr} \;\; N_{\alpha uh} \;\; N_{\alpha uw} \;\; N_{\alpha cl} \;\; N_{\alpha cs} \;\; N_{\alpha cp} \right]^T \tag{7.3}$$

$$\mathbf{W}_{\beta I} = \left[m_\beta \;\; \mathrm{a}^*_{\beta t} \;\; k_{\beta b} \;\; \mathrm{N}_{\beta pr} \;\; N_{\beta uh} \;\; N_{\beta uw} \;\; N_{\beta cl} \;\; N_{\beta cs} \;\; N_{\beta cp} \right]^T \tag{7.4}$$

where m_c, m_α, and m_β are indices which correspond to the material type of the core, α-winding, and the β-winding, respectively. Also the dependent variable sets are defined as

$$\mathbf{C}_D = \left[\mathbf{P}_c^T \;\; h_{ci} \;\; w_{ci} \;\; h_{co} \;\; w_{co} \;\; r_{co} \;\; A_{cv} \;\; l_{cv} \;\; A_{ch} \;\; l_{ch} \;\; U_c \;\; M_c \right]^T \tag{7.5}$$

$$\mathbf{G}_D = \left[c_{\alpha c} \;\; c_{bc\_mn} \;\; c_{\alpha v} \;\; c_{\beta v} \right]^T \tag{7.6}$$

$$\mathbf{W}_{\alpha D} = \left[\mathbf{P}_\alpha^T \;\; a_{\alpha c} \;\; r_{\alpha c} \;\; k_{\alpha bd} \;\; w_{\alpha u} \;\; h_{\alpha u} \;\; w_\alpha \;\; h_\alpha \;\; A_{\alpha cl} \;\; k_{\alpha pf} \;\; U_{\alpha cl} \;\; M_\alpha \right]^T \tag{7.7}$$

$$\mathbf{W}_{\beta D} = \left[\mathbf{P}_\beta^T \;\; a_{\beta c} \;\; r_{\beta c} \;\; k_{\beta bd} \;\; w_{\beta u} \;\; h_{\beta u} \;\; w_\beta \;\; h_\beta \;\; A_{\beta cl} \;\; k_{\beta pf} \;\; U_{\beta cl} \;\; M_\beta \right]^T \tag{7.8}$$

where c_{bc_mn} is the minimum clearance between the α-winding bending curvature and the core and $\mathbf{P}_c$, $\mathbf{P}_\alpha$, and $\mathbf{P}_\beta$ are vectors that carry a material related information on the core, α-winding, and the β-winding, respectively. Expanded, they are expressed

$$\mathbf{P}_c = \left[\rho_c \;\; \mu_r \;\; \alpha_\mu \;\; \beta_\mu \;\; \gamma_\mu \;\; k_h \;\; \alpha_h \;\; \beta_h \;\; k_e \right]^T \tag{7.9}$$

$$\mathbf{P}_\alpha = \left[\rho_{\alpha c} \;\; \sigma_{\alpha c} \;\; J_{\alpha,mxa} \right]^T \tag{7.10}$$

$$\mathbf{P}_\beta = \left[\rho_{\beta c} \;\; \sigma_{\beta c} \;\; J_{\beta,mxa} \right]^T \tag{7.11}$$

In (7.9), ρ_c is the core material mass density, α_μ, β_μ, and γ_μ are the anhysteretic curve parameters, and k_h, α_h, α_h, and k_e are parameters associated with the MSE loss model. In (7.10) and (7.11), $\rho_{\alpha c}$ and $\rho_{\beta c}$ are the mass density for the α-winding, and the β-winding, $\sigma_{\alpha c}$ and $\sigma_{\beta c}$ are the conductivities of the winding conductors, and $J_{\alpha,mxa}$ and $J_{\beta,mxa}$ are the maximum allowed current density for the corresponding winding. Within the design program, the independent set parameters are used to calculate the parameters of the dependent set. They are then merged into the corresponding vectors

$$\mathbf{C} = \left[\mathbf{C}_I^T \;\; \mathbf{C}_D^T \right]^T \tag{7.12}$$

$$\mathbf{G} = \left[\mathbf{G}_I^T \;\; \mathbf{G}_D^T \right]^T \tag{7.13}$$

$$\mathbf{W}_{\alpha} = \left[\mathbf{W}_{\alpha I}^{T} \; \mathbf{W}_{\alpha D}^{T} \right]^{T} \tag{7.14}$$

$$\mathbf{W}_{\beta} = \left[\mathbf{W}_{\beta I}^{T} \; \mathbf{W}_{\beta D}^{T} \right]^{T} \tag{7.15}$$

Within the design program, it is convenient to merge all vectors and parameters that are related to the transformer description into a single structure as follows

$$\mathbf{T} = \left[\mathbf{C}^{T} \; \mathbf{G}^{T} \; \mathbf{W}_{\alpha}^{T} \; \mathbf{W}_{\beta D}^{T} \; d_{T} \; w_{T} \; h_{T} \; M_{T} \right]^{T} \tag{7.16}$$

Similar to the sets that are related to the transformer geometry and material selection, it is useful to define the vector of the electrical parameters as

$$\mathbf{E} = \left[N_{\beta} \; N_{\alpha} \; r_{\beta} \; r_{D_{\beta}} \; r_{\alpha}^{'} \; r_{D_{\alpha}}^{'} \; L_{l\beta} \; L_{\alpha}^{'} \; L_{m0} \; \chi \right]^{T} \tag{7.17}$$

A vector which contains the operating point analysis denoted $\mathbf{O}$ is divided into input set $\mathbf{0}_{I}$ and output set $\mathbf{O}_{O}$ and they are defined as

$$\mathbf{O}_{I} = \left[V_{\beta} \; Z_{L} \; \omega_{e} \right]^{T} \tag{7.18}$$

$$\mathbf{O}_{O} = \left[I_{\beta} \; V_{\alpha} \; P_{rl} \; P_{cl} \; P_{l} \; L_{m} \; R_{c} \; B_{ch}(t) \; B_{cv}(t) \; B_{co,1}(t) \; B_{co,2}(t) \; B_{co,3}(t) \; i_{m}(t) \; T_{mx} \right]^{T} \tag{7.19}$$

An operating point vector which contain both sets is then expressed

$$\mathbf{O} = \left[\mathbf{O}_{I}^{T} \; \mathbf{O}_{O}^{T} \right]^{T} \tag{7.20}$$

Some of the variables that are related to the transformer dimensions are fixed. For example the clearances between the windings and between windings and core are fixed since they depend on the maximum allowed voltage stress which is typically specified. Also, the number of coils connected in series and parallel are held constant in this research. The build factor of each winding can also be approximated to be a constant value. Therefore, a design vector which contain these fixed parameters is defined as

$$\mathbf{D}_{fp} = \left[c_{\alpha c\_mn} \; c_{\alpha\beta} \; c_{\beta\beta} \; c_{\alpha v}^{*} \; c_{\beta v}^{*} \; k_{\alpha b} \; N_{\alpha cs} \; N_{\alpha cp} \; k_{\beta b} \; N_{\beta cs} \; N_{\beta cp} \right]^{T} \tag{7.21}$$

where $c_{\alpha c\_mn}$ is the minimum clearance between α–winding and core. When the fitness function is defined this vector is considered as part of the design specification.

7.2. Design Space

As part of the design process, a design input vector is specified using some of the independent variables identified in the previous section. It is defined as

$$\boldsymbol{\theta} = \left[m_c \;\; d_w \;\; c_{\alpha c} \;\; h_{bce} \;\; w_{bce} \;\; w_{es} \;\; r_{ci} \;\; m_\beta \;\; a^*_{\beta t} \;\; N^*_{\beta pr} \;\; N^*_{\beta cl} \;\; R^*_{\beta hw} \;\; m_\alpha \;\; a^*_{\alpha t} \;\; N^*_{\alpha pr} \;\; R^*_{N\beta\alpha} \;\; R^*_{\alpha hw} \right]^T \tag{7.22}$$

One may question why many of the independent variables highlighted in the previous section are not used in the design vector. It is often the case that the independent variables are fixed by design specifications. For example, the clearance between the alpha and beta windings may be set by the manufacturer. Similarly, the beta winding voltage, frequency, and load impedance are often specified. In (7.22), the parameters denoted by the '*' notation are desired values. Exact desired values may not be achievable in practice. For example, $a^*_{\alpha t}$ may not correspond to a standard wire gauge. In these cases corresponding actual values are defined to be those that are closest to the desired values. The actual values are then used within the performance evaluation of a design.

From the design and fixed parameter vectors, most of the independent variables of the vector $\mathbf{T}$ are identified. However, some of the independent variables associated with $\mathbf{C}_I$, $\mathbf{G}_I$, $\mathbf{W}_{\alpha I}$, and $\mathbf{W}_{\beta I}$ must be defined using additional operators. These include

$$N_{\beta pr} = \text{round}\left(N^*_{\beta pr} \right) \tag{7.23}$$

$$N_{\beta cl} = \text{round}\left(N^*_{\beta pl} \right) \tag{7.24}$$

$$N_{\beta uh} = \text{ceil}\left(\sqrt{\frac{N_{\beta cl} R^*_{\beta hw}}{N_{\beta pr}}} \right) \tag{7.25}$$

$$N_{\beta uw} = \text{ceil}\left(\frac{N_{\beta cl}}{N_{\beta uh}} \right) \tag{7.26}$$

$$N_{\alpha pr} = \text{round}\left(N^*_{\alpha pr} \right) \tag{7.27}$$

$$N_{\alpha cl} = \max\left(1, \text{round}\left(\frac{N_{\beta cl} N_{\beta cs}}{R^*_{N\beta\alpha} N_{\alpha cs}} \right) \right) \tag{7.28}$$

$$N_{\alpha uh} = \text{ceil}\left(\sqrt{\frac{N_{\alpha cl} R^*_{\alpha hw}}{N_{\alpha pr}}} \right) \tag{7.29}$$

$$N_{\alpha uw} = \text{ceil}\left(\frac{N_{\alpha cl}}{N_{\alpha uh}} \right) \tag{7.30}$$

where ceil is an operator that rounds the input to the upper most integer, and round is an operator that rounds the input to the closest integer.

7.3. Design constraints and fitness functions

To ensure that the obtained designs from the optimization process are all feasible, design constraints are imposed. Before considering the design constraints, it is convenient to define the less-than and the greater-than function as

$$\text{lte}\left(x, x_{mx}\right) = \begin{cases} 1 & x \le x_{mx} \\ \dfrac{1}{1 + x - x_{mx}} & x > x_{mx} \end{cases} \tag{7.31}$$

$$g\text{te}\left(x, x_{mn}\right) = \begin{cases} 1 & x \ge x_{mn} \\ \dfrac{1}{1 + x_{mn} - x} & x < x_{mn} \end{cases} \tag{7.32}$$

The less-than function is used when the constraint is on an upper limit x_{mx} while the greater-than function is used to impose the constraint on a lower limit x_{mn}.

The first constraint is imposed on the minimum clearance between and core

$$c_1 = g\text{te}\left(c_{\alpha c\_mn}, c_{mnr}\right) \tag{7.33}$$

where c_{mnr} is the minimum required clearance.

Typically, it is desired to limit the total dimensions of the transformer which yields the constraints

$$c_2 = \text{lte}\left(d_T, d_{Tmxa}\right) \tag{7.34}$$

$$c_3 = \text{lte}\left(w_T, w_{Tmxa}\right) \tag{7.35}$$

$$c_4 = \text{lte}\left(h_T, h_{Tmxa}\right) \tag{7.36}$$

Also, another constraint regarding dimensions is imposed on the design of the transformer. First the aspect ratio of the transformer is defined as

$$\eta_T = \frac{\max\left(d_T, w_T, h_T\right)}{\min\left(d_T, w_T, h_T\right)} \tag{7.37}$$

Subsequently, the constraint on the aspect ratio is imposed

$$c_5 = \mathrm{lte}\left(\eta_T, \eta_{Tmxa}\right) \tag{7.38}$$

To keep the total mass of the transformer within a practical range and to reduce the search space, the maximum allowed mass is constrained. This yields the constraint

$$c_6 = \mathrm{lte}\left(M_T, M_{Tmxa}\right) \tag{7.39}$$

Since the β-winding coils are wound around the α-winding coils, it is recommended practice that the height of the β-winding coils is less than the height of the α-winding coils. Thus

$$c_7 = \mathrm{lte}\left(h_\beta, h_\alpha\right) \tag{7.40}$$

The bending radius of a conductor depends on the conductor radius. Therefore, constraints on the bending factor are considered

$$c_8 = \mathrm{gte}\left(k_{\beta bd}, k_{bdmnr}\right) \tag{7.41}$$

$$c_9 = \mathrm{gte}\left(k_{\alpha bd}, k_{bdmnr}\right) \tag{7.42}$$

where k_{bdmnr} is the minimum required bending radius factor.

The evaluation of some constraints can only be performed if the MEC converges. Therefore, a constraint c_{10} is used to check MEC convergence. If the MEC solver does not converge, the design is considered infeasible. If the MEC converges, the constraint on the voltage regulation is evaluated using

$$c_{11} = \mathrm{lte}\left(\chi, \chi_{mxa}\right) \tag{7.43}$$

The inrush current is limited implicitly by imposing a constraint on the magnetizing flux linkage. To evaluate, within the MEC the β-winding current is set to be the maximum allowed inrush current while the α-winding current is set to zero. Since the MEC is used in this test, a constraint c_{12} is imposed to check the MEC convergence. Provided the convergence of MEC, the calculated β-winding flux linkage $\lambda_{\beta i}$ is

compared to the magnetizing flux linkage defined as the worst case scenario in (4.61). If the calculated flux linkage is greater than the worst case scenario flux linkage then the worst case scenario magnetizing current will be less than maximum allowed inrush current. This is archived by imposing the constraint on the β -winding flux linkage as

$$c_{13} = \mathrm{lte}\left(\lambda_{\beta i}, \lambda_{\beta wci}\right) \tag{7.44}$$

The operating point analysis described in Chapter 4 must be performed for each member of the population. The first step in the operating point analysis requires the calculation of a magnetizing current versus magnetizing flux linkage curve for each design. A constraint c_{14} is used to check the convergence of the MEC in the construction of this relationship. If convergence occurs then the operating point analysis proceeds.

Within the design process, the operating point analysis is conducted for three load conditions: no-load, half-load, and full-load. A design constraint c_{15} is imposed on the convergence of the operating point analysis for the no-load case. If the operating point analysis converges, constraints on the β-winding maximum current and the range of the α-winding voltage are imposed as

$$c_{16} = \mathrm{lte}\left(\left|I_{\beta,1}\right|, I_{\beta,nlmxa}\right) \tag{7.45}$$

$$c_{17} = \mathrm{gte}\left(\left|V_{\alpha,1}\right|, V_{\alpha nl,mnr}\right) \tag{7.46}$$

$$c_{18} = \mathrm{lte}\left(\left|V_{\alpha,1}\right|, V_{\alpha nl,mxa}\right) \tag{7.47}$$

For the remaining load-conditions, it is useful to use the subscript 'k' to denote the operating point number, where $k = 1$ for half-load case and $k = 2$ for full-load case. Similar to the no-load case, a constraint c_{17+2k} is imposed on the convergence of each operating point analysis. A constraint on the transformer maximum temperature is also defined as

$$c_{18+2k} = \mathrm{lte}\left(T_{mx}, \mathrm{T}_{mxa}\right) \tag{7.48}$$

Considering the weight function $\mathbf{W}$, the weighted loss is a function of the loss at every operating point which is calculated as

$$P_l = \mathbf{w}^T \mathbf{P}_l \tag{7.49}$$

where $\mathbf{P}_l$ is a vector that contains the total loss corresponding to all operating points. The constraint on the total loss is obtained as

$$c_{19+2K} = \mathrm{lte}\left(P_l, P_{lmxa}\right) \tag{7.50}$$

where K is the number of operating points without including the no-load case, i.e., $K = 2$ and P_{lmxa} is the maximum allowed loss.

Before defining the fitness function, it is convenient to define the design specifications $\mathbf{D}_{ds}$ as follows

$$\begin{aligned}\mathbf{D}_{ds} = \Big[& f \;\; \omega_e \;\; V_{\beta 0} \;\; V_{\alpha nlmxa} \;\; V_{\alpha nlmnr} \;\; I_{\beta nlmxa} \;\; I_{\alpha fl} \;\; \chi_{mxa} \;\; \mathrm{i}_{\beta imxa} \;\; \lambda_{\beta wcs} \ldots \\ & \mathbf{V}_\beta \;\; \mathbf{Z}_l \;\; \boldsymbol{\omega}_\mathbf{e} \;\; \mathbf{W} \;\; P_{lmxa} \;\; M_{Tmxa} \;\; d_{Tmxa} \;\; w_{Tmxa} \;\; h_{Tmxa} \;\; k_{lmxa} \;\; k_{bdmnr} \ldots \\ & \eta_{mxa} \;\; T_{mxa} \;\; i_{\alpha,t} \;\; i_{\beta,t} \;\; N_{impt} \;\; N_{tpt} \;\; O_{emxa} \;\; O_{imxa} \Big]^T\end{aligned} \tag{7.51}$$

where $\mathbf{V}_\beta$, $\mathbf{Z}_l$, and $\boldsymbol{\omega}_\mathbf{e}$ are vectors of β-winding voltage, load impedance, and radian frequency values for different load conditions.

For more convenience, the design information vector defined in (7.21) and (7.51) are combined in one vector as

$$\mathbf{D} = \left[\mathbf{D}_{fp}^T \;\; \mathbf{D}_{ds}^T \right]^T \tag{7.52}$$

Finally, the fitness function is expressed as

$$f\left(\theta, D\right) = \begin{cases} \left[\dfrac{1}{M_T} \;\; \dfrac{1}{P_l} \right]^T & c = 1 \\ (c-1)\left[1 \; 1\right]^T & c < 1 \end{cases} \tag{7.53}$$

where

$$c = \frac{1}{n_c} \sum_{i=1}^{nc} c_i \tag{7.54}$$

where n_c is the number of constraints.

7.4. Example Design

As an example design, a single-phase tape-wound core-type transformer with a rated α-winding voltage $V_{\alpha\_rated} = 480$ V and a rated β-winding $V_{\beta\_rated} = 240$ V with a rated load of $S_{rated} = 5$ kVA and an operating frequency of 20 kHz was considered. The design specifications and fixed parameters are shown in Table 7.1.

Table 7.1 Transformer Design Specifications and Fixed Parameters.

Parameter	Value	Parameter	Value
f (Hz)	400	k_{bdmnr}	12
ω_e (rad/sec)	$2.51*10^3$	η_{mxa}	3
$V_{\beta 0}$ (V)	V_{β_rated}	T_{mxa} (K^o)	600
$V_{\alpha nlmxa}$ (V)	$1.02V_{\alpha\_rated}$	$i_{\alpha,t}$ (nA)	1
$V_{\alpha nlmnr}$ (V)	$0.98V_{\alpha\_rated}$	$i_{\beta,t}$ (nA)	1
$I_{\beta nlmxa}$ (A)	$0.1I_{\beta\_rated}$	N_{impt}	25
$I_{\alpha fl}$ (A)	I_{α_rated}	N_{tpt}	25
χ_{mxa}	0.05	O_{emxa}	10^{-3}
$\mathrm{i}_{\beta imxa}$ (A)	$2\sqrt{2}I_{\beta\_rated}$	O_{imxa}	10
$\lambda_{\beta wcs}$ (V.s)	$2\sqrt{2}V_{\beta\_rated}/\omega_e$	$c_{\alpha\beta}$ (mm)	2.5
$\mathbf{V}_\beta$ (V)	$V_{\beta\_rated}[1\ \ 1]$	$c_{\beta\beta}$ (mm)	2.5
$\mathbf{Z}_l$ (Ω)	$Z_{l\_rated}[2\ \ 1]$	$c^*_{\alpha v}$ (mm)	2.5
$\boldsymbol{\omega}_\mathbf{e}$ (rad/sec)	$\omega_e[1\ \ 1]$	$c^*_{\beta v}$ (mm)	2.5
$\mathbf{W}$	$[0.1\ \ 0.4\ \ 0.5]$	$k_{\alpha b}$	1.2
P_{lmxa} (W)	200	$N_{\alpha cs}$	1
M_{Tmxa} (kg)	60	$N_{\alpha cp}$	2
d_{Tmxa} (m)	1	$k_{\beta b}$	1.2
w_{Tmxa} (m)	1	$N_{\beta cs}$	1
h_{Tmxa} (m)	1	$N_{\beta cp}$	2

In Table. 7.1, the rated currents are calculated as

$$I_{\alpha\_rated} = \frac{S_{rated}}{V_{\alpha\_rated}} \tag{7.55}$$

$$I_{\beta\_rated} = \frac{S_{rated}}{V_{\beta\_rated}} \tag{7.56}$$

and the rated load impedance is expressed as

$$Z_{l\_rated} = \frac{V_{\alpha\_rated}}{I_{\alpha\_rated}} \tag{7.57}$$

The transformer design space parameters are coded as genes as shown in Table 7.2. The range of each gene is set by defining minimum and maximum limits. The limits are based on practice and can be flexibly changed as desired. As shown, the gene type is defined as integer ‘int’ when the parameter represents a material type. The gene type is defined as linear ‘lin’ when the parameter represent a fraction and it is defined as logarithmic ‘log’ when the parameter vary within a large range such as the transformer dimensions.

Table. 7.2 Transformer Design Parameters

No.	Par.	Description	Min.	Max.	Type
1	m_c	Core material	1	5	int
2	d_w	Depth of winding (m)	10^{-4}	1	log
3	$c_{\alpha c}$	α- winding to core clearance (m)	$2*10^{-3}$	10^{-2}	log
4	h_{bce}	Vertical distance between bending center and core edge (m)	10^{-4}	$2*10^{-1}$	log
5	w_{bce}	Horizontal distance between bending center and core edge (m)	10^{-4}	$2*10^{-1}$	log
6	w_{es}	Coil straight length on end (m)	10^{-4}	10^{-1}	log
7	r_{ci}	Core inner radius (m)	10^{-5}	$2*10^{-2}$	log
8	m_β	β- winding material	1	2	int
9	$a^*_{\beta t}$	Desired area of β- winding conductors (m^2)	10^{-6}	10^{-3}	log
10	$N^*_{\beta pr}$	Desired number of β- conductors in parallel	1	5	int
11	$N^*_{\beta cl}$	Desired Number of β- coil turns	10	10^3	log
12	$R^*_{\beta hw}$	Desired β- coil height to width ratio	0.2	5	log
13	m_α	α- winding material	1	2	int
14	$a^*_{\alpha t}$	Desired area of α- winding conductors (m^2)	10^{-6}	10^{-3}	log
15	$N^*_{\alpha pr}$	Desired number of α- conductors in parallel	1	5	int
16	$R^*_{N\beta\alpha}$	Desired β- winding to α- winding turns ratio	$0.95\frac{V_{\beta\_rated}}{V_{\alpha\_rated}}$	$1.05\frac{V_{\beta\_rated}}{V_{\alpha\_rated}}$	lin
17	$R^*_{\alpha hw}$	Desired α- coil height to width ratio	0.2	5	log

To establish the design, GOSET [1] was applied with a population size of 1000 over 1000 generations. The resulting Pareto-optimal front (POF) which show a trade-off between total mass and total loss is shown in Fig. 7.1. Design 100 which is highlighted by red circle is selected from the POF to be presented in details. The parameter distribution plot is illustrated in the Appendix.

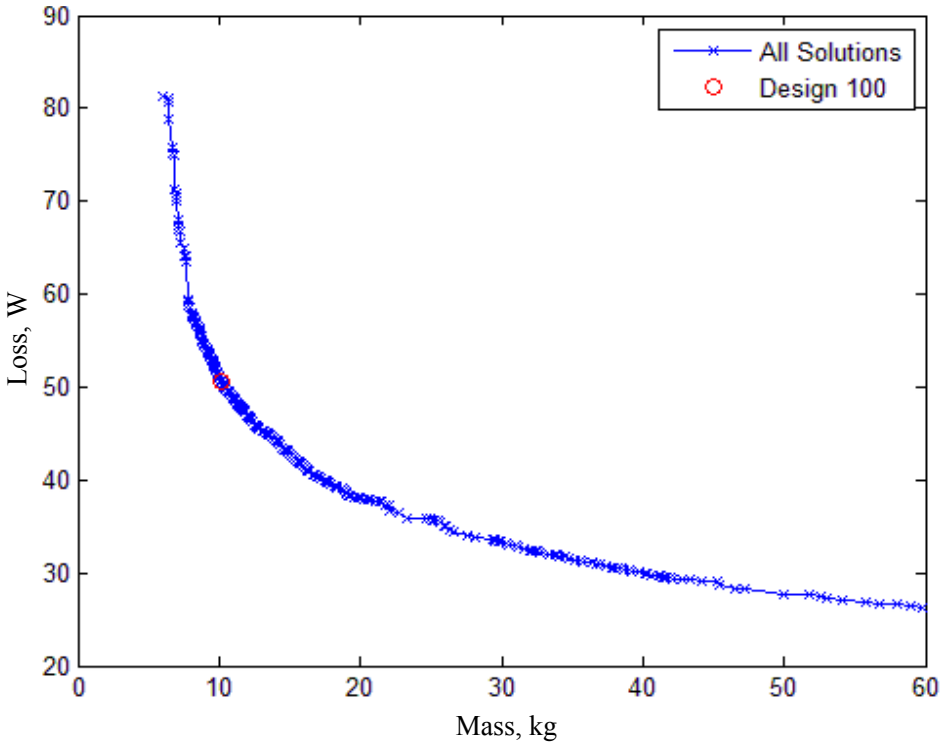

Fig. 7.1 Transformer Design Pareto-Optimal Front

The top and front cross-sectional views of design 100 are depicted in Fig. 7.2. As shown, the bending starts before the core tip which leads to minimizing the clearance between the coil and the core in the depth direction. Also as enforced by one of the constraints, the height of the β-winding coils are less than the height of the α-winding coils. The parameters of this design are shown in Table 7.2 and the electrical parameters are shown in Table 7.4.

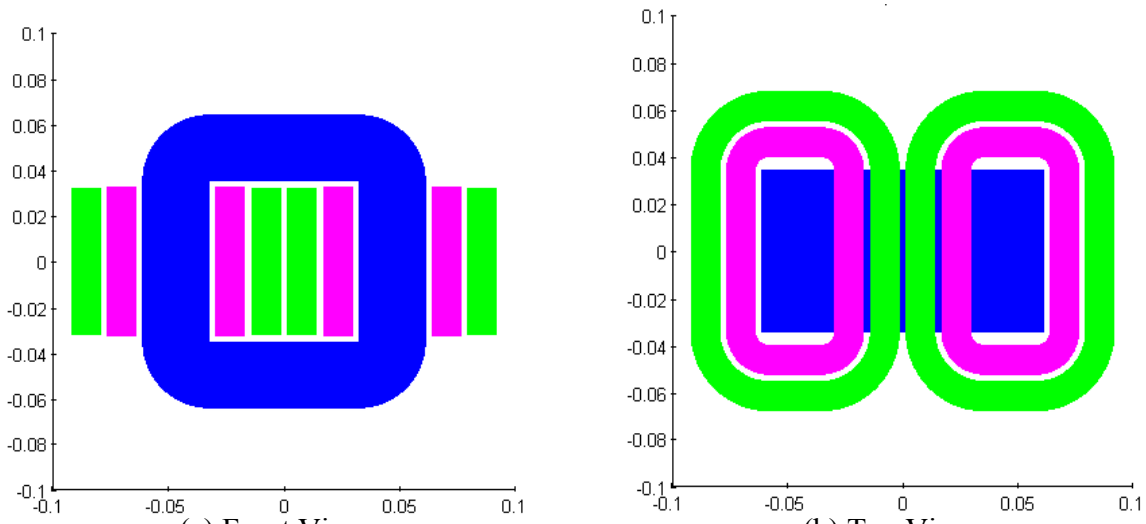

(a) Front View (b) Top View

Fig. 7.2 Transformer Cross-sectional View

Table 7.3 Parameters of Design 100

Core		β-winding		α-winding	
Par.	Value	Par.	Value	Par.	Value
Material	Hiperco50	Material	Copper	Material	Copper
d_c	6.93 cm	AWG	16	AWG	19
h_{co}	12.84 cm	$r_{\beta c}$	6.45 cm^2	$r_{\alpha c}$	4.56 cm^2
w_{co}	12.24 cm	$N_{\beta cs}$	1	$N_{\alpha cs}$	1
h_{ci}	7.03 cm	$N_{\beta cp}$	2	$N_{\alpha cp}$	2
w_{ci}	6.43 cm	$N_{\beta pr}$	4	$N_{\alpha pr}$	4
t_c	2.91 cm	$N_{\beta uw}$	8	$N_{\alpha uw}$	11
r_{ci}	1*10^{-5} m	$N_{\beta uh}$	10	$N_{\alpha uh}$	14
A_c	20.12 cm^2	w_β	1.3 cm	w_α	1.28 cm
U_c	725 cm^3	h_β	6.48 cm	h_α	6.53 cm
M_c	5.69 kg	$r_{\beta i}$	2.09 cm	$r_{\alpha i}$	0.56 cm
		$r_{\beta o}$	3.39 cm	$r_{\alpha o}$	1.84 cm
		$k_{\beta pf}$	49.8 %	$k_{\alpha pf}$	48.01 %
		$k_{\beta bd}$	32.41	$k_{\alpha bd}$	12.24
		M_β	2.64 kg	M_α	1.84 kg

Table 7.4 Electrical Parameters

Par.	Value	Par.	Value	Par.	Value
$N_\beta : N_\alpha$	80 : 154	r_β	45.48 mΩ	$r_\alpha^{'}$	34.4 mΩ
L_{m0}	2.38 H	$L_{l\beta}$	135.5 μH	$L_{l\alpha}^{'}$	56.4 μH

The β-winding flux linkage versus current is depicted in Fig. 7.3. As shown the inrush current (plotted in green) is less than the allowed inrush current (plotted in red) which satisfies the design requirement.

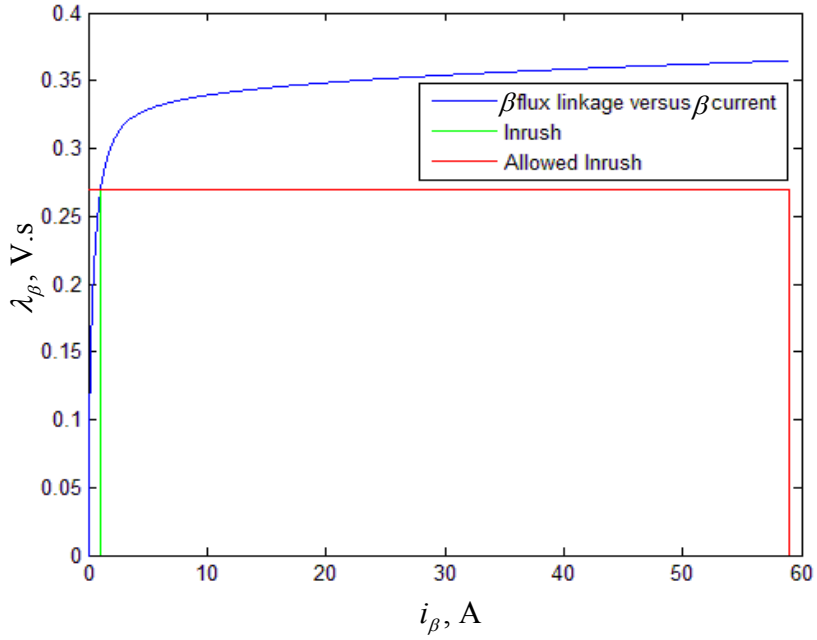

Fig. 7.3 β -winding Flux Linkage versus Current

The parameters of the operating point analysis are shown in Table 7.5. From these parameters there are several observations. For one, the core loss is almost independent of the load current and it represents nearly all of the transformer total loss at the no-load case. The winding loss depends directly on the load current and they represent about 23% of the total loss at half-load and about 57% at the full-load case. Over an operation cycle, the transformer load condition varies between no-load, when there is nearly only a core loss, and full-load, when the winding loss becomes higher than core loss. Therefore, both transformer losses are significant and it is desired to minimize their net. As one may expect the transformer maximum temperature correlate to winding currents. A difference of about 96 C^o between no-load and full-load case is observed. The thermal analysis is performed under the assumption that the ambient temperature is assumed to be 20 C^o. One may expect that the transformer maximum temperature should be equal to the ambient temperature at no-load case. However, due to core loss, the maximum temperature at no-load case is equal to 61 C^o.

Table 7.5 Operating Point Data

Par.	No Load	Half Load	Full Load
V_β (V)	$240\angle 0^o$	$240\angle 0^o$	$240\angle 0^o$
f (Hz)	400	400	400
Z_L (Ω)	∞	$92.16\angle 0^o$	$46.08\angle 0^o$
I_β (A)	$0.15\angle -38.3^o$	$9.73\angle -1.66^o$	$19.24\angle -2.48^o$
V_α (V)	$461.9\angle -0.0085^o$	$460.19\angle -1.12^o$	$457.79\angle -2.21^o$
I_α (A)	0	$4.99\angle 178.88^o$	$9.93\angle 177.79^o$
r_β (mΩ)	48.85	50.33	56.4
$r_\alpha^{'}$ (mΩ)	37.14	38.91	46.37
$S_{\beta r}$ (W)	0.0011	4.8	21
$S_{\alpha r}$ (W)	0	3.62	17.06
S_{cl} (W)	28.343	28.2	28
S_l (W)	28.344	36.63	66.06
R_c (kΩ)	2.032	2.033	2.035
L_m (H)	1.025	1.028	1.031
J_β (A/mm^2)	0.0144	0.93	1.84
J_α (A/mm^2)	0	0.956	1.9
T_{mx} (C^o)	61	77.85	157.38

The flux density in the core vertical leg, horizontal leg, and the corner segments at no-load are shown in Fig. 7.4. As shown, the peak value of the flux density in the interior segment of the core corner is higher than the peak value of the flux density in the other core regions. In addition, the variance in the flux density levels between the corner segments proves the importance of dividing the core corner into several parallel segments. It is also noted that the flux density waveforms in the vertical and horizontal core legs are almost identical which is expected since they have the same cross-sectional area and their corresponding permeances can be considered as being series connected if the leakage flux is neglected.

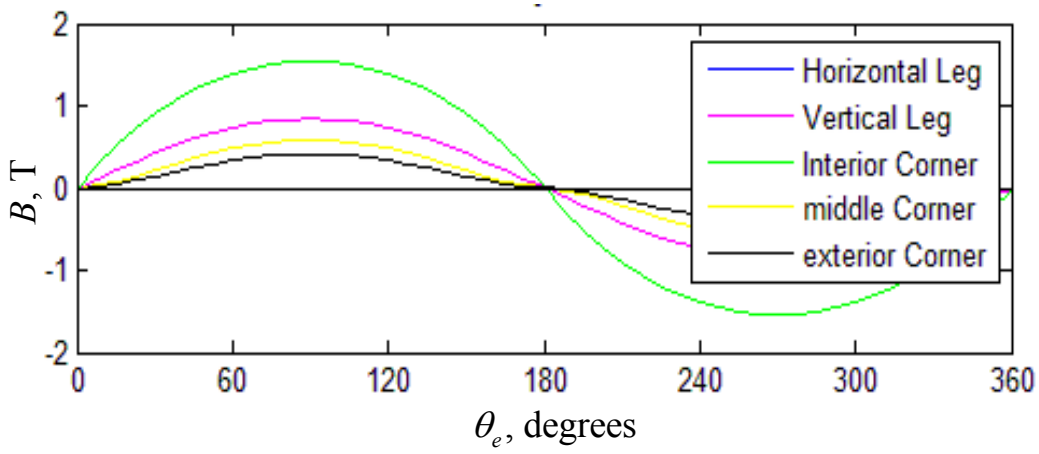

Fig. 7.4 No-load Flux Density

The transformer maximum temperature versus mass is depicted in Fig. 7.5. It is noted that as the mass increases, the maximum temperature goes down.

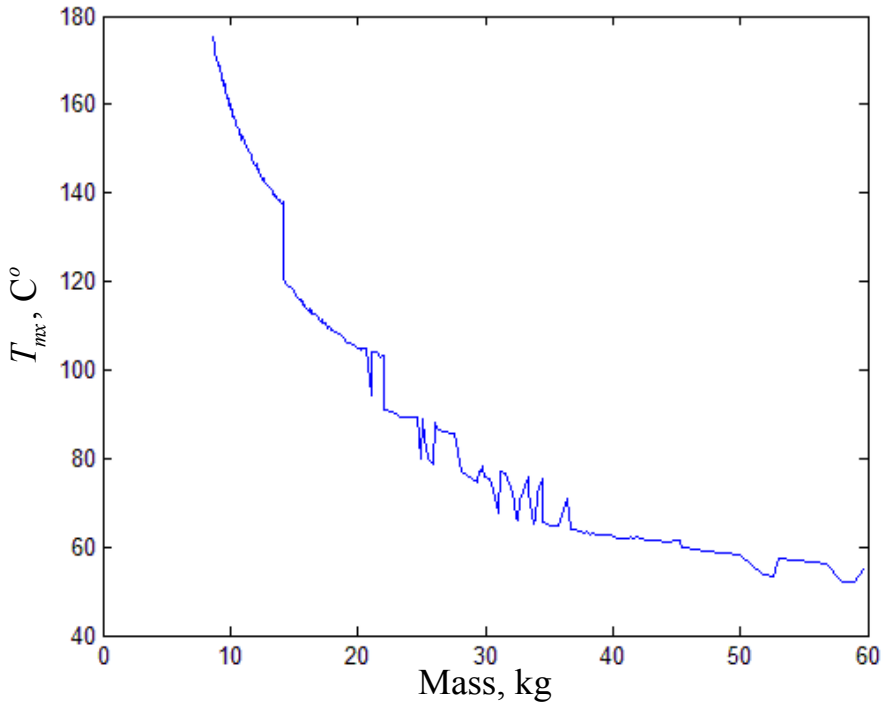

Fig. 7.5 Maximum Temperature Versus Mass at Full Load

8. SCALED DESIGN APPROACH

The objective of the research presented in this chapter is to develop meta-model based scaling laws for the tape wound transformer model derived in the previous chapters. Prior to doing so, the possibility of developing the meta-model based scaling laws is initially explored using a simplified two winding transformer. The purpose of considering this simplified transformer is mainly to develop and validate the scaling laws. Therefore, some crude approximations are initially made to simplify analysis such as neglecting the leakage inductances and eddy current loss and assuming linear magnetizing curve. Subsequently, the meta-model is derived for the tape wound transformer in great details.

As will be discussed in this chapter, scaling laws enable one to approximate key performance metrics, i.e. loss and mass, based upon device power ratings without requiring one to perform a detailed component optimization [41]. Often, large degree of freedom component-level optimization within the context of a system-level optimization is intractable.

To explore scaling laws, a simplified two winding, core type transformer shown in Fig. 8.1 is initially considered. The α-winding (lighter orange) is wound on the left leg and the β-winding (darker orange) is wound on the right leg. For simplicity, the two windings are assumed to have the same dimensions and the clearances between the windings and the core are neglected; therefore,

$$w_\alpha = w_\beta = \frac{w_{ci}}{2} \tag{8.1}$$

and

$$h_\alpha = h_\beta = \frac{h_{ci}}{2} \tag{8.2}$$

where w_α, w_β, and w_{ci} are the widths of α-winding, β-winding, and core interior window respectively and h_α, h_β, and h_{ci} are the heights of α-winding, β-winding, and core interior window respectively. It should be noted that when the scaling of the tape-wound transformer is considered in Section 8.6, the winding to winding and winding to core clearances will not be neglected and the winding heights and widths do not have to be equal.

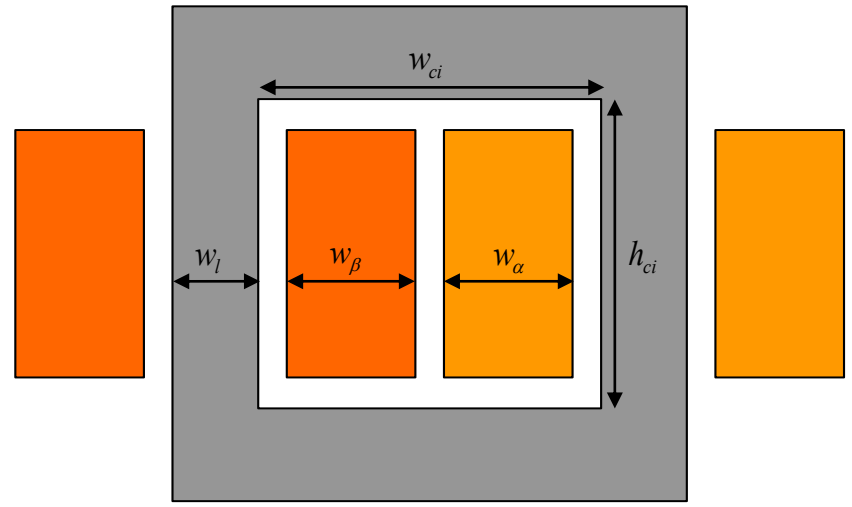

(a) Front View

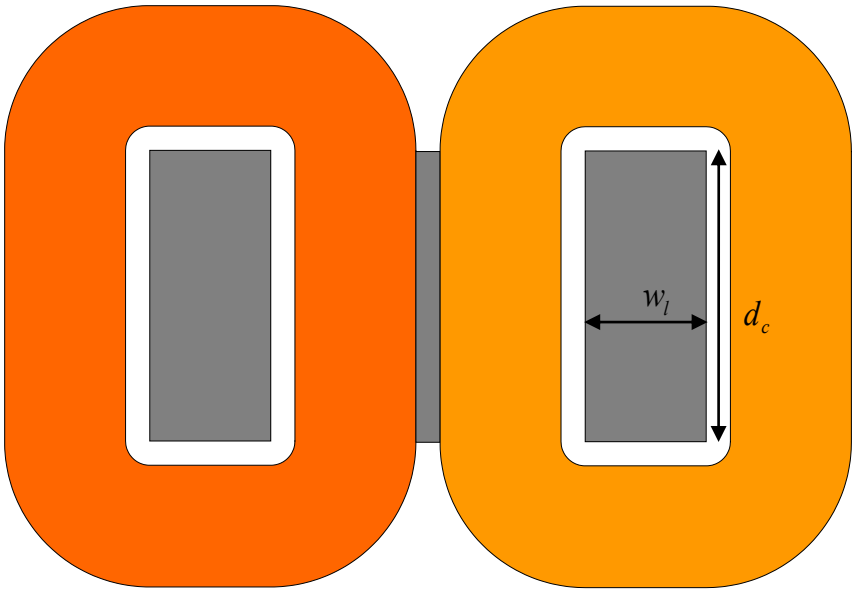

(b) Top View

Fig. 8.1 Two Winding Core Type Transformer Cross Section

Prior to considering scaling, it is useful to define and describe several key parameters of the transformer. The rms current density for winding j is expressed as

$$J_j = \frac{N_j I_j}{A_j k_{pf}} \tag{8.3}$$

where N_j and I_j are the j-winding number of turns and rms current respectively, k_{pf} is the winding packing factor, and A_j is the area of the j-winding. The winding area is represented by

$$A_j = w_j h_j \tag{8.4}$$

In Section 8.6, the current densities of both windings do not have to be the equal but initially for the simplified model, the α-winding and β-winding rms current densities are assumed to be equal

$$J_\alpha = J_\beta = J \tag{8.5}$$

The mass is another quantity of interest and is given by

$$M = 2d_c w_l \left(w_{ci} + h_{ci} + 2w_l\right)\rho_c + \sum_{j=\alpha,\beta} k_{pf} U_j \rho_{jc} \tag{8.6}$$

where ρ_c and ρ_{jc} are the mass density of core material and j-winding conductor respectively and U_j is the volume of winding x which is calculated by

$$U_j = h_j w_j \left(2\left(d_c + w_l\right) + \pi w_j\right) \tag{8.7}$$

As shown in previous chapters, it is convenient to utilize a T-equivalent circuit when analyzing transformers. Initially for the simplified model, the T-equivalent circuit shown in Fig. 8.2 is considered. As shown, the leakage flux is neglected and it is assumed that the magnetizing curve is linear. In Section 8.6, leakage inductances will be included in the T-equivalent circuit to account for the leakage flux and the operating point analysis will be performed to evaluate the magnetizing branch parameters due to the non-linearity of the magnetizing curve. Within the circuit, the referred (primed) α-winding rms voltage, rms current and resistance are expressed as

$$V_{\alpha}^{'} = \frac{N_{\beta}}{N_{\alpha}} V_{\alpha} \tag{8.8}$$

$$I_{\alpha}^{'} = \frac{N_{\alpha}}{N_{\beta}} I_{\alpha} \tag{8.9}$$

$$r_{\alpha}^{'} = \left(\frac{N_{\beta}}{N_{\alpha}} \right)^2 r_{\alpha} \tag{8.10}$$

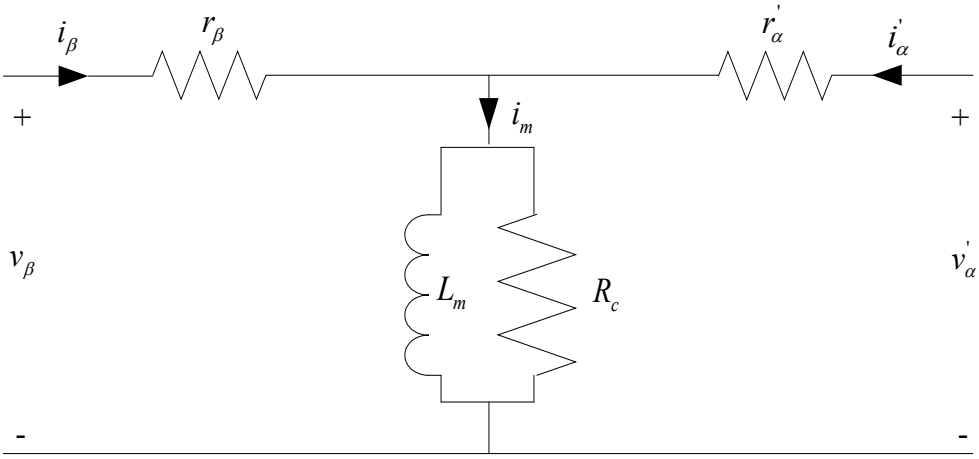

Fig. 8.2 Transformer T-equivalent Circuit

The flux path inside the core is assumed to be the average path. The peak flux density is expressed

$$B_{pk} = \frac{\sqrt{2} N_{\beta} I_m P}{A_c} \tag{8.11}$$

where I_m is the rms magnetizing current, A_c is the core cross-sectional area, and P is the core permeance which is calculated using the relationship

$$P = \frac{\mu A_c}{l_p} \tag{8.12}$$

In (8.12), μ is the core material permeability and l_p is the flux path average length inside the core which is expressed as

$$l_p = 2\left(w_{ci} + h_{ci} + 2w_l\right) \tag{8.13}$$

Neglecting the core loss resistance and the voltage drop on the resistance of the β-winding, r_β; the rms magnetizing current can be approximated

$$I_m = \frac{V_\beta}{\omega_e L_m} \tag{8.14}$$

where V_β is the rms value of the β-winding terminal voltage, ω_e is the angular frequency of the sinusoidal primary voltage, and L_m is the magnetizing inductance which is defined as

$$L_m = N_\beta^2 P \tag{8.15}$$

Using (8.3), (8.12)-(8.15) and (8.11) and simplifying one can approximate the peak flux density using:

$$B_{pk} = \frac{\sqrt{2}S_r}{J_r A_c A_\beta \omega_e k_{pf}} \tag{8.16}$$

where P_r and J_r the transformer rated power and rated current density respectively.

Typically, the magnetizing current is required to be much less than the rated current. This can be achieved by enforcing this constraint

$$I_m < \frac{S_r}{V_\beta} k_m \tag{8.17}$$

where k_m is a constant which is much less than 1. Substituting equations (8.3), (8.14), and (8.15) into (8.17) and simplifying yields

$$J_\beta^2 > \frac{S_r}{\omega_e k_m A_\beta^2 k_{pf}^2 P} \tag{8.18}$$

It is very interesting to consider (8.17) and (8.18). Although the magnetizing current is equal to the sum of the α-winding and the β-winding currents as in Fig. 8.2, its upper limit can be enforced by setting a lower limit on the β-winding current density.

8.1. Normalization Base

The objective of this section is to set the stage for the normalization process by defining the normalization base. The goal is to scale all quantities tied to ratings (i.e. dimensions) and not those that are rating independent (i.e. flux density and field intensity) [41].

One can note from the previous section that many of the key constraints can be expressed in terms of current density. This makes the current density a good candidate to be a parameter in the scaling laws (in addition to power and frequency). Another advantage of selecting the current density as a parameter is that it is a general quantity. In other words, a particular value of the current density may correspond to a wide range of transformer sizes, power ratings, and voltage levels.

8.1.1. Geometrical Quantities

To establish the meta-model, the linear dimensions are scaled as [41]

$$\hat{x} = x / D \tag{8.19}$$

In (8.19), the notation '^' denotes the scaled quantity and D is the normalization base. The area and volume are scaled accordingly using [41]

$$\hat{a} = a / D^2 \tag{8.20}$$

$$\hat{U} = U / D^3 \tag{8.21}$$

Substituting (8.19) and (8.21) into (8.6), normalized mass is expressed as

$$\hat{M} = 2\hat{l}_c \hat{w}_l \left(\hat{w}_{ci} + \hat{h}_{ci} + 2\hat{w}_l \right) \rho_c + \sum_{j=\alpha,\beta} k_{pf} \hat{U}_j \rho_{jc} \tag{8.22}$$

where

$$\hat{M} = M / D^3 \tag{8.23}$$

8.1.2. Electrical Quantities

It is desired not to scale the flux density when deriving the meta-model. Considering (8.11), (8.12), (8.19), and (8.20), to keep B_m unscaled the current must be scaled as [41]

$$\hat{i} = i / D \tag{8.24}$$

From (8.3), (8.20), and (8.24), the current density is expressed

$$\hat{J} = JD \tag{8.25}$$

The flux linkage associated with winding j is expressed as

$$\lambda_j = N_j \int_{S_j} B \cdot ds \tag{8.26}$$

where S_j is the surface.

Since the flux density is not scaled [41], then from (8.20), the scaled flux linkage can be expressed

$$\hat{\lambda} = \lambda / D^2 \tag{8.27}$$

The instantaneous voltage associated with winding j is calculated

$$v_j = \frac{l_j N_j}{\sigma a_j} i_j + \frac{d\lambda_j}{dt} \tag{8.28}$$

where j and a_j are the winding j wire length and area respectively, i_j is winding j instantaneous current and σ is the winding conductor material conductivity.

If time is scaled as [41]

$$\hat{t} = t / D^2 \tag{8.29}$$

then from (8.19), (8.20), (8.24), and (8.27), the voltage can be expressed in terms of scaled quantities as [41]

$$v_j = \frac{\hat{l}_j N_j}{\sigma \hat{a}_j} \hat{i}_j + \frac{d\hat{\lambda}_j}{\hat{dt}} \tag{8.30}$$

From which one can observe that voltage is not scaled.

The frequency is the reciprocal of time and therefore, from (8.29) the frequency is scaled as

$$\hat{f} = fD^2 \tag{8.31}$$

Since the relationship between the angular frequency and the frequency is

$$\omega = 2\pi f \tag{8.32}$$

then

$$\hat{\omega} = \omega D^2 \tag{8.33}$$

From (8.16), (8.19), (8.25), and (8.33), the flux density is expressed in terms of the scaled quantities as

$$B_{pk} = \frac{\sqrt{2}\hat{S}_r}{\hat{J}_\beta \hat{A}_c \hat{A}_\beta \hat{\omega}_e k_{pf}} \tag{8.34}$$

where the scaled rated power is defined as [41]

$$\hat{S}_r = S_r / D \tag{8.35}$$

From (8.12), (8.19), and (8.20) the scaled permeance is

$$\hat{P} = \frac{\mu \hat{A}_c}{\hat{l}_p} \tag{8.36}$$

where

$$\hat{P} = P / D \tag{8.37}$$

the constraint on current density (8.18) can be expressed in terms of scaled quantities

$$\hat{J}_\beta^2 > \frac{\hat{S}_r}{\hat{\omega}_e k_m \hat{A}_\beta^2 k_{pf}^2 \hat{P}} \tag{8.38}$$

8.1.3. Voltage Regulation

As mentioned in Chapter 6, due to the winding resistances and leakage inductances, the secondary voltage of a transformer varies with load condition. It is desired in practice to keep this variation within a specified margin which depends on the type of the load and its sensitivity to voltage variations. During normal operation of a transformer, the largest variation in the secondary voltage occurs when the load condition changes from no-load to full-load. Thus, the voltage regulation is defined as the absolute difference between the secondary voltage at full-load and the one at no-load relative to the voltage at no-load:

$$\chi = \left| \frac{V'_{\alpha,fl} - V'_{\alpha,nl}}{V'_{\alpha,nl}} \right| \tag{8.39}$$

To simplify analysis, the leakage inductances are neglected in the initial scaling derivations as shown by the transformer electric equivalent circuit in Fig. 8.2. The leakage inductances will be accounted for in Section 8.6. In addition, the voltage drop on the primary resistance is neglected at no-load since the magnetizing impedance is relatively large compared to the primary resistance. The magnetizing current is neglected

at full-load since it is much smaller than the rated load current as enforced by (8.17). Therefore, the transformer voltage regulation can be approximated as

$$\chi = \left(r_\beta + r_\alpha^{'}\right)\frac{I_\alpha^{'}}{V_\beta} \tag{8.40}$$

Using (8.3), (8.9), (8.10), and (8.40) the voltage regulation can be expressed as

$$\chi = \frac{J_\alpha J_\beta k_{pf}}{\sigma S_r}\left(\frac{A_\alpha}{A_\beta}U_\beta + \frac{A_\beta}{A_\alpha}U_\beta\right) \tag{8.41}$$

Although voltage is not scaled, the voltage regulation can be expressed in terms of scaled quantifies

$$\chi = \frac{\hat{J}_\alpha \hat{J}_\beta k_{pf}}{\sigma \hat{S}_r}\left(\frac{\hat{A}_\alpha}{\hat{A}_\beta}\hat{U}_\beta + \frac{\hat{A}_\beta}{\hat{A}_\alpha}\hat{U}_\beta\right) \tag{8.42}$$

8.1.4. Loss

Transformer power loss is comprised of transformer winding electrical resistance loss and core loss. The resistive power lost in winding j is calculated using

$$S_{loss\_j} = I_j^2 N_j^2 \frac{U_j}{k_{pf} A_j^2 \sigma} \tag{8.43}$$

From (8.3) and (8.43) the resistive power lost due to winding j may be formulated in terms of the rms current density as

$$S_{loss\_j} = \frac{U_j k_{pf} J_j^2}{\sigma} \tag{8.44}$$

It is noted that the resistive power loss in both windings are equal since the current density and the winding dimensions are assumed to be the same for both windings. Thus, the total resistive loss is twice that in (8.44). Expressed in terms of scaled quantities using, (8.21), (8.25), and (8.35) to (8.44) yields

$$\hat{S}_{loss\_j} = \frac{\hat{U}_j k_{pf} \hat{J}_j^2}{\sigma} \tag{8.45}$$

Core loss includes hysteresis loss and eddy current loss. To demonstrate the hysteresis loss, Fig. 8.3 is first considered. At each cycle, the flux density follows the

lower path when it is increasing and it follows the upper path when it is decreasing. Therefore, the trajectory of the flux density forms a loop and the area of this loop represents energy lost in the core in form of heat. This lost energy is referred to as hysteresis loss. Typically, the flux density waveform is not a pure sinusoidal function due to the effect of saturation. Initially, the flux density waveform is assumed to be sinusoidal by neglecting the saturation effect but in Section 8.6, the flux density waveform may not be sinusoidal due to saturation. Thus the hysteresis loss is initially estimated using MSE [13]

$$S_h = k_h B_{\max}^{\beta_h} f^{\alpha_h} U_c \tag{8.46}$$

where k_h, α_h, and β_h are the hysteresis loss constants.

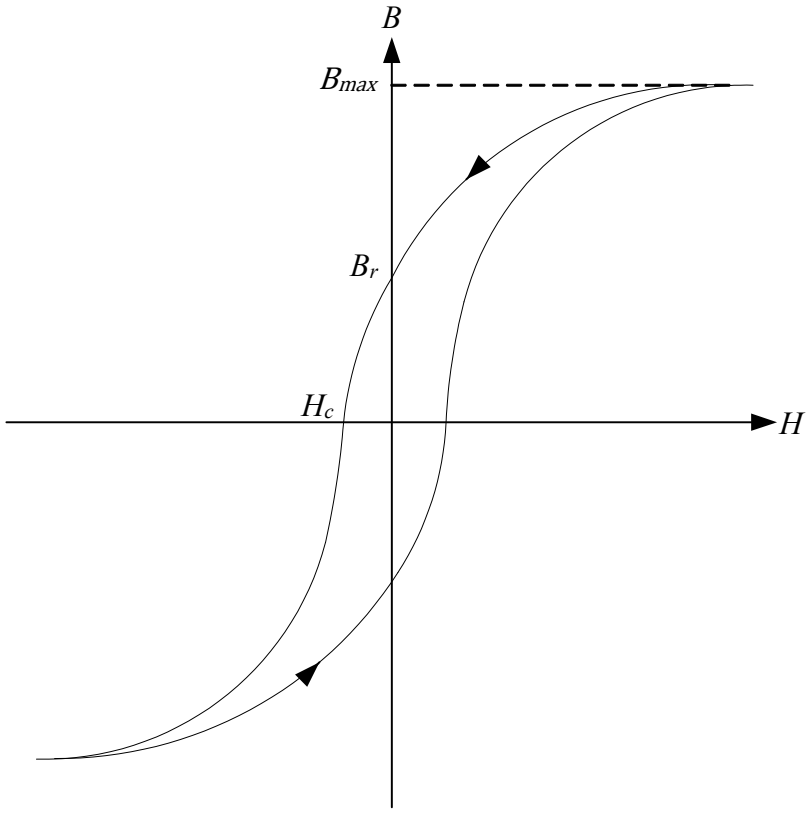

Fig. 8.3 Magnetizing Curve for a Soft Magnetic Material

The eddy current loss is initially approximated using MSE [13]

$$S_e = k_e B_{\max}^2 f^2 U_c \tag{8.47}$$

where k_e is the eddy current loss constant.

The total core loss is the sum of the hysteresis and eddy current loss; thus,

$$S_{cl} = S_h + S_e \tag{8.48}$$

To enable scaling of the hysteresis loss in (8.46), the constant α_h must be an integer. Typically α_h is very close to 1 and thus it is herein approximated to be 1. The hysteresis loss is thus modeled

$$S_h = k_h B_{\max}^{\beta_h} f U_c \tag{8.49}$$

Applying (8.21), (8.31), and (8.35) to (8.49) yields a scaled loss

$$\hat{S}_h = k_h B_{\max}^{\beta_h} \hat{f} \hat{U}_c \tag{8.50}$$

To obtain the scaled eddy current loss, (8.21), (8.31), and (8.35) are substituted in (8.47) which yields

$$\hat{S}_e = \left(k_e B_{\max}^2 \hat{f} \hat{U}_c \right) f \tag{8.51}$$

8.1.5. Nominal Design Performance

Before starting the scaled design process, it is useful to explain how one can apply the equations derived thus far to a specific design. If the voltage of winding j and transformer rated power are defined, then the winding j rated current is calculated using

$$I_j = \frac{S_r}{V_j} \tag{8.52}$$

If the winding j current density is defined and the winding dimensions are known, then the number of turns for the corresponding winding is calculated using (8.3). After calculating the current density, the transformer performance equations can be evaluated.

8.1.6. Normalization Base Selection

The selection of the normalization base is a very crucial step. Since transformers are typically defined in terms of the rated power, the base of normalization is selected to be the rated power; thus,

$$D = S_r \tag{8.53}$$

8.2. Simplified Two Winding Transformer Design Process

Prior to considering the tape-wound transformer detailed design process, the design process of the simplified two winding transformer is considered. Using, the scaled model defined by equations (8.19)-(8.51), transformer design is considered to establish Pareto-optimal fronts from which a meta-model can be proposed.

The first step in the design process is to define the design vector as

$$\hat{\mathbf{\theta}} = \left[\hat{J}_r \;\; \hat{h}_{ci} \;\; r_{ci} \;\; r_l \;\; r_c \right]^T \tag{8.54}$$

where the ratios r_{ci} , r_l , and r_c are defined as

$$r_{ci} = \frac{\hat{w}_{ci}}{\hat{h}_{ci}} \tag{8.55}$$

$$r_l = \frac{\hat{w}_l}{\hat{h}_{ci}} \tag{8.56}$$

$$r_c = \frac{\hat{l}_{ci}}{\hat{h}_{ci}} \tag{8.57}$$

The second step is to implement the design constraints. The less-than and greater-than functions discussed in Chapter 7 are used to represent the scaled design constraints.

The first constraint is the constraint on the current density

$$c_1 = \text{gte}\left(\hat{J}_r, \hat{J}_{mnr} \right) \tag{8.58}$$

where the minimum required current density $\hat{J}_{mnr}$ is

$$\hat{J}_{mnr} > \sqrt{\frac{\hat{S}_r}{\hat{\omega}_e k_m \hat{A}_\beta^2 k_{pf}^2 \hat{P}}} \tag{8.59}$$

The second constraint is imposed on the voltage regulation as

$$c_2 = \text{lte}\left(\chi, \chi_{mxa}\right) \tag{8.60}$$

In the analysis used to develop the scaled model, the magnetic material is assumed to be linear. Therefore, a constraint is imposed on the flux density as

$$c_3 = \text{lte}\left(B_{pk}, B_{mxa}\right) \tag{8.61}$$

A final constraint is imposed on the total power loss $\hat{P}_l$ as follows

$$c_4 = \text{lte}\left(\hat{S}_l, \hat{\text{S}}_{l,mxa}\right) \tag{8.62}$$

The fitness function used for the performance evaluations is defined as

$$f\left(\theta\right) = \begin{cases} \begin{bmatrix} \dfrac{1}{\hat{M}} & \dfrac{1}{\hat{S}_l} \end{bmatrix}^T & c = 1 \\ \left(c-1\right)\begin{bmatrix} 1 & 1 \end{bmatrix}^T & c < 1 \end{cases} \tag{8.63}$$

where c is defined as

$$c = \frac{1}{n_c}\sum_{i=1}^{n_c} c_i \tag{8.64}$$

and n_c is the number of constraints.

The fitness function is calculated using the Pseudo-code as illustrated in Table 8.1.

Table 8.1 Multi-Objective Optimization Pseudo-Code

1. define $\hat{\omega}$, k_{pf}, the material parameters, χ_{mxa}, and B_{mxa}
2. determine the parameters of the design vector in (8.54)
   evaluate transformer dimensions
   evaluate χ using (8.42) and B_{pk} using (8.34)
   calculate $\hat{J}_{mnr}$ using the RHS of (8.38).
3. evaluate c_1, c_2, c_3, and c_4 using (8.58) and (8.60)-(8.62).
   evaluate c using (8.64)
4. calculate $\hat{M}$ using (8.22)
   calculate $\hat{P}_{loss\_j}$ using (8.45)
   calculate $\hat{P}_h$ using (8.50)
   evaluate the total loss $\hat{P}_l = 2\hat{P}_{loss\_j} + \hat{P}_h$
   use (8.63) to evaluate the fitness function
   return to step 2

end

To define the search space of the multi-objective optimization process, the range of the scaled parameters is defined as follows: $10^5 \le \hat{J} \le 10^{20}$ AW/m^2, $10^{-12} \le \hat{h}_{ci} \le 0.1$ m/W, $0.1 \le r_{ci} \le 10$, $10^{-2} \le r_l \le 10$, and $0.1 \le r_c \le 10$, where r_{ci}, r_l, r_c, and are unit-less. The packing factor k_{pf} is selected to be 0.6, the maximum allowed ratio between the magnetizing and the rated current k_m is chosen to be 0.05, the maximum voltage regulation χ_{mxa} is set to 0.05, the upper limit on the flux density χ_{mxa} is 1.4 T, the winding conductor is selected to be copper which has a conductivity σ of 5.959*10^7 S/m and a mass density of 8890 Kg/m^3, and the steel material is chosen to be linear with relative permeability μ_r that is equal to 5000, mass density of 7402 Kg/m^3, and the hysteresis loss constants are chosen to be 64.064 J/m^3 for k_h and 1.7991 for β_h.

Based on the result in (8.51), the scaled eddy current loss is a function of the nominal frequency which is undesired in the scaling process. Initially, this problem can be addressed by neglecting the eddy current loss and only considering the scaled hysteresis loss defined in (8.50) to represent the total core loss. This may be acceptable in the low frequency range where the hysteresis loss is the dominant core loss. Therefore, to make the model valid for higher frequencies, a better approach than neglecting the scaled eddy current loss should be used. In Section 8.6, an assumption will be made to enable scaling the eddy current loss.

After defining the design parameters, specifications, and constraints, a multi-objective optimization is conducted with a population size of 2000 and for 2000 generations.

8.3. Multi-Objective Optimization Results of the Two Winding Transformer

Using the range of the scaled design parameters and the fixed parameters defined in the previous section and defining the scaled frequency, a multi-objective optimization is performed to obtain the Pareto-optimal front which relates the normalized mass to the normalized loss. The normalized loss versus normalized mass when the normalized frequency is $3.75*10^{10}$ HzW^2 is shown in Fig. 8.4. This value corresponds to a nominal frequency of 60 Hz at rated power of 25 kW. As shown in Fig. 8.4, the relationship between normalized loss and normalized mass is composed of two linear regions in the log-log scale. Typically, transformers tend to operate around the knee of the magnetization curve. Since the steel material is initially assumed to be linear for the simplified two winding transformer, the operating point of the transformer will tend to be against the upper flux density limit. Therefore, the region where the designs are against the upper flux density limit (plotted in red) is selected to obtain the meta-model based scaling law. The gene distribution plot is shown in the Appendix.

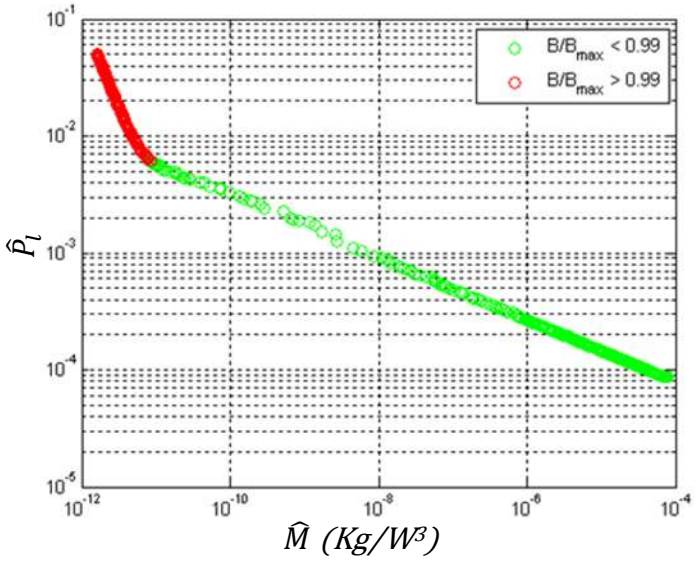

Fig. 8.4 Normalized Pareto-Optimal Front

In order to construct meta-model based scaling laws that relate normalized mass and normalized loss to normalized frequency and normalized current density, the multi-objective optimization is conducted at several values of the normalized frequency. Then the values of $\hat{J}$ at each frequency is evaluated and used to obtain plots of the normalized mass versus normalized current density and normalized loss versus normalized current density at each normalized frequencies. These are depicted in Fig. 8.5 and Fig. 8.6 respectively.

8.4. Meta-Model of the Two Winding Transformer

By using curve fitting techniques, a meta-model based scaling law can be constructed from the results shown in Fig. 8.5 and Fig. 8.6. The goal is to express the normalized mass and loss as functions of normalized frequency and current density. Relationships of the form

$$\hat{M} = C_M \hat{f}^{n_{fM}} \hat{J}^{n_{JM}} \tag{8.65}$$

$$\hat{P}_l = C_l \left(\hat{J}\hat{f}^{n_{fl1}} + b_{Jl} \right)^{n_{Jl}} \hat{f}^{n_{fl2}} \tag{8.66}$$

are considered herein.

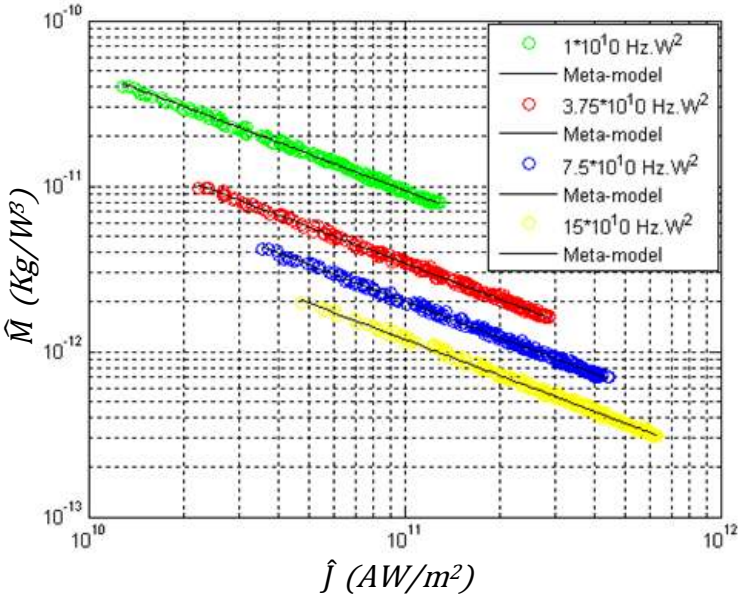

Fig. 8.5 Normalized Mass Versus Normalized Current Density

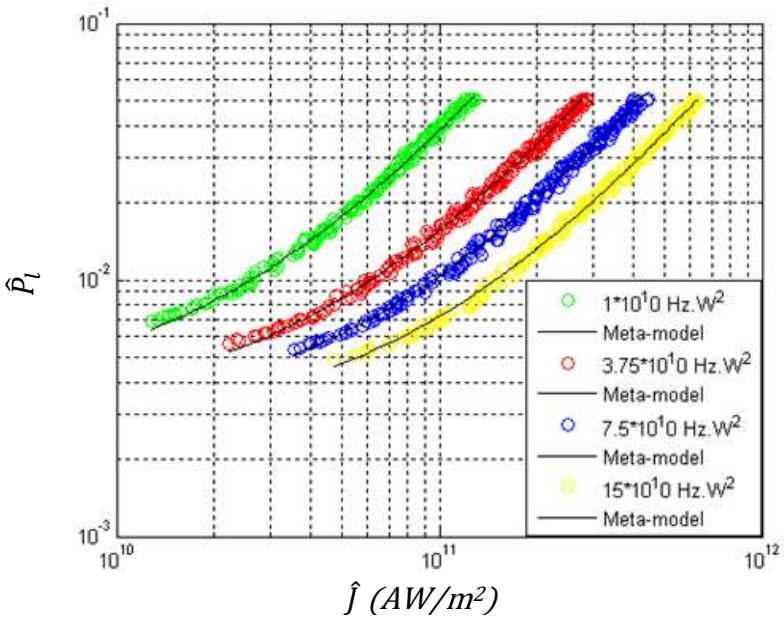

Fig. 8.6 Normalized Loss Versus Normalized Current Density

The parameters of the meta-model expressed by (8.66) and (8.67) are calculated using curve fitting techniques and listed in Table 8.2 The resulting curves are plotted with the original data in Fig. 8.5 and Fig. 8.6. Comparing values, one can see that the meta-model obtained by the curve fitting techniques represents the normalized mass and loss for different values of normalized frequency and current density very well.

Table 8.2 Meta-Model Parameters.

Parameter	Value	Parameter	Value
C_M	$4.0298*10^4$	b_{Jl}	$1.9054*10^5$
n_{fM}	-0.7656	n_{Jl}	1.5276
n_{JM}	-0.7251	n_{fl1}	-0.5142
C_l	$3.5328*10^{-10}$	n_{fl2}	-0.1069

In practice, it is most useful to express the meta-model in terms of the physical quantities. This can be achieved by applying (8.25), (8.33), (8.35), and (8.52) to (8.65) and (8.66)

$$M = C_M P_r^3 \left(f P_r^3 \right)^{n_{fM}} \left(J P_r \right)^{n_{JM}} \tag{8.67}$$

$$P_l = C_l P_r \left(J P_r \left(f P_r^2 \right)^{n_{fl1}} + b_{Jl} \right)^{n_{Jl}} \left(f P_r^2 \right)^{n_{fl2}} \tag{8.68}$$

Equations (8.67) and (8.68) can be used to generate the pareto-optimal front for transformers where specified power rating, (low) operating frequency, and current density. Therefore, for any transformer with a defined operating voltage, rated power, and frequency, the pareto-optimal front for that transformer can be obtained by sweeping the desired range of the current density values. This will be shown in the next section.

8.5. Validation Using Dedicated Design Code

In order to validate the meta-model obtained in (8.67) and (8.68), it is compared with the results obtained using a dedicated design code. The dedicated design code was obtained using the steps explained in Section 8.1.5. Using this code, the pareto-optimal fronts for two design specifications were obtained. To validate the meta-model, a design

from each pareto-optimal front was used as follows: Design 1 is a 240/240 V, 10 kW, 60 Hz transformer and Design 2 is a 500/500 V, 50 kW, 400 Hz transformer. In both designs, the power factor is assumed to be unity. A multi-objective optimization between mass and power loss is conducted for these two designs with the following range of parameters: $5 \le N_\beta \le 10^3$ A/m^2, $10^{-6} \le h_{ci} \le 3$ m, $0.1 \le r_{ci} \le 10$, $10^{-2} \le r_l \le 10$, and $0.1 \le r_c \le 10$. In this design code the number of turns is considered to be a design parameter instead of current density. The current density is calculated using (8.3) and since the transformer voltage is defined then the rated current of winding x is calculated using (8.52). It is assumed that the α-winding and the β-winding voltages are equal and thus the α-winding and the β-winding currents are also equal.

The Pareto-optimal fronts are compared to the meta-model as shown by Fig. 8.7 and Fig. 8.8. As shown, there is a good agreement between the results from the dedicated design code and that predicted by the meta-model.

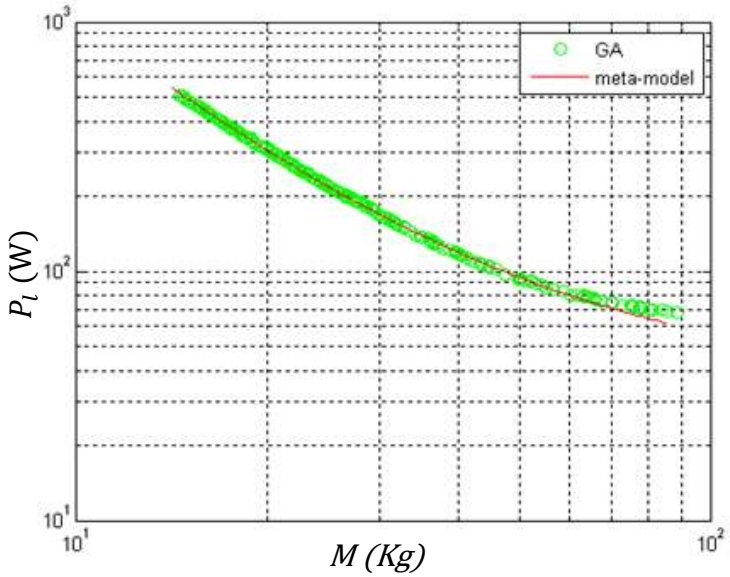

Fig. 8.7 Pareto-Optimal Front for 240 V, 10KW, 60 Hz transformer

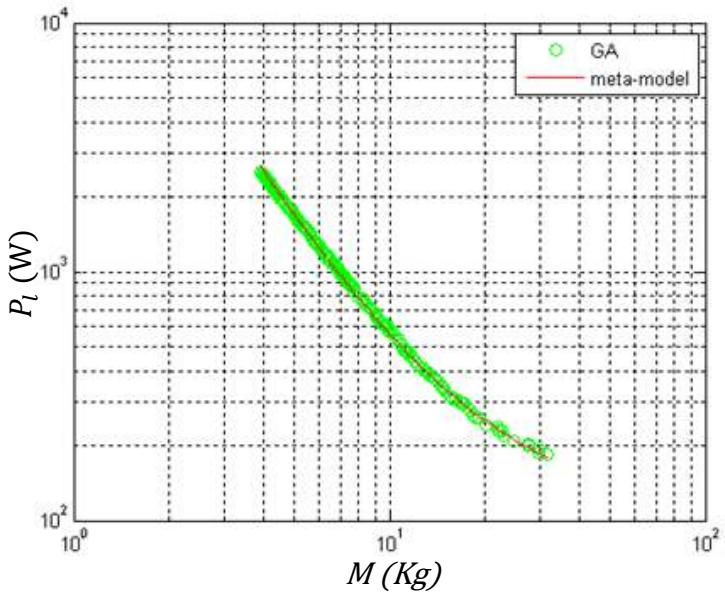

Fig. 8.8 Pareto-Optimal Front for 500 V, 50KW, 400 Hz transformer

Now the stage is set for constructing a meta-model of the tape-wound transformer detailed model. In the next section the scaling laws are used to derive a meta-model of the tape-wound transformer detailed model.

8.6. Tape-wound Transformer Scaling

In the previous sections, scaling of a simplified two-winding transformer was considered. Using the curve fitting techniques, a meta-model was derived and validated by comparing it to a dedicated design code which showed that the meta-model is reasonably accurate. This is a motivation to extend the work to much more involved transformer configuration with more detailed model.

In this section, the meta-model of a tape-wound transformer is derived. The objective is to apply the scaling laws derived in the previous sections to the transformer model derived in Chapters 3-5. It should be noted that the high frequency loss model and the thermal model are not included in the scaling process. Including these models may be of interest for future research.

In the following sub-sections, evaluating transformer performance is considered. Prior to doing, it is useful to derive the per-unit T-equivalent circuit. Also, some of the

expressions derived in Chapter 6 need to be re-defined in terms of the desired parameters in the scaling process. In addition, an assumption is made to make scaling of the eddy current loss possible.

8.6.1. Per Unit T-equivalent Circuit

In the previous chapters, the T-equivalent circuit parameters were expressed in terms of current and number of turns. Since defining current and number of turns is not desired in the scaling process, these expressions need to be modified and expressed in terms of the desired design parameters such as current density. To achieve that, the current density in the j -winding is expressed as

$$\hat{J}_j = \frac{N_{jcl}\hat{i}_{jc}}{k_{jpf}\hat{A}_{jcl}} \tag{8.69}$$

By applying KCL to the MEC depicted in Fig. 3.10, it can be shown that

$$\hat{\Phi}_{\alpha c} = \hat{\Phi}_{m3} - \hat{\Phi}_{m4} + N_{\alpha cl}\hat{i}_{\alpha c}\hat{P}_{\alpha li} \tag{8.70}$$

$$\hat{\Phi}_{\beta c} = \hat{\Phi}_{m3} + N_{\beta cl}\hat{i}_{\beta c}\hat{P}_{\beta l} \tag{8.71}$$

Substituting (8.69) into (8.70) and then into (8.71) yields

$$\hat{\Phi}_{\alpha c} = \hat{\Phi}_{m3} - \hat{\Phi}_{m4} + \hat{J}_{\alpha}k_{\alpha pf}\hat{A}_{\alpha cl}\hat{P}_{\alpha li} \tag{8.72}$$

$$\hat{\Phi}_{\beta c} = \hat{\Phi}_{m3} + \hat{J}_{\beta}k_{\beta pf}\hat{A}_{\beta cl}\hat{P}_{\beta l} \tag{8.73}$$

It should be noted that j in (8.69) is replaced by α in (8.72) and by β in (8.73).

The magnetizing inductance in the linear region can be evaluated using

$$\hat{L}_{m0} = \frac{\hat{\Phi}_{\alpha c}\Big|_{\hat{i}_{\beta}=\hat{i}_{\beta,t},\hat{i}_{\alpha}=0} N_{\beta}}{\hat{i}_{\beta,t}} \tag{8.74}$$

Applying (8.69) to (8.74) yields

$$\hat{L}_{m0} = N_{\beta}^2 \frac{\hat{\Phi}_{\alpha c}\Big|_{\hat{J}_{\beta}=\hat{J}_{\beta,t},\hat{J}_{\alpha}=0}}{N_{\beta cs}N_{\beta cp}\hat{J}_{\beta,t}k_{\beta pf}\hat{A}_{\beta cl}} \tag{8.75}$$

where in (8.75)

$$\hat{J}_{\beta,t} = \frac{N_{\beta cl}\hat{i}_{\beta,t}}{k_{\beta pf}\hat{A}_{\beta cl}N_{\beta cp}} \tag{8.76}$$

From the T-equivalent circuit, leakage inductance of α -winding can be expressed as

$$\hat{L}_{l\alpha} = \left(\frac{N_\beta}{N_\alpha}\right)^2 \frac{N_\alpha \hat{\Phi}_{\alpha c}\Big|_{\hat{i}_\beta=0,\hat{i}_\alpha=\hat{i}_{\alpha,t}}}{\hat{i}_{\alpha,t}} - \hat{L}_{m0} \tag{8.77}$$

Substituting (8.69) and (8.75) into (8.77) yields

$$\hat{L}_{l\alpha} = N_\beta^2 \left(\frac{\hat{\Phi}_{\alpha c}\Big|_{\hat{J}_\beta=0,\hat{J}_\alpha=\hat{J}_{\alpha,t}}}{N_{\alpha cs}N_{\alpha cp}\hat{J}_{\alpha,t}k_{\alpha pf}\hat{A}_{\alpha cl}} - \frac{\hat{\Phi}_{\alpha c}\Big|_{\hat{J}_\beta=\hat{J}_{\beta,t},\hat{J}_\alpha=0}}{N_{\beta cs}N_{\beta cp}\hat{J}_{\beta,t}k_{\beta pf}\hat{A}_{\beta cl}} \right) \tag{8.78}$$

The leakage inductance of β -winding can be expressed as

$$\hat{L}_{l\beta} = \frac{N_\beta \hat{\Phi}_{\beta c}\Big|_{i_\beta=i_{\beta,t},i_\alpha=0}}{\hat{i}_{\beta,t}} - \hat{L}_{m0} \tag{8.79}$$

By substituting (8.75) and (8.76), into (8.79) one obtains

$$\hat{L}_{l\beta} = N_\beta^2 \left(\frac{\hat{\Phi}_{\beta c}\Big|_{\hat{J}_\beta=\hat{J}_{\beta,t},\hat{J}_\alpha=0} - \hat{\Phi}_{\alpha c}\Big|_{\hat{J}_\beta=\hat{J}_{\beta,t},\hat{J}_\alpha=0}}{N_{\beta cs}N_{\beta cp}\hat{J}_{\beta,t}k_{\beta pf}\hat{A}_{\beta cl}} \right) \tag{8.80}$$

The winding resistances are obtained using

$$\hat{r}'_\alpha = N_\beta^2 \frac{\hat{U}_{\alpha cl}}{k_{\alpha pf}\hat{A}_{\alpha cl}^2\sigma_{\alpha c}N_{\alpha cs}N_{\alpha cp}} \tag{8.81}$$

$$\hat{r}_\beta = N_\beta^2 \frac{\hat{U}_{\beta cl}}{k_{\beta pf}\hat{A}_{\beta cl}^2\sigma_{\beta c}N_{\beta cs}N_{\beta cp}} \tag{8.82}$$

where $\sigma_{\alpha c}$ and $\sigma_{\beta c}$ are the conductivities of the α- and the β- winding conductors respectively. It should be noted that the resistance obtained in (8.81) is the referred quantity of the α- winding to the β- winding side.

It is noted that the T-equivalent circuit resistances and inductances remain expressed in terms of the number of the number of turns which is not desired. To eliminate this dependency on the number of turns, per unit (p.u) quantities are defined. The per unit value $f^{(p.u)}$ which correspond to an actual quantity f is calculated as

$$f^{(p.u)} = \frac{f}{f_{base}} \tag{8.83}$$

where f_{base} is the base quantity and f can be voltage, current, power, impedance, or flux.

To set the stage for the derivation of the per unit quantities, the base impedance is defined as

$$\hat{Z}_{base} = \frac{\hat{S}_{base}}{\hat{I}_{base}^{\ 2}} \tag{8.84}$$

In (8.84), $\hat{S}_{base}$ and $\hat{I}_{base}$ are the base power and current which are equal to the corresponding rated values. After substituting (8.69) into (8.84) one can obtain

$$\hat{Z}_{base} = N_{\beta}^2 \frac{\hat{S}_{base}}{\left(k_{\beta pf}\hat{A}_{\beta cl}\hat{J}_{base}N_{\beta cs}N_{\beta cp}\right)^2} \tag{8.85}$$

where $\hat{J}_{base}$ is the base current density which is expressed as

$$\hat{J}_{base} = \frac{N_{\beta}\hat{I}_{base}}{k_{jpf}N_{\beta cs}N_{\beta cp}\hat{A}_{jcl}} \tag{8.86}$$

Now the per-unit values correspond to the T-equivalent circuit resistances and inductances can be evaluated by applying (8.83)-(8.85) to (8.75), (8.78), and (8.80)-(8.82) which yields

$$\hat{L}_{m0}^{(p.u)} = \hat{Y}_b^{pst} \frac{\hat{\Phi}_{\alpha c}\Big|_{\hat{J}_{\beta}=\hat{J}_{\beta,t},\hat{J}_{\alpha}=0}}{N_{\beta cs}N_{\beta cp}\hat{J}_{\beta,t}k_{\beta pf}\hat{A}_{\beta cl}} \tag{8.87}$$

$$\hat{L}_{l\alpha}^{(p.u)} = \hat{Y}_b^{pst}\left(\frac{\hat{\Phi}_{\alpha c}\Big|_{\hat{J}_{\beta}=0,\hat{J}_{\alpha}=\hat{J}_{\alpha,t}}}{N_{\alpha cs}N_{\alpha cp}\hat{J}_{\alpha,t}k_{\alpha pf}\hat{A}_{\alpha cl}} - \frac{\hat{\Phi}_{\alpha c}\Big|_{\hat{J}_{\beta}=\hat{J}_{\beta,t},\hat{J}_{\alpha}=0}}{N_{\beta cs}N_{\beta cp}\hat{J}_{\beta,t}k_{\beta pf}\hat{A}_{\beta cl}}\right) \tag{8.88}$$

$$\hat{L}_{l\beta}^{(p.u)} = \hat{Y}_b^{pst}\left(\frac{\hat{\Phi}_{\beta c}\Big|_{\hat{J}_{\beta}=\hat{J}_{\beta,t},\hat{J}_{\alpha}=0} - \hat{\Phi}_{\alpha c}\Big|_{\hat{J}_{\beta}=\hat{J}_{\beta,t},\hat{J}_{\alpha}=0}}{N_{\beta cs}N_{\beta cp}\hat{J}_{\beta,t}k_{\beta pf}\hat{A}_{\beta cl}}\right) \tag{8.89}$$

The winding resistances are obtained using

$$\hat{r}_{\alpha}^{(p.u)} = \hat{Y}_{b}^{pst} \frac{\hat{U}_{\alpha cl}}{k_{\alpha pf} \hat{A}_{\alpha cl}^{2} \sigma_{\alpha c} N_{\alpha cs} N_{\alpha cp}} \tag{8.90}$$

$$\hat{r}_{\beta}^{(p.u)} = \hat{Y}_{b}^{pst} \frac{\hat{U}_{\beta cl}}{k_{\beta pf} \hat{A}_{\beta cl}^{2} \sigma_{\beta c} N_{\beta cs} N_{\beta cp}} \tag{8.91}$$

where $\hat{Y}_{b}^{pst}$ is the base conductance per square turn which is defined as

$$\hat{Y}_{b}^{pst} = \frac{\left(k_{\beta pf} \hat{A}_{\beta cl} \hat{J}_{base} N_{\beta cs} N_{\beta cp}\right)^{2}}{\hat{S}_{base}} \tag{8.92}$$

It is noted that both the actual resistance and inductances of the T-equivalent circuit and the base impedance are multiplied by N_{β}^{2}. As a result, the per-unit quantities are not functions of the number of turns.

8.6.2. Magnetizing Flux

As will be discussed later, the magnetizing curve is represented as a relationship between magnetizing flux and current density. Therefore, deriving an expression for the magnetizing flux is required. To achieve that, the relationship between the p.u. flux and flux linkage is considered

$$\hat{\Phi}_{m}^{(p.u)} = \frac{\hat{\lambda}_{m}^{(p.u)}}{N_{\beta}} \tag{8.93}$$

In order to obtain the actual value of the magnetizing flux, the base value of the flux linkage need to be defined. From the definition of p.u. inductances, it can be noted that the base flux linkage is equal to the base voltage

$$\hat{\lambda}_{base} = \hat{V}_{base} \tag{8.94}$$

Using (8.69), (8.83), (8.93) and (8.94), the actual value of the magnetizing flux can be expressed as

$$\hat{\Phi}_{m} = \frac{\hat{\lambda}_{m}^{(p.u)} \hat{S}_{base}}{N_{\beta cs} N_{\beta cp} k_{\beta pf} \hat{J}_{base} \hat{A}_{\beta cl}} \tag{8.95}$$

8.6.3. Core Loss

In order to evaluate the core loss S_{cl}^{k} using the MSE [13], calculating the flux density in the core tubes is required. The flux density in the core tubes can be evaluated using the MEC depicted in Fig. 3.10. As shown, the mmf source of the j- winding is expressed as

$$mmf_{j}^{k} = 2N_{jcl}^{k}\hat{i}_{jc}^{k} \tag{8.96}$$

As mentioned earlier in this chapter, the winding currents and number of turns are not defined in the scaling process. Therefore, the winding mmf is re-derived in terms of the current density. Applying (8.69) to (8.96) yields

$$mmf_{j}^{k} = 2\hat{J}_{j}^{k}k_{jpf}\hat{A}_{jcl} \tag{8.97}$$

Scaling eddy current loss is another challenge in the scaling process as discussed in Section 8.1.4. Therein, this issue was resolved by neglecting the eddy current loss. However, this assumption can lead to significant error for high frequencies. In this section, an assumption is made to make scaling of the eddy current loss possible. Specifically, if $k_e f$ is held constant then (8.51) can be expressed only in terms of the scaled frequency as

$$\hat{S}_{e} = k_{ef}B_{\max}^{2}\hat{f}\hat{U}_{c} \tag{8.98}$$

where $k_{ef} = k_e f$.

Typically, when the transformer operating frequency increases, the thickness of the transformer core lamination is reduced. Since k_e is proportional to the transformer lamination thickness then holding $k_e f$ constant may be justified.

8.6.4. Voltage Regulation

The transformer voltage regulation can be expressed in terms of the per unit quantities as

$$\chi = \left| \left(\hat{r}_{\alpha}^{(p.u)} + j\hat{\omega}_{e}\hat{L}_{l\alpha}^{(p.u)} \right) \left(1 + \frac{\hat{L}_{l\beta}^{(p.u)}}{\hat{L}_{m}^{(p.u)}} - \frac{j\hat{r}_{\beta}^{(p.u)}}{\hat{\omega}_{e}\hat{L}_{m}^{(p.u)}} \right) + \hat{r}_{\beta}^{(p.u)} + j\hat{\omega}_{e}\hat{L}_{l\beta}^{(p.u)} \right| \frac{\hat{I}_{\alpha,fl}^{(p.u)}}{\hat{V}_{\beta}^{(p.u)}} \tag{8.99}$$

8.6.5. Operating Point Analysis

The operating point analysis is conducted using a numerical method similar to the method applied in Chapter 6. A difference is that the T-equivalent circuit and the MEC are expressed in terms of the p.u. quantities instead of the actual quantities. It is assumed that the analysis is performed under normal loading conditions with the assumption that the input voltage $\tilde{V}$ and the referred load impedance $\hat{Z}_l'$ are constant.

The steps of the numerical method are as follows:

Step 1 – Magnetizing Current Density as a Function of Magnetizing Flux

Since it is not desired to specify currents and number of turns, the magnetizing curve is constructed as a relationship between the magnetizing current density and the magnetizing flux. To obtain this relationship using the MEC, the β–winding current density is set to zero and test current densities between zero and multiple of the nominal are applied to the α–winding. The magnetizing flux corresponding to a test current density $\hat{J}_m$ is calculated as

$$\hat{\Phi}_m = \hat{\Phi}_\beta\Big|_{\hat{J}_\beta=0,\hat{J}_\alpha=\hat{J}_m} \tag{8.100}$$

From this data, the current density

$$\hat{J}_{ml} = F_{Jm}\left(\hat{\Phi}_m\right) \tag{8.101}$$

is generated.

\Step 2 – Initialization

The p.u. magnetizing inductance, core resistance, and the magnetizing current component in the core resistance are initialized to

$$\hat{R}_c^{1(p.u)} = \infty \tag{8.102}$$

$$\hat{L}_m^{1(p.u)} = \hat{L}_{m0}^{(p.u)} \tag{8.103}$$

Also from (8.102) the component of the p.u. magnetizing current that flows in the core resistance is initialized to

$$\hat{i}_{mR}^{1(p.u)} = 0 \tag{8.104}$$

Step 3 – Solving the p.u. T-equivalent Circuit

In order to solve the T-equivalent circuit, the p.u. values obtained in the previous section are used. From the T-equivalent circuit, the per unit impedance at the magnetizing branch is calculated as:

$$\hat{Z}_m^{k(p.u)} = \frac{j\omega_e \hat{L}_m^{k(p.u)} \hat{R}_c^{k(p.u)}}{\hat{R}_c^{k(p.u)} + j\omega_e \hat{L}_m^{k(p.u)}} \tag{8.105}$$

The per unit values of the α-winding branch impedance and the referred β-winding branch impedance are defined as

$$\hat{Z}_\beta^{(p.u)} = \hat{r}_\beta^{(p.u)} + j\omega_e \hat{L}_{l\beta}^{(p.u)} \tag{8.106}$$

$$\hat{Z}_\alpha^{(p.u)} = \hat{r}_\alpha^{(p.u)} + j\omega_e \hat{L}_{l\alpha}^{(p.u)} \tag{8.107}$$

The series combination of $\hat{Z}_\alpha^{(p.u)}$ and $\hat{Z}_l^{(p.u)}$ is expressed

$$\hat{Z}_{\alpha l}^{(p.u)} = \hat{Z}_\alpha^{(p.u)} + \hat{Z}_l^{(p.u)} \tag{8.108}$$

And finally, the parallel combination of $\hat{Z}_m^{(p.u)}$ and $\hat{Z}_{\alpha l}^{(p.u)}$ is expressed

$$\hat{Z}_{m\alpha l}^{k(p.u)} = \frac{\hat{Z}_m^{k(p.u)} \hat{Z}_{\alpha l}^{(p.u)}}{\hat{Z}_m^{k(p.u)} + \hat{Z}_{\alpha l}^{(p.u)}} \tag{8.109}$$

Using the impedance expressions derived in (8.105)-(8.109), the p.u magnetizing voltage and the voltage and current at the load side are calculated

$$\hat{V}_m^{k(p.u)} = \frac{\hat{Z}_{m\alpha l}^{k(p.u)}}{\hat{Z}_{m\alpha l}^{k(p.u)} + \hat{Z}_\beta^{(p.u)}} \hat{V}_\beta^{(p.u)} \tag{8.110}$$

$$\hat{V}_\alpha^{k(p.u)} = \frac{\hat{Z}_l^{(p.u)}}{\hat{Z}_l^{(p.u)} + \hat{Z}_\alpha^{(p.u)}} \hat{V}_m^{k(p.u)} \tag{8.111}$$

$$\hat{I}_\alpha^{k(p.u)} = \frac{\tilde{V}}{\hat{Z}_l^{(p.u)}} \tag{8.112}$$

It is noted form (8.86) that the p.u current and current density are equal, thus

$$\hat{J}_\alpha = I_\alpha^{k(p.u)} \hat{J}_{base} \tag{8.113}$$

Step 4 – Magnetizing Current Density

The p.u. magnetizing voltage is assumed to be

$$\hat{v}_m^{k(p.u)} = \sqrt{2}\left|\hat{V}_m^{k(p.u)}\right|\sin\left(\hat{\omega}_e\hat{t} + \phi_{vm}^k\right) \tag{8.114}$$

The p.u magnetizing flux linkage obtained from the magnetizing voltage using Faraday's law is expressed:

$$\hat{\lambda}_m^{k(p.u)} = \frac{\sqrt{2}\left|\hat{V}_m^{k(p.u)}\right|}{\hat{\omega}_e}\cos\left(\hat{\omega}_e\hat{t} + \phi_{vm}^k\right) \tag{8.115}$$

From (8.95)

$$\hat{\Phi}_m^k = \frac{\hat{\lambda}_m^{k(p.u)}\hat{S}_{base}}{N_{\beta cs}N_{\beta cp}k_{\beta pf}\hat{J}_{base}\hat{A}_{\beta cl}} \tag{8.116}$$

Substituting the value of the magnetizing flux obtained using (8.116) into (8.101) yields the corresponding magnetizing current density then the p.u. magnetizing current is calculated as,

$$\hat{i}_{mL}^{k(p.u)}\left(\hat{t}\right) = \frac{\hat{J}_{mL}^k\left(\hat{t}\right)}{\hat{J}_{base}} \tag{8.117}$$

The total p.u. magnetizing current is then calculated as

$$\hat{i}_m^{k(p.u)}\left(\hat{t}\right) = \hat{i}_{mL}^{k(p.u)}\left(\hat{t}\right) + \hat{i}_{mR}^{k(p.u)}\left(\hat{t}\right) \tag{8.118}$$

Step 5 – Updating the Magnetizing Branch Parameters

In this step, the p.u. magnetizing inductance and the core resistance for the following iteration are calculated. First the β- winding current is calculated

$$\hat{i}_\beta^{k(p.u)}\left(\hat{t}\right) = \hat{i}_m^{k(p.u)}\left(\hat{t}\right) - \hat{i}_\alpha^{k(p.u)}\left(\hat{t}\right) \tag{8.119}$$

The current density of the β-winding is then calculated as

$$\hat{J}_\beta = \hat{I}_\beta^{k(p.u)}\hat{J}_{base} \tag{8.120}$$

Using the MEC depicted in Fig. 3.10 with the winding mmfs are defined as in (8.97), the flux density in the core tube is obtained. Then the MSE is used to compute the core loss $\hat{S}_{cl}^k$, [1]

Using (8.83), the per unit core loss is calculated as

$$\hat{P}_{cl}^{k(p.u)} = \frac{\hat{P}_{cl}^{k}}{\hat{P}_{base}} \tag{8.121}$$

Next, the p.u. core resistance is updated

$$\hat{R}_{c}^{k+1(p.u)} = \frac{\left(\hat{V}_{m}^{k(p.u)}\right)^{2}}{\hat{P}_{cl}^{k(p.u)}} \tag{8.122}$$

The p.u. current in the core resistance for the next iteration is thus computed as

$$\hat{i}_{mR}^{k+1(p.u)} = \frac{\hat{v}_{m}^{k(p.u)}}{\hat{R}_{c}^{k+1(p.u)}} \tag{8.123}$$

Next, the Fourier series is used to obtain the fundamental component of the p.u. current through the magnetizing inductance. To do so, Fourier series coefficient are expressed as

$$\hat{a}_{mL1}^{k} = \frac{4}{\hat{T}} \int_{0}^{\hat{T}/2} \hat{i}_{mL}^{k(p.u)}\left(\hat{t}\right)\cos\left(\hat{\omega}_{e}\hat{t}\right)d\hat{t} \tag{8.124}$$

$$\hat{b}_{mL1}^{k} = \frac{4}{\hat{T}} \int_{0}^{\hat{T}/2} \hat{i}_{mL}^{k(p.u)}\left(\hat{t}\right)\sin\left(\hat{\omega}_{e}\hat{t}\right)d\hat{t} \tag{8.125}$$

The p.u. rms value of the magnetizing current through the magnetizing inductance is computed as

$$\hat{I}_{mL}^{k(p.u)} = \frac{1}{\sqrt{2}}\sqrt{\left(\hat{a}_{mL1}^{2} + \hat{b}_{mL1}^{2}\right)} \tag{8.126}$$

Subsequently, p.u. value of the magnetizing inductance for the next iteration is updated as

$$\hat{L}_{m}^{k+1(p.u)} = \frac{\hat{V}_{m}^{k(p.u)}}{\hat{\omega}_{e}\hat{I}_{mL}^{k(p.u)}} \tag{8.127}$$

Step 6 – Checking the Convergence

To check the convergence, the error metrics are defined

$$e = \max\left(\left|\frac{\hat{R}_{c}^{k+1(p.u)} - \hat{R}_{c}^{k(p.u)}}{\hat{R}_{c}^{k+1(p.u)}}\right|, \left|\frac{\hat{L}_{m}^{k+1(p.u)} - \hat{L}_{m}^{k(p.u)}}{\hat{L}_{m}^{k+1(p.u)}}\right|\right) \tag{8.128}$$

In (8.128), if the error is less than the maximum allowed error, e_{mxa}, then the algorithm proceeds to the final calculation step. Otherwise, the iterative process is repeated starting at step 3.

Step 7 – Final Calculations

Once convergence is obtained, the transformer total power loss is computed. The resistive power loss is calculated as

$$\hat{P}_{rl}^{(p.u)} = \hat{r}_{\beta}^{(p.u)} \hat{I}_{\beta}^{(p.u)2} + \hat{r}_{\alpha}^{'(p.u)} \hat{I}_{\alpha}^{'(p.u)2} \tag{8.129}$$

The p.u. total power loss is

$$\hat{P}_{l}^{(p.u)} = \hat{P}_{rl}^{(p.u)} + \hat{P}_{cl}^{(p.u)} \tag{8.130}$$

From (8.83), the actual value of the total power loss can be obtained

$$\hat{P}_{l} = \hat{P}_{l}^{(p.u)} \hat{P}_{base} \tag{8.131}$$

The current density in the j-winding is also calculated using

$$\hat{J}_{j} = \left| \hat{I}_{j}^{(p.u)} \right| \hat{J}_{base} \tag{8.132}$$

8.6.6. Inrush Current Density

The inrush current behavior discussed in Chapter 6 is addressed herein by defining the maximum allowed inrush current density instead of the inrush current. By applying a test current density that is equal to the maximum allowed inrush current density to the β-winding while setting the α-winding current density to zero, the corresponding value of the magnetizing flux is obtained. This value is then compared to the worst case scenario flux which is expressed as

$$\hat{\Phi}_{\beta,wcs} = \frac{\hat{\lambda}_{\beta,wcs}^{(p.u)} \hat{S}_{base}}{N_{\beta cs} N_{\beta cp} k_{\beta pf} \hat{J}_{base} \hat{A}_{\beta cl}} \tag{8.133}$$

where $\hat{\lambda}_{\beta,wcs}^{(p.u)}$ is the p.u. worst case scenario flux linkage which is defined as

$$\hat{\lambda}_{\beta,wcs}^{(p.u)} = \frac{2\sqrt{2}\hat{V}_{\beta}^{(p.u)}}{\hat{\omega}_{e}} \tag{8.134}$$

If the value of the flux corresponds to this test current density is greater than the worst case scenario flux, then the worst case scenario magnetizing current density will be less than the maximum allowed inrush current density and the constraint will be met.

8.7. Scaled Design Process of a Tape-Wound Transformer

The scaled quantities correspond to the tape-wound transformer performance derived in Section 8.6 are used as the basis of the design process.

8.7.1. Transformer Analysis Organization

As mentioned in Chapter 7, it is useful to organize these parameters into categories. First, the variables that are related to the transformer configuration are defined. The independent sets of the core, clearance, and winding parameters are defined as

$$\mathbf{C}_I = \left[m_c \;\; \hat{r}_{ci} \;\; \hat{t}_c \;\; \hat{d}_c \right]^T \tag{8.135}$$

$$\mathbf{G}_I = \left[\hat{c}_{\alpha\beta} \;\; \hat{c}_{\beta\beta} \;\; \hat{c}^*_{\alpha v} \;\; \hat{c}^*_{\beta v} \right]^T \tag{8.136}$$

$$\mathbf{W}_{\alpha I} = \left[m_\alpha \;\; N_{\alpha cs} \;\; N_{\alpha cp} \;\; k_{\alpha pf} \right]^T \tag{8.137}$$

$$\mathbf{W}_{\beta I} = \left[m_\beta \;\; N_{\beta cs} \;\; N_{\beta cp} \;\; k_{\beta pf} \right]^T \tag{8.138}$$

and the dependent sets are defined as

$$\mathbf{C}_D = \left[\mathbf{P}_c^T \;\; \hat{h}_{ci} \;\; \hat{w}_{ci} \;\; \hat{h}_{co} \;\; \hat{w}_{co} \;\; \hat{r}_{co} \;\; \hat{A}_{cv} \;\; \hat{l}_{cv} \;\; \hat{A}_{ch} \;\; \hat{l}_{ch} \;\; \hat{U}_c \;\; \hat{M}_c \right]^T \tag{8.139}$$

$$\mathbf{G}_D = \left[\hat{c}_{\alpha c} \;\; \hat{c}_{bc\_mn} \;\; \hat{c}_{\alpha v} \;\; \hat{c}_{\beta v} \right]^T \tag{8.140}$$

$$\mathbf{W}_{\alpha D} = \left[\mathbf{P}_\alpha^T \;\; \hat{w}_\alpha \;\; \hat{h}_\alpha \;\; \hat{A}_{\alpha cl} \;\; \hat{U}_{\alpha cl} \;\; \hat{M}_\alpha \right]^T \tag{8.141}$$

$$\mathbf{W}_{\beta D} = \left[\mathbf{P}_\beta^T \;\; \hat{w}_\beta \;\; \hat{h}_\beta \;\; \hat{A}_{\beta cl} \;\; \hat{U}_{\beta cl} \;\; \hat{M}_\beta \right]^T \tag{8.142}$$

The structure of the transformer description is then defined as

$$\mathbf{T} = \left[\mathbf{C}^T \;\; \mathbf{G}^T \;\; \mathbf{W}_\alpha^T \;\; \mathbf{W}_{\beta D}^T \;\; \hat{d}_T \;\; \hat{w}_T \;\; \hat{h}_T \;\; \hat{M}_T \right]^T \tag{8.143}$$

The vector of the electrical parameters is also defined as

$$\mathbf{E} = \left[\hat{r}_{\beta}^{(p.u)} \;\; \hat{r}_{\alpha}^{(p.u)} \;\; \hat{L}_{l\beta}^{(p.u)} \;\; \hat{\mathrm{L}}_{l\alpha}^{(p.u)} \;\; \hat{\mathrm{L}}_{m0}^{(p.u)} \;\; \chi \right]^T \tag{8.144}$$

The vectors which contains the operating point analysis input set $\mathbf{O}_I$ and output set $\mathbf{O}_O$ are defined as

$$\mathbf{O}_I = \left[\hat{V}_{\beta}^{(p.u)} \;\; \hat{Z}_L^{(p.u)} \;\; \hat{\omega}_e \right]^T \tag{8.145}$$

$$\mathbf{O}_O = \left[\hat{I}_{\beta}^{(p.u)} \;\; \hat{V}_{\alpha}^{(p.u)} \;\; \hat{P}_{rl} \;\; \hat{P}_{cl} \;\; \hat{P}_l \;\; \hat{L}_m^{(p.u)} \;\; \hat{R}_c^{(p.u)} \;\; B_{ch}(t) \;\; B_{cv}(t) \;\; \ldots \right. \tag{8.146}$$
$$\left. B_{co,1}(t) \;\; B_{co,2}(t) \;\; B_{co,3}(t) \;\; \hat{\mathrm{J}}_m(t) \;\; \hat{J}_{\alpha} \;\; \hat{J}_{\beta} \right]^T$$

Finally, the design vector which contain the fixed parameters is defined as

$$\mathbf{D}_{fp} = \left[\hat{c}_{\alpha c\_mn} \;\; \hat{c}_{\alpha\beta} \;\; \hat{c}_{\beta\beta} \;\; \hat{c}_{\alpha v}^{*} \;\; \hat{c}_{\beta v}^{*} \;\; k_{\alpha pf} \;\; k_{\beta pf} \;\; N_{\alpha cs} \;\; N_{\alpha cp} \;\; N_{\beta cs} \;\; N_{\beta cp} \right]^T \tag{8.147}$$

where $k_{\alpha pf}$ and $k_{\beta pf}$ are the packing factors of α- and β- coils respectively.

8.7.2. Design Space

Using the independent variables identified in the previous section, the design space vector is defined as

$$\boldsymbol{\theta} = \left[\hat{J}_r \;\; m_c \;\; m_{\beta} \;\; \hat{h}_{\beta w} \;\; r_{w\beta w} \;\; m_{\alpha} \;\; r_{h\alpha w} \;\; r_{w\alpha w} \;\; r_{dw} \;\; r_{wes} \;\; r_{rci} \right]^T \tag{8.148}$$

where $\hat{h}_{\beta w}$ is scaled height of the β- coil and the ratios $r_{w\beta w}$, $r_{h\alpha w}$, $r_{w\alpha w}$, r_{dw}, r_{wes}, and r_{rci} are defined as

$$r_{w\beta w} = \frac{\hat{w}_{\beta w}}{\hat{h}_{\beta w}} \tag{8.149}$$

$$r_{h\alpha w} = \frac{\hat{h}_{\alpha w}}{\hat{h}_{\beta w}} \tag{8.150}$$

$$r_{h\alpha w} = \frac{\hat{w}_{\alpha w}}{\hat{h}_{\beta w}} \tag{8.151}$$

$$r_{dw} = \frac{\hat{d}_w}{\hat{h}_{\beta w}} \tag{8.152}$$

$$r_{wes} = \frac{\hat{w}_{es}}{\hat{h}_{\beta w}} \tag{8.153}$$

$$r_{rci} = \frac{\hat{r}_{ci}}{\hat{h}_{\beta w}} \tag{8.154}$$

where $\hat{w}_{\beta w}$ is the scaled width of the coil, $\hat{h}_{\alpha w}$ and $\hat{w}_{\alpha w}$ are the scaled height of the coil, and $\hat{d}_w$, $\hat{w}_{es}$, and $\hat{r}_{ci}$ are the scaled winding depth, the scaled straight width of end-winding, and the scaled core radius, respectively.

8.7.3. Design constraints and fitness functions

The design constraints are imposed using the less-than and the greater-than functions defined in (7.31) and (7.32). The first constraint is imposed on the scaled minimum clearance between and core

$$c_1 = \text{gte}\left(\hat{c}_{\alpha c\_mn}, \hat{c}_{mnr}\right) \tag{8.155}$$

where $\hat{c}_{mnr}$ is the scaled minimum required clearance.

As mention in Chapter 7, it is desired to limit the ratio between transformer total height, width, and depth. First the aspect ratio of the transformer is defined as

$$\eta_T = \frac{\max\left(\hat{d}_T, \hat{w}_T, \hat{h}_T\right)}{\min\left(\hat{d}_T, \hat{w}_T, \hat{h}_T\right)} \tag{8.156}$$

Subsequently, the constraint on the aspect ratio is imposed

$$c_2 = \text{lte}\left(\eta_T, \eta_{Tmxa}\right) \tag{8.157}$$

A constraint is imposed to ensure that the scaled height of the β-winding coils is less than the scaled height of the α-winding coils. Thus

$$c_3 = \text{lte}\left(\hat{h}_\beta, \hat{h}_\alpha\right) \tag{8.158}$$

Another constraint on the transformer dimensions is imposed to ensure that the scaled lengths of the core vertical and horizontal legs are greater than zero

$$c_4 = \text{gte}\left(\min\left(\hat{l}_{cv}, \hat{l}_{ch}\right), 0\right) \tag{8.159}$$

The MEC in conjunction with the p.u. T-equivalent circuit are used to calculate the voltage regulation. First, a constraint c_5 is imposed to check MEC convergence. If the MEC solver does not converge, the design is considered infeasible. If the MEC converges, the constraint on the voltage regulation is evaluated using

$$c_6 = \mathrm{lte}\left(\chi, \chi_{mxa}\right) \tag{8.160}$$

The scaled inrush current density is limited implicitly by imposing a constraint on the scaled magnetizing flux. To evaluate, within the MEC the scaled β-winding current density is set to be the maximum allowed scaled inrush current density while the α-winding current density is set to zero. The maximum allowed inrush current density is calculated by multiplying the p.u. of the maximum allowed current by the scaled base current density. Since the MEC is used in this test, a constraint c_7 is imposed to check the MEC convergence. Provided the convergence of MEC, the calculated β-winding scaled flux $\hat{\Phi}_{\beta i}$ is compared to the magnetizing flux defined as the worst case scenario in (8.133). If the calculated scaled flux is greater than the scaled value of the worst case scenario flux then the scaled value of the worst case scenario magnetizing current density will be less than scaled maximum allowed inrush current density. This is archived by imposing the constraint on the β-winding scaled flux as

$$c_8 = \mathrm{lte}\left(\Phi_{\beta i}, \Phi_{\beta wci}\right) \tag{8.161}$$

A constraint c_9 is used to check the convergence of the MEC in the construction of the relationship between the scaled magnetizing current and the scaled magnetizing flux. If convergence occurs then the operating point analysis proceeds.

Similar to Chapter 7, the operating point analysis is conducted for three load conditions: no-load, half-load, and full-load. A design constraint c_{10} is imposed on the convergence of the operating point analysis for the no-load case. If the operating point analysis converges, constraints on the p.u. values of the β-winding maximum current and the range of the α-winding voltage are imposed as

$$c_{11} = \mathrm{lte}\left(\left|I_{\beta,1}^{(p.u)}\right|, I_{\beta,nlmxa}^{(p.u)}\right) \tag{8.162}$$

$$c_{12} = \text{gte}\left(\left|V_{\alpha,1}^{(p.u)}\right|, V_{\alpha nl,mnr}^{(p.u)}\right) \tag{8.163}$$

$$c_{13} = \text{lte}\left(\left|V_{\alpha,1}^{(p.u)}\right|, V_{\alpha nl,mxa}^{(p.u)}\right) \tag{8.164}$$

For the remaining load-conditions, constraints c_{14} and c_{15} are imposed to check the MEC convergence for both half-load and full-load case.

Considering the weight function $\mathbf{w}$, the scaled weighted loss is a function of the scaled loss at every operating point which is calculated as

$$\hat{P}_l = \mathbf{w}^T \hat{\mathbf{P}}_l \tag{8.165}$$

where $\hat{\mathbf{P}}_l$ is a vector that contains the scaled total loss corresponding to all operating points. The constraint on the scaled total loss is obtained as

$$c_{16} = \text{lte}\left(\hat{P}_l, \hat{P}_{lmxa}\right) \tag{8.166}$$

where $\hat{P}_{lmxa}$ is the scaled maximum allowed loss.

The design specifications $\mathbf{D}_{ds}$ as follows

$$\begin{aligned}\mathbf{D}_{ds} = \Big[& \hat{f}\ \hat{\omega}_e\ V_{\beta 0}^{(p.u)}\ V_{\alpha nlmxa}^{(p.u)}\ V_{\alpha nlmnr}^{(p.u)}\ I_{\beta nlmxa}^{(p.u)}\ I_{\alpha fl}^{(p.u)}\ \chi_{mxa}\ \mathrm{i}_{\beta imxa}^{(p.u)}\ \lambda_{\beta wcs}^{(p.u)}\ \ldots \\ & \mathbf{V}_{\beta}^{(p.u)}\ \mathbf{Z}_l^{(p.u)}\ \hat{\boldsymbol{\omega}}_{\mathbf{e}}\ \mathbf{W}\ \hat{P}_{lmxa}\ \eta_{mxa}\ \hat{J}_{\alpha,t}\ \hat{J}_{\beta,t}\ N_{impt}\ N_{tpt}\ O_{emxa}\ O_{imxa} \Big]^T\end{aligned} \tag{8.167}$$

Where $\mathbf{V}_{\beta}^{(p.u)}$, $\mathbf{Z}_l^{(p.u)}$, and $\hat{\boldsymbol{\omega}}_{\mathbf{e}}$ are vectors of β-winding p.u. voltage, p.u. load impedance, and scaled radian frequency values for different load conditions.

Finally, the fitness function is expressed as

$$f(\theta, D) = \begin{cases} \left[\dfrac{1}{\hat{M}_T} \quad \dfrac{1}{\hat{P}_l}\right]^T & c = 1 \\ (c-1)\left[1\ 1\right]^T & c < 1 \end{cases} \tag{8.168}$$

8.7.4. Design Setup

Prior to performing the multi-objective optimization, the design specifications and the search space are defined. The design specifications and fixed parameters are shown in Table 8.3.

Table 8.3 Transformer Design Specifications and Fixed Parameters.

Parameter	Value	Parameter	Value
$V_{\beta 0}^{(p.u)}$	1	N_{Jmpt}	100
$V_{\alpha nlmxa}^{(p.u)}$	1.02	N_{tpt}	50
$V_{\alpha nlmnr}^{(p.u)}$	0.98	O_{emxa}	10^{-3}
$I_{\beta nlmxa}^{(p.u)}$	0.1	O_{imxa}	10
$I_{\alpha fl}^{(p.u)}$	1	$\hat{c}_{\alpha c\_mn}$	10^{-9}
χ_{mxa}	0.05	$\hat{c}_{\alpha\beta}$	10^{-9}
$\mathrm{i}_{\beta imxa}^{(p.u)}$	$2\sqrt{2}$	$\hat{c}_{\beta\beta}$	10^{-9}
$\lambda_{\beta wcs}^{(p.u)}$	0.05	$\hat{c}_{\alpha v}^{*}$	10^{-9}
$\mathbf{V}_{\beta}^{(p.u)}$	$[1\ \ 1]$	$\hat{c}_{\beta v}^{*}$	10^{-9}
$\mathbf{Z}_{l}^{(p.u)}$	$[2\ \ 1]$	$k_{\alpha pf}$	0.6
$\hat{\boldsymbol{\omega}}_{\mathbf{e}}$	$\hat{\omega}_e[1\ \ 1]$	$k_{\beta pf}$	20.6
$\mathbf{W}$	$[0.1\ \ 0.4\ \ 0.5]$	$N_{\beta cp}$	2
$\hat{P}_{lmxa}$	0.1	$N_{\beta cs}$	1
η_{mxa}	$2\sqrt{2}/\hat{\omega}_e$	$N_{\alpha cp}$	2
$\hat{J}_{\alpha,t}$	10^{-3}	$N_{\alpha cs}$	1
$\hat{J}_{\beta,t}$	10^{-3}		

To define the search space of the multi-objective optimization process, the range of the scaled parameters is defined as depicted in Table 8.4. It I noted that the range of the parameters that represent the winding and core material types is defined as an integer while the range of the parameters that represent the transformer dimensions is defined as a logarithmic. After defining the design parameters, specifications, and constraints, a multi-objective optimization is conducted with a population size of 2000 and for 2000 generations.

Table 8.4 Design parameters encoding

Number	Parameter	Minimum	Maximum	Type
1	$\hat{J}_r$	$1*10^{8}$	$1*10^{14}$	Logarithmic
2	m_c	1	4	Integer
3	m_β	1	2	Integer
4	$\hat{h}_{\beta w}$	$1*10^{-7}$	10	Logarithmic
5	$r_{w\beta w}$	0.1	20	Logarithmic
6	m_α	1	2	Integer
7	$r_{h\alpha w}$	0.1	20	Logarithmic
8	$r_{w\alpha w}$	0.1	20	Logarithmic
9	r_{dw}	0.1	20	Logarithmic
10	r_{wes}	0.01	10	Logarithmic
11	r_{rci}	$1*10^{-4}$	$1*10^{-3}$	Logarithmic

8.7.5. Results

A multi-objective optimization is conducted between the normalized loss and the normalized mass. Similar to the process in Section 8.8, the multi-objective optimization is conducted at several values of the normalized frequency. The normalized mass versus normalized current density and normalized loss versus normalized current density at each normalized frequencies are depicted in Fig. 8.9 and Fig. 8.10 respectively. The gene distribution plot when the scaled frequency is $3.75*10^{10}$ Hz.W^2 is shown in the Appendix.

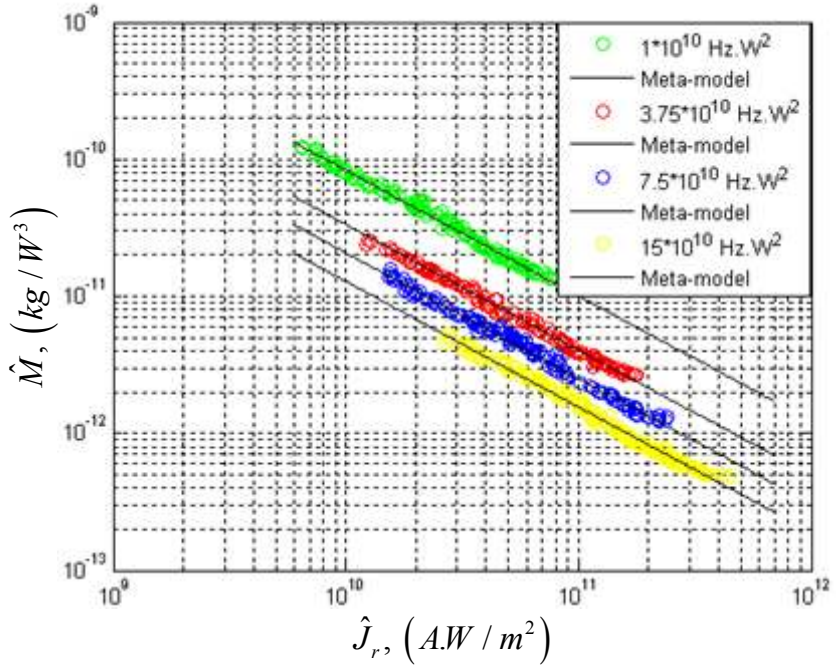

Fig. 8.9 Normalized Mass Versus Normalized Current Density

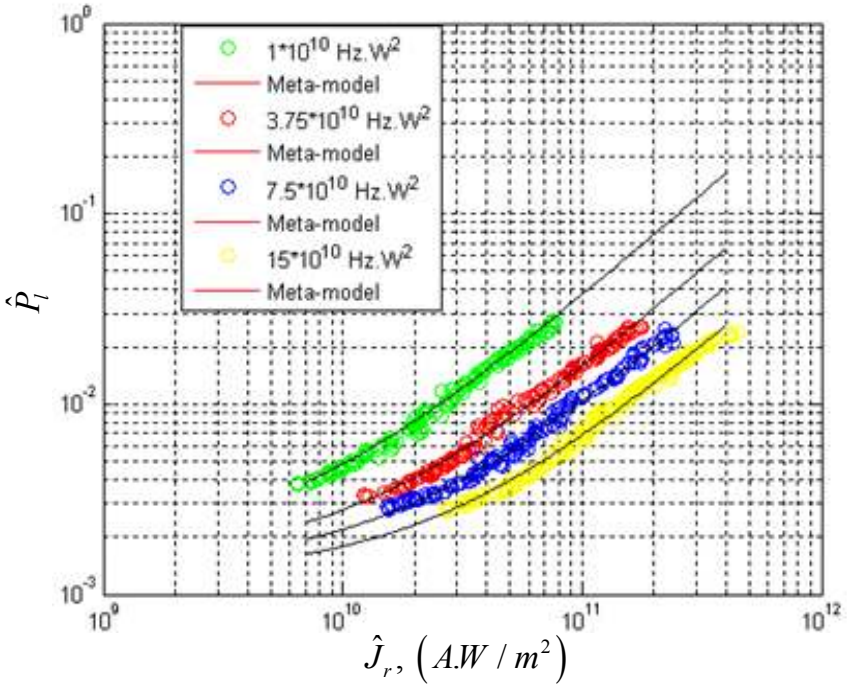

Fig. 8.10 Normalized Loss Versus Normalized Current Density

By using curve fitting techniques, a meta-model based scaling law can be constructed from the results shown in Fig. 8.9 and Fig. 8.10. Using (8.65) and (8.66), the normalized mass and loss as functions of normalized frequency and current density are obtained.

The parameters of the meta-model expressed by (8.65) and (8.66) are calculated using curve fitting techniques and listed in Table 8.5. The resulting curves are plotted with the original data in Fig. 8.9 and Fig. 8.10. It can be seen that the meta-model is reasonably accurate in predicting the relationship between normalized mass and loss for different values of normalized frequency and current density.

Table 8.5 Meta-Model Parameters.

Parameter	Value	Parameter	Value
C_M	$9.218*10^5$	b_{Jl}	$2.907*10^4$
n_{fM}	-0.9155	n_{Jl}	1.098
n_{JM}	-0.6892	n_{fl1}	-0.5345
C_l	$2.993*10^{-7}$	n_{fl2}	-0.1137

The parameter distribution plot is depicted in Fig. 8.11. As shown, each parameter tends to almost converge to a specific value except b_{Jl} which seems to have less significant contribution to the loss Meta-model equation.

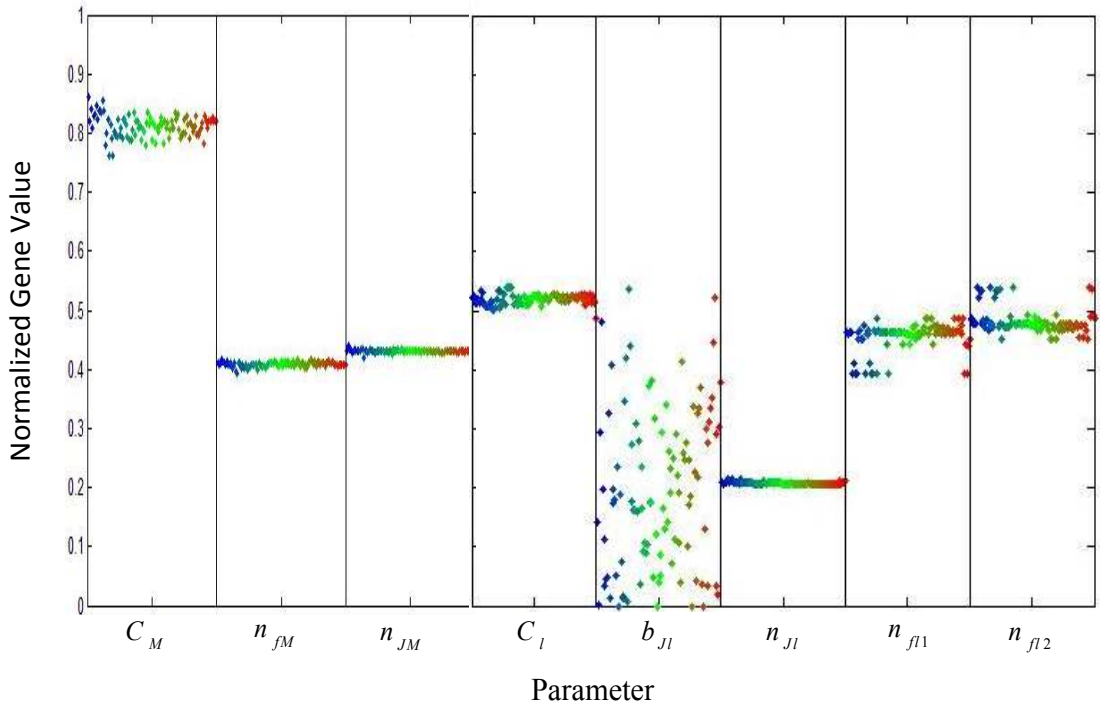

Fig. 8.11 Distribution Plot of Meta-Model Parameters

Using (8.67) and (8.68), the meta-model can be expressed in terms of the physical quantities. When power rating, current density, and frequency are specified, the meta-model defined in (8.67) and (8.68) can accurately predict the Pareto-optimal front for that specific design. Since the transformer eddy current loss is included, the obtained meta-model may be valid for relatively high frequency.

The Pareto-optimal fronts of 240 V, 25 kW, 60 Hz transformer and 500 V, 5kW, 400 Hz transformer are compared to the meta-model as shown in Fig. 8.12 and Fig. 8.13. As shown, there is a good agreement between the results from the dedicated design code and that predicted by the meta-model.

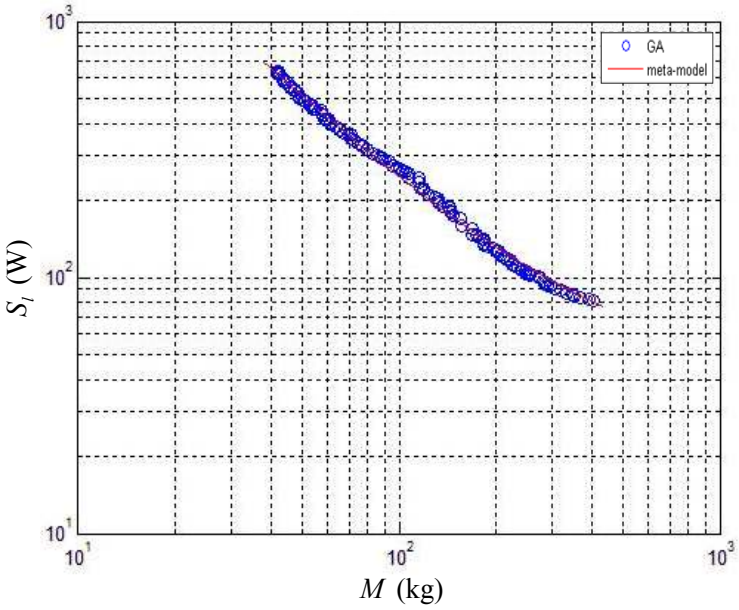

Fig. 8.12 Pareto-Optimal Front for 240 V, 25KW, 60 Hz transformer

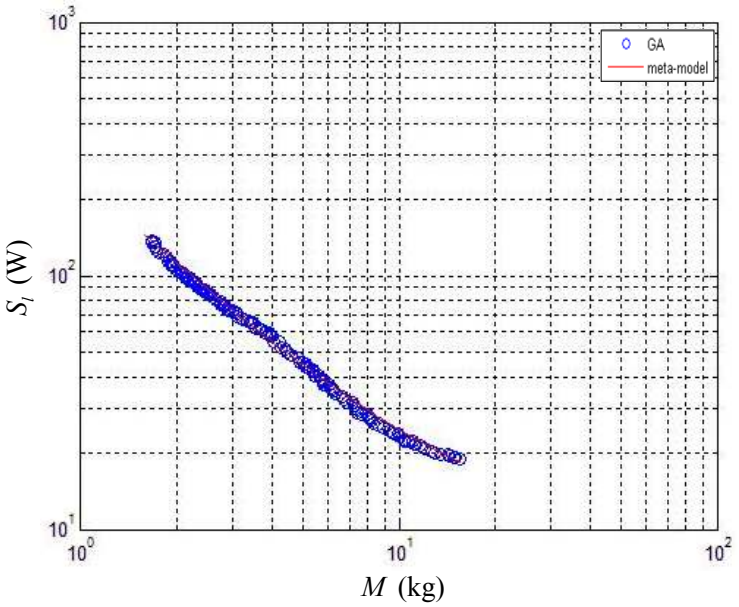

Fig. 8.13 Pareto-Optimal Front for 500 V, 5KW, 400 Hz transformer

9. CONCLUSION AND FUTURE WORK

9.1. Conclusion

In this research, the magnetic equivalent circuit (MEC) of a tape wound core transformer was derived. The MEC elements are core permeances, leakage permeance, and coil MMFs. To accurately predict the flux level in the magnetic material; the core is subdivided into several tubes. The permeance associated with each tube is expressed in terms of the tube dimensions and the core material. Since they tend to saturate faster than any other part in the core, the core corners are represented by three parallel permeances. Using the approach described in [13], the leakage flux paths were predicted based on the position of the coil with respect to the core window. Using these paths, expressions for the leakage permeances were derived. The coil MMF's were defined as a function of coil current and number of turns. Performing the leakage test on the defined MEC, the leakage inductances of both windings were obtained. The leakage inductances calculated by the MEC are compared to the ones calculated using a finite element method (FEM). The difference between the leakage inductances predicted was shown to be relatively small which provides confidence in the MEC model.

In order to accurately predict the performance of high frequency designs, modeling the skin effect and the proximity effect was considered. The skin effect was accounted for by calculating the winding AC resistance. By analytically performing electromagnetic analysis, a second order differential equation that relates the current density to the radius of a cylindrical conductor was obtained. This differential equation which has the same form as the zero order Bessel function was solved by applying the conductor boundary conditions to the solution of the zero order Bessel function. Using this result and the voltage across the conductor terminals, an expression of the conductor AC resistance was derived. This expression was then extended to obtain the AC resistance of the transformer

winding. To model the proximity effect, a frequency independent expression referred to as the dynamic resistance was derived for each coil segment. The dynamic resistance which is a function of the winding parameters and the normalized leakage flux density is a two-by-two matrix when there is a coupling between the leakage fluxes of two coil segments; otherwise, it is only a single element. The normalized flux density was evaluated by applying Ampere's law and the stored energy approach to the leakage paths and then applying the normalization defined in [13] to the result.

A thermal equivalent circuit (TEC) was derived to predict the temperature throughout the transformer. First, the thermal equivalent circuit was derived for a cuboidal element. To achieve rapid analysis of the transformer thermal model, a thermal symmetry was assumed and thus only one-eighth of the transformer was considered for the thermal analysis. This portion of the transformer is divided into 14 cuboidal elements and then the TEC is evaluated for each element. Cuboids which have non rectangular surface areas such as the coil end curvature and the core corner were replaced by effective cuboids that have the same total surface areas. Using the coil homogenization method discussed in [13], an equivalent anisotropic material was used to represent each transformer coil.

To conveniently calculate the transformer performance, the T-equivalent circuit was developed. The parameters of the T-equivalent circuit such as magnetizing inductance and core resistance were determined numerically using the operating point analysis. These analyses were also used to predict the winding currents. These current waveforms were used as inputs to the MEC in order to obtain the flux density in the core and the core loss. Some transformer performance such as voltage regulation and inrush current were also calculated.

Using the machine model, an optimization based design was conducted. The design space which contains the independent parameters is defined. In order to ensure feasible designs, constraints were imposed on the transformer dimensions and performance. Fitness functions which are defined as the reciprocal of the competing objectives i.e. mass and loss were computed. A set of non-dominated designs called the Pareto-optimal

front was obtained. The details of one of the designs in the Pareto-optimal front were presented.

Finally, scaling laws that establish the performance of the tape wound transformer was derived in terms of the transformer ratings. By doing so, the degrees of freedom in the design search space are reduced dramatically. Initially, two winding rectangular transformer was considered. Using the curve fitting techniques, a meta-model which expresses the transformer total mass and loss as a function of transformer power rating was derived. The performance predicted by the meta-model was compared to performance predicted by traditional design code and there was strong agreement between them. The scaling laws are then applied to the tape-wound transformer model derived earlier. However, the high frequency loss model and the thermal model were not included in the scaling process. A meta-model which relates the tap-wound transformer total mass and total loss to the current density, frequency, and rated power was derived. The parameters of the meta-model were obtained using the curve fitting techniques.

9.2. Future Work

In chapter 4, the high frequency model of a tape-wound transformer was derived. In Chapter 5, the transformer thermal model was established by deriving the thermal equivalent circuit (TEC). However, none of these two models was validated. To have more confidence in the analytical model, the high frequency and the TEC models may be validated using numerical analysis. Based on the results obtained using the numerical method, adjustments can be made to the analytical model.

In addition, one of the designs obtained using the analytical method-based optimization can be used to achieve a hardware design of a tape-wound transformer. By doing so, the transformer performance predicted by the analytical model can be compared with measurement.

Finally, including the high frequency loss model in the scaling process can make the transformer meta-model to be valid for higher frequency range. Also it would be useful to include the TEC model within the scaled design process.

LIST OF REFERENCES

LIST OF REFERENCES

[1] Vacuumschmelze "*Tape-wound cores for magnetic amplifier chokes Vitrovac 6025 Z*", Edition 1998

[2] Magmetics "*Fundamentals of tape wound core design*", Edition 2000.

[3] M. Tsili, A. Kladas, P. Georgilakis, A. Souflaris, D. Paparigas, "Advanced design methodology for single and dual voltage wound core power transformers based on a particular finite element model" *Electric power systems research,* vol. 76, no. 9-10, pp. 729-741, Jun. 2006.

[4] V. J. Thottuvelil, T. G. Wilson, and H. A. Owen, "Unusual high-frequency behaviour of some amorphous metallic-alloy tape-wound magnetic cores," *IEEE Transactions on Magnetics,* vol. 20, no. 4, pp. 570–578, Jul. 1984.

[5] T. D.Kefalas, P. S. Georgilakis, A. G. Kladas, A. T. Souflaris, and D. G. Paparigas, "Multiple grade lamination wound core: A novel technique for transformer iron loss minimization using simulated annealing with restarts and an anisotropy model," *IEEE Transactions on Magnetics*, vol. 44, no. 6, pp. 1082–1085, Jun. 2008.

[6] P. Georgilakis, N. Hatziargyiou, N. Doulamis, A. Doulamis, S. Kollias, "Prediction of iron loss of wound core distribution transformer based on artificial neural networks", *Neurocomputing*, vol. 23, no. 13, pp. 15-29, Dec. 1998.

[7] X. Haihong, D. Song, L. Long, "Study of material-saving effect of transformer with 3-D wound core", *Electricity Distribution, China International Conference on*, pp. 1-4, Sept. 2012

[8] B; Cougo, A. Tüysüz, J. Muhlethaler, J.W Kolar, "Increase of tape wound core losses due to interlamination short circuits and orthogonal flux components", *IEEE Industrial Electronics Society Conference,* pp. 1372 – 1377, 2011.

[9] A. Boglietti, P. Ferraris, M. Lazzari, F. Profumo, "Amorphous metal alloy wound core test procedure", *IEEE Industry Applications Annual Meeting Conference,* vol.1, pp. 30-36. Oct. 1990.

[10] M. H. Kheraluwala, D. W. Novotny, and D. M. Divan, "Coaxially wound transformers for high-power high-frequency applications," *IEEE Transactions on Power Electronics*, vol. 7, no. 1, pp. 54–62, Jan. 1992.

[11] **A.** G. Ganz, "Applications of thin Permalloy tape in wide-band telephone and pulse transformers," *Transactions of the American Institute of Electrical Engineers,* vol. 65, no. 4, pp. 177-183, Apr. 1946.

[12] B. Cougo and J. Kolar, "Integration of Leakage Inductance in Tape Wound Core Transformers for Dual Active Bridge Converters," *International Conference on Integrated Power Electronics Systems,* pp. 1-6, Mar. 2012.

[13] S.D. Sudhoff, Power Magnetic Devices: *A Multi-Objective Design Approach*, IEEE Press/Wiley, Jan. 2013.

[14] C. Versele, O. Deblecker, J. Lobry, "Multiobjective optimal design of high frequency transformers using genetic algorithm," *IEEE European Conference on Power Electronics and Applications,* pp. 1-10, Sep. 2009.

[15] C. Versele, O. Deblecker, J. Lobry, "Multiobjective optimal design of transformers for isolated switch mode power supplies," *IEEE International Symposium on Power Electronics Electrical Drives Automation and Motion*, pp. 1687–1692, Jun. 2010.

[16] S. Zhang, Q. Hu, X. Wang, Z. Zhu, "Application of chaos genetic algorithm to transformer optimal design," *IEEE International Workshop on Chaos-Fractals Theories and Applications*, pp. 108-111, Nov. 2009.

[17] R. A. Jabr, "Application of Geometric Programming to Transformer Design," *IEEE Transactions on Magnetics*, vol. 41, no. 11, pp. 4261 - 4269, Nov. 2005.

[18] S. Zhang, Q. Hu, X. Wang, D. Wang, "Research of transformer optimal design modeling and intelligent algorithm," *IEEE Chinese Control and Decision Conference*, pp. 213-218, May 2011.

[19] R. Petkov, "Optimum Design of a High-Power High-Frequency Transformer", *IEEE Transactions on Power Electronics*, vol. 11, no. 1, pp. 33-42, Jan. 1996.

[20] Amoiralis, E.I.; Tsili, M.A.; Kladas, A.G. "Global transformer design optimization using deterministic and non-deterministic algorithms", *IEEE International Conference on Electrical Machines,* pp. 2323-2331, Sep. 2012

[21] S. Farhangi, “A Simple and efficient Optimization Routine for Design of High Frequency Power Transformers”, *Power Electronics and Application Conference*, Sep. 1999

[22] W. G. Hurley, W. H. Wölfe and J. G. Breslin, “Optimized Transformer Design: Inclusive of High-Frequency Effects,” *IEEE Transactions on Power Electronics*, vol. 13, no. 4, pp. 651-659, Jul. 1998.

[23] A. Khatri, H. Malik, O. Rahi, “Optimal Design of Power Transformer Using Genetic Algorithm**”** *IEEE International Conference on Communication Systems and Network Technologies*, pp. 830-833, May 2012.

[24] V. Rashtchi, A. Shabani, A. Bagheri, “Optimal design of measurement-type current transformer using genetic algorithm,” *IEEE International Conference on Power and Energy,* pp. 958-961, Dec. 2008.

[25] J. Du, Y. Feng,G. Wu,P. Li,Z. Mo, “Optimal Design for Rectifier Transformer Using Improved PSO Algorithm,” *IEEE International Conference on Measuring Technology and Mechatronics Automation,* vol. 2, pp. 828-831, Mar. 2010.

[26] N. Tutkun and A. Moses, “Design optimization of a typical strip-wound toroidal core using genetic algorithms,” *Journal of Magnetism and Magnetic Materials,* vol. 277, no. 12, pp. 216-220, Jun. 2004.

[27] Silvester, P.; Konrad, A. "Analysis of Transformer Leakage Phenomena by High-Order Finite Elements", *IEEE Transactions on Power Apparatus and Systems,* vol. 92, no. 6, pp. 1843 – 1855, Nov. 1973.

[28] P. Silvester and M. Chari, "Finite Element Solution of Saturable Magnetic Field Problems," *IEEE Transactions on Power Apparatus and Systems*, vol. 89, no. 7, pp. 1642-1651, sept. 1970.

[29] P. Hammond, “Roth’s method for the solution of boundary-value problems in electrical engineering,” *IET Proceedings of the Institution of Electrical Engineers,* vol. 114, no. 12, pp. 1969–1976, Dec. 1967.

[30] A. Pramanik, "Extension of Roth's method to three-dimensional multi-region Eddy current problems", *IEEE Transactions on Magnetics,* vol. 11, no. 5, pp. 1526 – 1528, Sep. 1975.

[31] A. Pramanik, “Extension of Roth’s method to 2-dimensional rectangular regions containing conductors of any cross-section,” *IET Proceedings of the Institution of Electrical Engineers*, vol. 116, no. 7, pp. 1286–1288, Jul. 1969.

[32] M. Lambert, F. Sirois, M. Martinez-Duro, J. Mahseredjian, "Analytical Calculation of Leakage Inductance for Low-Frequency Transformer Modeling," , *IEEE Transactions on Power Delivery,* vol. 28 , no. 1, pp. 507-515, Jan. 2013.

[33] L. Rabins, "Transformer reactance calculations with digital computers," *American Institute of Electrical Engineers*, vol. 75, no.3, pp. 261–267, Jul. 1956.

[34] P. I. Fergestad and T. Henriksen, "Inductances for the calculation of transient oscillations in transformers," *IEEE Transactions on Power Apparatus and Systems*, vol. 93, no. 2, pp. 510-517, Mar. 1974.

[35] Lambert, M.; Sirois, F.; Martinez-Duro, M.; Mahseredjian, J. "Analytical Calculation of Leakage Inductance for Low-Frequency Transformer Modeling", *IEEE Transactions on Power Delivery,* vol. 28, no. 1, pp. 507 – 515, Jan. 2013.

[36] P. Gómez and F. de León, "Accurate and efficient computation of the inductance matrix of transformer windings for the simulation of very fast transients," *IEEE Transactions on Power Delivery*, vol. 26, no. 3, pp. 1423–1431, Jul. 2011.

[37] R. Doebbelin, C. Teichert, M. Benecke, and A. Lindemann, "Computerized calculation of leakage inductance values of transformers," *Progress in Electromagnetics Research Symposium online*, vol. 5, no. 8, pp. 721–726, Aug. 2009.

[38] R. Doebbelin, M. Benecke, A. Lindemann, "Calculation of Leakage Inductance of Core-Type Transformers for Power Electronics Circuits", *IEEE Power Electronics and Motion Control Conference'*, pp. 1280-1286, Sept. 2008.

[39] Young-Do Kim; Chong-Eun Kim; Kyu-Min Cho; Ki-Bum Park; Gun-Woo Moon "ZVS phase shift full bridge converter with separated primary winding", *IEEE Energy Conversion Congress and Exposition,* pp. 484-489, Sept. 2009.

[40] V. K. Lebedev, "Calculation of the short-circuit resistance of welding transformers with yoke leakage (russ.)," *Automatic Welding*, vol. 11, no. 4, pp. 37–44, 1958.

[41] Sudhoff, S.D.; Shane, G.M.; Suryanarayana, H., "Magnetic-Equivalent-Circuit-Based Scaling Laws for Low-Frequency Magnetic Devices," *IEEE Transactions on Energy Conversion*, vol. 28, no. 3, pp. 746-755, Sept. 2013.

[42] V.Ostovic, *Dynamics of Saturated Electric Machines,* Springer New York, 2011.

[43] J. Cale, S. D. Sudhoff,and Li-Quan Tan, "Accurately Modeling EI Core Inductors Using a High-Fidelity Magnetic Equivalent Circuit Approach," *IEEE Transactions on Magnetics*, vol. 42, no. 1, pp. 40-46, Jan. 2006.

[44] Marco Amrhein and P. T. Krein, "Induction Machine Modeling Approach Based in 3-D magnetic Equivalent Circuit Framework," *IEEE Trans Energy Convers.*, vol. 25, no. 2, pp. 339-347, Jun. 2010.

[45] S. D. Sudhoff, B. T. Kuhn, K. A. Corzine et al, "Magnetic Equivalent Circuit Modeling of Induction Motors," *IEEE Transactions on Magnetics*, vol. 22, no. 2, pp. 259-270, Jun. 2007.

[46] M. L. Bash and S. Pekarek, "Analysis and Validation of a Population – Based design of a Wound-Rotor Synchronous machine," *IEEE Transactions on Energy Conversion*, vol. 27, no. 3, pp. 603-614, Sept. 2012.

[47] P. L. Dowell "Effects of Eddy Currents in Transformer Windings", *IET Proceedings of the Institution of Electrical Engineers,* vol. 113, no. 8, pp.1387 - 1394, Jan. 1966.

[48] P.S.Venkatraman, "Winding eddy current losses in switch mode power transformers due to rectangular wave currents", *Proceedings of Powercon 11,Power Concepts Inc.*, pp. 1–11, 1984.

[49] M.P. Perry, "Multiple layer series connected winding design for minimum losses", *IEEE Transactions on Power Apparatus and Systems*, vol. 98, no. 1, pp. 116–123, Jan. 1979.

[50] S.C. Larson E.Bennet, "Effective resistance of alternating currents of multilayer windings", *IEEE American Institute of Electrical Engineers*, vol. 59, no.12, pp. 1010–1017, Dec. 1940.

[51] Bruce Carsten, "High frequency conductor losses in switch mode magnetics", *International High Frequency Power Conversion Conference.*, pp. 155-176, May 1986.

[52] Richard L. Stoll, *The analysis of eddy currents*, Clarendon Press. Oxford, 1974.

[53] J. A. Ferreira, "Improved analytical modeling of conductive losses in magnetic components", *IEEE Transactions on Power Electronics*, vol. 9, no. 1, pp. 127–131, Jan. 1994.

[54] N. Noferi M.Bartoli and A. Reatti, “Modelling winding losses in high frequency power inductors”, *Journal of Circuits, Systems, and Computers*, vol. 5, no. spec issue, pp. 607–626, Dec. 1996.

[55] William R. Smythe, *Static and Dynamic Electricity*, McGraw-Hill, pp. 411, 1968.

[56] J. A. Ferreira, “Analytical computation of ac resistance of round and rectangular litz wire windings”, *IEEE Proceedings-B Electric Power Applications*, vol. 139, no. 1, pp. 21–25, Jan. 1992.

[57] J. A. Ferreira, *Electromagnetic Modelling of Power Electronic Converters*, Kluwer Academic Publishers, 1989.

[58] X. Nan and C. R. Sullivan "An improved calculation of proximity-effect loss in high-frequency windings of round conductors", *IEEE Annual Power Electronics Specialist Conference*, vol2, pp. 853-860, Jun. 2003.

[59] Sullivan, C.R. "Computationally efficient winding loss calculation with multiple windings, arbitrary waveforms, and two-dimensional or three-dimensional field geometry", *IEEE Transactions on Power Electronics,* vol. 16, no. 1, pp. 142 – 150, Jan. 2001.

[60] Jiankun Hu; Sullivan, C.R. "Optimization of shapes for round-wire high-frequency gapped-inductor windings", *IEEE Annual Meeting Industry Applications Conference,* vol.2, pp. 907-912, Oct. 1998.

[61] Zimmanck, D.R. “Sullivan, C.R. "Efficient calculation of winding-loss resistance matrices for magnetic components," *IEEE Workshop on Control and Modeling for Power Electronics,* pp. 1-5, Jun. 2010.

[62] Shane, G.M.; Sudhoff, S.D. "Design Paradigm for Permanent-Magnet-Inductor-Based Power Converters", *IEEE Transactions on Energy Conversion,* vol. 28, no. 4, pp. 880-893, Dec. 2013.

[63] M. Hettegger , O. Biro , A. Stermecki and G. Ofner "Temperature rise determination of an induction motor under blocked rotor conditions," *IET International Conference on Power Electronics, Machines and Drives,* pp.1-5, Apr. 2010.

[64] Weili Li, Junci Cao, Fei Huo, Jiafeng Shen. "Numerical Analysis of Stator-Rotor Coupled Transient Thermal Field in Induction Motors with Blocked Rotor," *IEEE World Automation Congress,* pp. 1-6, Sept.-Oct. 2008.

[65] M. Lefik, K. Komeza. "Computer Modelling of 3D Transient Thermal Field Coupled with Electromagnetic Field in I-phase Induction Motor with Locked Rotor", *International Symposium on Electromagnetic Fields in Mechatronics, Electrical and Electronic Engineering,* vol. 27, no.4, pp. 861-868, Jun. 2008.

[66] R. Wrobel and P. H. Mellor "A general cuboidal element for three-dimensional thermal modeling", *IEEE Transactions on Magnetics*, vol. 46, no. 8, pp.3197-3200, Aug. 2010

[67] P. H. Mellor, D. Roberts, and D. R. Turner, "Lumped parameter thermal model for electrical machines of TEFC design," *IET Proceedings-B on Electric Power Applications*, vol. 138, no. 5, pp. 205–218, Sep. 1991.

[68] I. J. Perez and J. G. Kassakian, "A stationary thermal model for smooth air-gap rotating electric machines," *Electric Machines & Power Systems*, vol. 3, no. 3, pp. 285–303, 1979.

[69] William H. Yeadon, *Handbook of Small Electric Motors*, New York: McGraw-Hill Companies, Inc., 2001

[70] Ansoft. Maxwell, ver. 12. Available on: WWW.ANSOFT.COM/PRODUCTS/EM/MAXWELL/

[71] Sudhoff, S.D., *"Genetic Optimization System Engineering Tool (GOSET) for Use With MATLAB"* ver. 2.42, School of Electrical and Computer Engineering, Purdue University, West Lafayette, IN, with United States Naval Academy, Annapolis, MD, 2005 [Online]. Available: HTTPS://ENGINEERING.PURDUE.EDU/ECE/RESEARCH/AREAS/PEDS/GO_SYSTEM_ENGINEERING_TOOLBOX

[72] Sudhoff, S.D. and G. Shane, PMM Toolbox: Power Magnetic Material Toolbox (Version 1.2) [MATLAB Toolbox], School of Electrical and Computer Engr., Purdue Univ., HTTPS://ENGINEERING.PURDUE.EDU/ECE/RESEARCH/AREAS/PEDS/POWER_magnetic_material_toolbox, 2010.

[73] Sudhoff, S.D., MEC Toolbox: Magnetic Equivalent Circuit Toolbox (Version 3.0) [MATLAB Toolbox], School of Electrical and Computer Engr., Purdue Univ., HTTPS://ENGINEERING.PURDUE.EDU/ECE/RESEARCH/AREAS/PEDS/MAGNETIC_EQUIVALENT_TOOLBOX, 2012.

[74] Sudhoff, S.D., TEC Toolbox: Thermal Equivalent Circuit Toolbox (Version 2.0) [MATLAB Toolbox], School of Electrical and Computer Engr., Purdue Univ., HTTPS://ENGINEERING.PURDUE.EDU/ECE/RESEARCH/AREAS/PEDS/THERMAL_EQUIVALENT_TOOLBOX , 2014.

[75] Paul C. Krause; Oleg Wasynczuk; Scott D. Sudhoff, *Analysis of Electric Machinery and Drive Systems*, 2nd ed., IEEE Press, 2002.

APPENDIX

A. GENE DISTRIBUTION PLOTS

The gene distribution plot for the tape-wound transformer nominal design approach discussed in Section 7.4 is shown in Figure A 1.

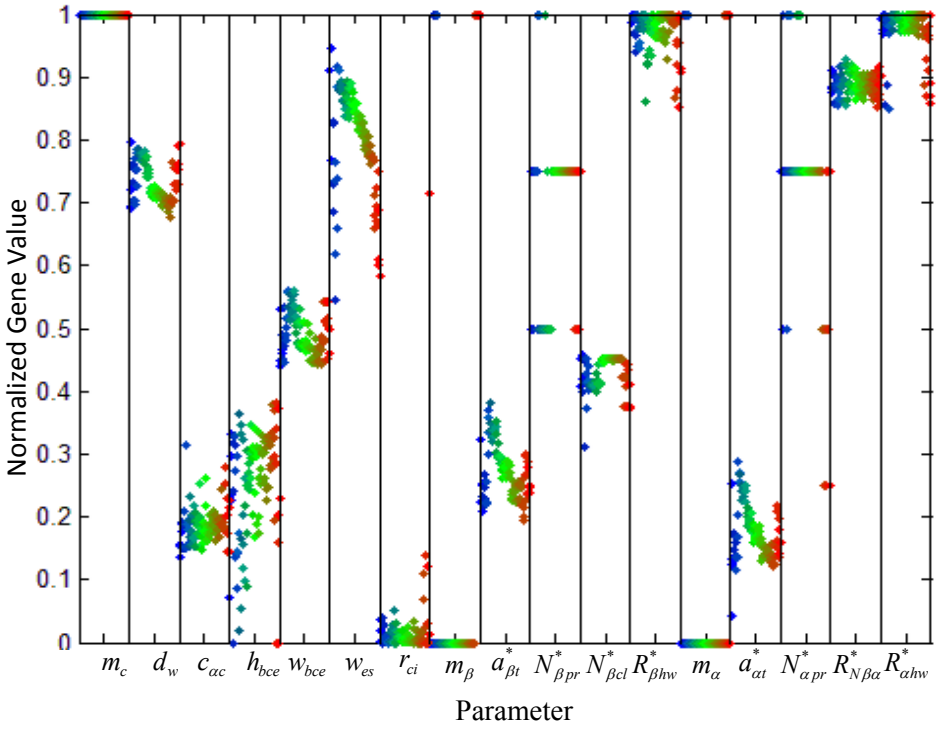

Figure A 1 Gene Distribution Plot for the Result in Section 7.4

The gene distribution plot for the two-winding transformer scaled design approach discussed in Section 8.3 is shown in Figure A 2.

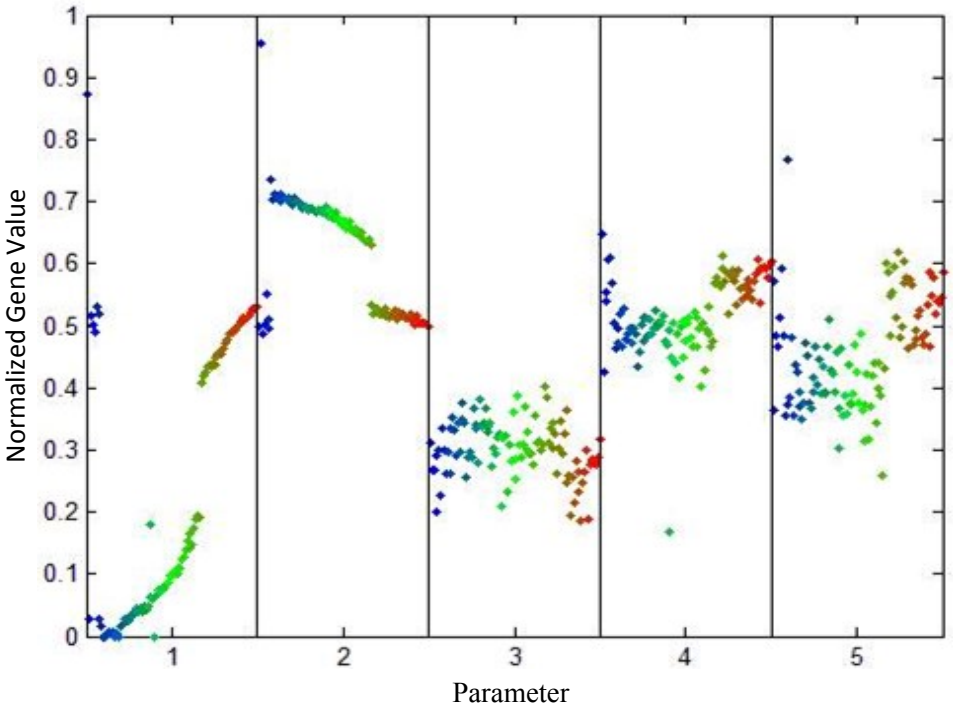

Figure A 2 Gene Distribution Plot for the Result in Section 8.3

The gene distribution plot for the tape-wound transformer scaled design approach discussed in Section 8.7.5 is shown in Figure A 3.

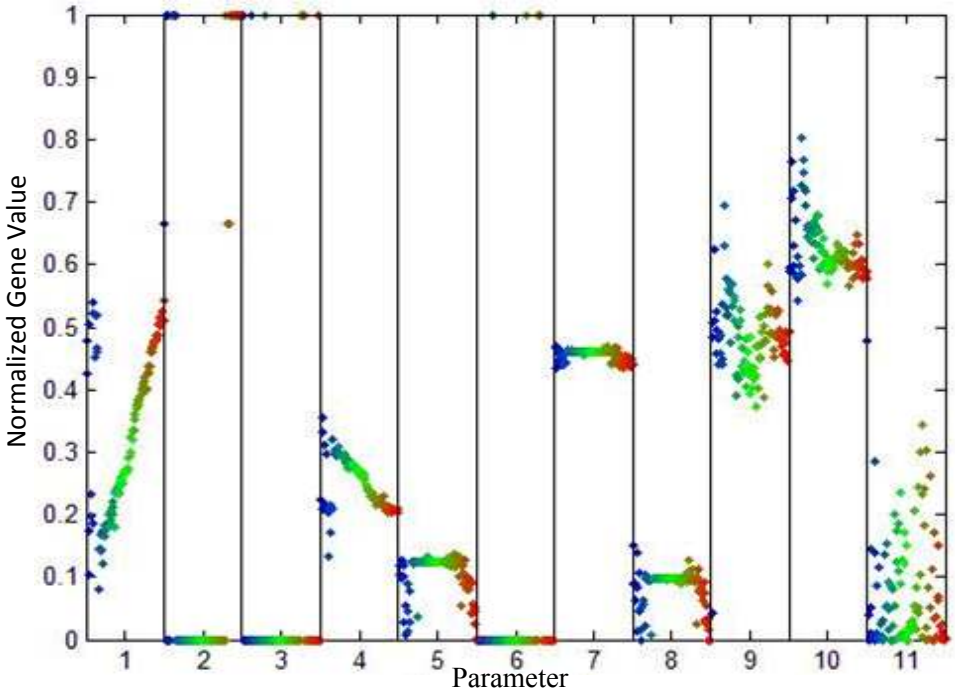

Figure A 3 Gene Distribution Plot for the Result in Section 8.7.5

VITA

VITA

Ahmed Taher received the degree of Bachelor of Science in Electrical Engineering in 2006 from University of Benghazi. In 2011 he received his Master of Science degree from Purdue University. He continued his graduate study at Purdue University to pursue the Doctor of Philosophy degree in Electrical and Computer Engineering. His area of interest is modeling and design of electromagnetic and electromechanical devices.